Crystalline and Amorphous Metallic Membranes for Hydrogen Separation

by

Tianmiao Lai

A Dissertation Presented in Partial Fulfillment
of the Requirements for the Degree
Doctor of Philosophy

Approved August 2015 by the
Graduate Supervisory Committee:

Mary Laura Lind, Chair
Jerry Lin
Jian Li

ARIZONA STATE UNIVERSITY

December 2015

ABSTRACT

In the United States, 95% of the industrially produced hydrogen is from natural gas reforming. Membrane-based techniques offer great potential for energy efficient hydrogen separations. $Pd_{77}Ag_{23}$ is the bench-mark metallic membrane material for hydrogen separation at high temperatures. However, the high cost of palladium limits widespread application. Amorphous metals with lower cost elements are one alternative to replace palladium-based membranes. The overall aim of this thesis is to investigate the potential of binary and ternary amorphous metallic membranes for hydrogen separation. First, as a benchmark, the influence of surface state of $Pd_{77}Ag_{23}$ crystalline metallic membranes on the hydrogen permeability was investigated. Second, the hydrogen permeability, thermal stability and mechanical properties of Cu-Zr and $Ni_{60}Nb_{35}M_5$ (M=Sn, Ti and Zr) amorphous metallic membranes was evaluated.

Different heat treatments were applied to commercial $Pd_{77}Ag_{23}$ membranes to promote surface segregation. X-ray photoelectron spectroscopy (XPS) analysis indicates that the membrane surface composition changed after heat treatment. The surface area of all membranes increased after heat treatment. The higher the surface Pd/(Pd+Ag) ratio, the higher the hydrogen permeability. Surface carbon removal and surface area increase cannot explain the observed permeability differences.

Previous computational modeling predicted that $Cu_{54}Zr_{46}$ would have high hydrogen permeability. Amorphous metallic Cu-Zr (Zr=37, 54, 60 at. %) membranes were synthesized and investigated. The surface oxides may result in the lower experimental hydrogen permeability lower than that predicted by the simulations. The permeability decrease indicates that the Cu-Zr alloys crystallized in less than two hours

during the test (performed at 300 °C) at temperatures below the glass transition temperature. This original experimental results show that thermal stability of amorphous metallic membranes is critical for hydrogen separation applications.

The hydrogen permeability of $Ni_{60}Nb_{35}M_5$ (M=Sn, Ti and Zr) amorphous metallic membranes was investigated. Nanoindentation shows that the Young's modulus and hardness increased after hydrogen permeability test. The structure is maintained amorphous after 24 hours of hydrogen permeability testing at 400°C. The maximum hydrogen permeability of three alloys is 10^{-10} mol m^{-1} s^{-1} $Pa^{-0.5}$. Though these alloys exhibited a slight hydrogen permeability decreased during the test, the amorphous metallic membranes were thermally stable and did not crystalize.

DEDICATION

To my parents and grandfather

ACKNOWLEDGMENTS

First and foremost, I would like to express my deepest appreciation to my advisor, Dr. Mary Laura Lind. It has been an honor for me to be her first Ph.D. student. She gave me the opportunity to do exciting and interesting research in several different projects. I want to thank her for all his continuous support, guidance, assistance and encouragement during my pursuit of Ph.D. I have been motivated by the joy, curiosity and enthusiasm she has for her research.

I would like to thank Dr. Lin and Dr. Li for their willingness to serve on my committee. I really appreciate them for taking the time and efforts to make invaluable inputs and suggestions to my research and dissertation. I would also like to thank Fred Pena for his assistance in building set up, equipment repair and maintenance in the lab.

I would like to thank the help of my collaborators who helped me enormously with my research. They are: Prof. Jerry Lin's group for the help of hydrogen permeability test system setup; Prof. William L. Johnson's group in Caltech, George Kaltenboch, Andrew Hoff; Prof. Zhifeng Ren's group in University of Houston; Prof. William Petuskey's group; Dr. Rongshun Zhu and Prof. David Sholl in Georgia Institute of Technology. I would also like to thank current and former group members.

I highly appreciate Ira A. Fulton Schools of Engineering, ASU; American Chemical Society Petroleum Research Funding DNI (Award #52461-DNI10) for the financial support of this work. We gratefully acknowledge the use of facilities with the LeRoy- Eyring Center for Solid State Science at Arizona State University.

TABLE OF CONTENTS

Page

CHAPTER Page

CHAPTER Page

LIST OF TABLES

Table Page

LIST OF FIGURES

Figure Page

Figure Page

Figure Page

Figure Page

CHAPTER 1 GENERAL INTRODUCTION

1.1 Introduction

According to a report in 2007 by the United Nations Intergovernmental Panel on Climate Change (IPCC), ongoing global warming caused by greenhouse gas emission is mainly to the result of human activities (Le Treut et al. 2007). The implications of global warming, such as a possible rise in sea level, will be devastating to areas near or below the sea level. The use of traditional, hydrocarbon based fossil fuels significantly contributes to greenhouse gas emission (Le Treut et al. 2007). As a fuel, hydrogen has zero greenhouse gas emissions - a property that could help alleviate these problems. In addition to being an emerging as mainstream form of energy, hydrogen is an established commodity chemical for applications in the chemical, petrochemical, food, and textile industries. Specific applications include hydrogenation, providing a source of fuel for fuel cells, and semiconductor doping.

In the United States, 95% of the industrially produced hydrogen is synthesized through the steam-reforming of natural gas or coal through the water-gas shift (WGS) reaction ($CO+H_2O \rightarrow CO_2+H_2$)（Ockwig and Nenoff 2007; Barelli et al. 2008; DOE 2013）. Synthesis gas (a fuel gas mixture consisting primarily of hydrogen, carbon monoxide) is produced from coal steam reaction. Coal derived synthesis gas can be converted to methanol and other industrial chemicals. Combining hydrogen production from natural gas or coal with CO_2 capture can help achieve a “zero emission power plant.” Fuel cells require very high purity hydrogen. The process of separating/purifying hydrogen from the synthesis gas mixture is a very energy consumptive step of hydrogen

production(Dolan et al. 2006). Three of the major methods utilized for hydrogen separation are pressure swing adsorption (PSA), cryogenic separations, and membrane-based processes.

PSA was developed in the early 1960s(Kerry 2007). It is based on the theory that there are different binding forces to adsorbent materials and the equilibrium amount of impurities adsorbed to the bed increase with increasing pressure. Typically, PSA plants can produce hydrogen with purity of 98-99.999%. However, PSA requires multiple absorption beds, thus the investment to build a PSA plant is very high which requires a minimum production of hydrogen to justify building a plant.（Dolan et al. 2006; Barelli et al. 2008）Cryogenic distillation was commercialized in the 1950s. The principle is simply separating gas mixture based on the volatility difference between the components. By cooling the gas mixture to very low temperature, most of the other components transfer to liquid phase while hydrogen stays in gas phase and thus is separated. To completely remove water and CO_2, the cryogenic unit should not freeze. This adds to the complexity and capital cost of the plant. (Kerry 2007).

The development of synthetic membrane dates back approximately 100 years (Bhave 1991). Membrane-based separation has been applied to large scale in industries like sea water desalinization, industrial waste purge, concentration of materials to produce food and drugs, and separation of different phases in petroleum extract (H. Strathmann et al. 2006). Polymer membranes are the primary type of membrane used to separate hydrogen. In the late 1970s, Monsanto commercialized polymeric hollow fiber gas separation membranes called Prism® for hydrogen recovery. Prism® had been

installed in many industrial plants. Encouraged by that, other companies like Dow, Ube and Du Pont also successfully launched membrane-based separation plants. (Baker 2004)

Table 1.1 reproduced from Ho and Sirkar summarizes the advantages of membrane-based separations over the PSA and cryogenic distillation techniques. (Ho and Sirkar 1992) Many membrane materials have been used for hydrogen separations. Two broad classifications of membrane materials are polymer and inorganic.

Table 1.1 Comparison of different types of hydrogen separation methods reproduced from (Ho and Sirkar 1992)

	Membrane	PSA	Cryogenics
Relative investment	1	1 to 3	2 to 3
Maximum operating pressure (psia)	2000	600	1000
Minimum hydrogen content in feed %	15-20	50	20
Max hydrogen purity %	99	99.999	98.5
Max hydrogen recovery	95	85	95
Product pressure/feed pressure	Lower	Same	Same
Retentate pressure/feed pressure	Same	Lower	Lower
Modularity	Yes	No	No
Ease of operation	Very easy	Average	Average

Both porous and dense membranes can be utilized for separation. For separation, there are three separation mechanism involves depending on the characteristic pore size of the membrane: Knudsen diffusion, molecular sieving (surface diffusion) and solution diffusion (Baker 2004). When the pore size is less than 1 micrometer (which is comparable to the mean free path of gas molecules), Knudsen diffusion governs the diffusion. For Knudsen diffusion, the gas molecules interact more frequently with the wall than with each other. If the pore size is approximately 5-20 Å, the separation occurs by molecular sieving. Both diffusion in the gas phase and diffusion through the gas

molecules adsorbed on the pore surface may happen at the same time. Solution-diffusion mechanism describes permeation in dense membranes. All of the polymeric commercial membranes for gas separation are based on solution-diffusion mechanism.

Volumetric flux of component is expressed as *J*, according to Fick's law the flux can be expressed as:

$$J = \frac{\bar{P}}{t}(P_H - P_L)$$

Where $\bar{P}$ is defined as the permeability of membrane; *t* is the thickness of the membrane; P_H is the partial pressure of feed side; P_L is the partial pressure of permeate side. $\bar{P}$ is usually an intrinsic properties of a membrane material. The selectivity $\alpha_{i/j}$ is defined as

$$\alpha_{i/\mathrm{j}} = \frac{\bar{P}_i}{\bar{P}_j}$$

1.2 Polymeric membranes

In 1991, Robeson published a seminal paper on polymeric membranes for gas separation. Robeson(2008) discovered a trade-off between membrane permeability and selectivity in polymeric membranes. The upper bound correlation follows the relationship, where Pi is the permeability of the fast gas, αij (Pi/Pj) is the separation factor, k is referred to as the "front factor" and n is the slope of the log–log plot of the noted relationship. Below this line on a plot of log αij versus log Pi, all the experimental data points exist. In 2008, Robeson updated the upper bounds for all the gas separations. For hydrogen related applications, it does not change very much. Figure 1.1 shows the upper bound for H_2/N_2 reproduced from (Robeson 2008).

Only cellulosics, polysulfones, polyimides and a few other polymeric materials have been used widely at large scale for gas separation. (Paul and Yampol'skii 1994) Cellulose derivatives (cellulosics) are made from cellulose. Cellulose is an abundant raw material and has many sources such as woods, cotton and etc. Cellulosics were initially

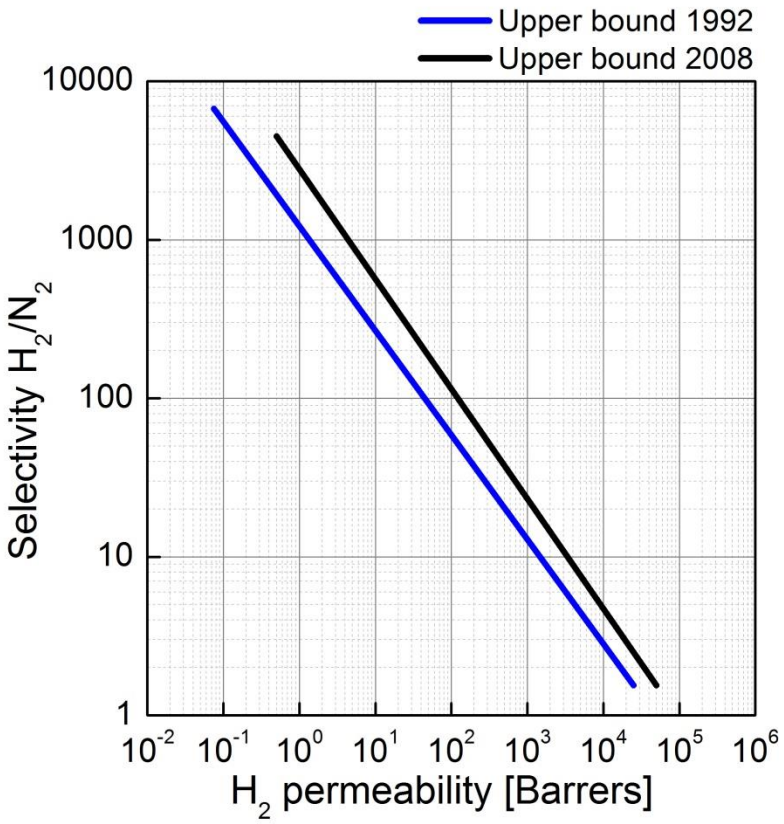

Figure 1.1 Upper bound correlation for H_2/N_2 separation. Image reproduced from (Robeson 2008).

investigated as a membrane material for desalination application in reverse osmosis process. Early hydrogen separation plants utilized cellulose acetate as the membranes. Polysulfones are a membrane material that has been successfully commercialized. It has relatively high T_g (185°C), exhibits stability under oxidative environment, and has good mechanical properties. It was first commercialized by Udel ®. Later, polysulfones were

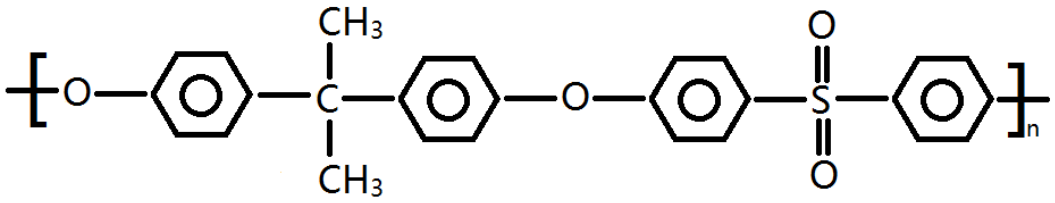

Figure 1.2 Prototype of a typical polysulfone class. Image reproduced from (Kesting and Fritzsche 1993)

commercialized and implemented in large industrial plant by Permea (Monsanto) under the brand name of PRISM®, and they were kept as the second generation of Prism® Alpha membrane. Figure 1.2 shows the one of the prototype polysulfones class(Kesting and Fritzsche 1993). Polyimides are promising class of polymers for gas separation applications. Polyimides rank among the most heat-resistant polymers and have many applications. (Liaw et al. 2012) Polyimides are one type of polymers have been applied for hydrogen separation in industrial plant. In the recent upper bound of H_2/N_2 shown in Figure 1.1, two polyimides are among the polymers near the upper bound. They are 1,1-6FDA-DIA (P_{H2}:31.4 barrer, $\alpha_{H2/N2}$:165(Rezac and Schöberl 1999)); and NTDA-BAPHFDS(H) (P_{H2}: 52, $\alpha_{H2/N2}$: 141(Tanaka et al. 2006).

Table 1.2 shows the hydrogen permeability and separation factor over N_2 of some polymers. The data is from two sources: (Paul and Yampol'skii 1994) and (Robeson 2008). The major problem limiting use of organic polymer membranes for hydrogen separations is their maximum working temperature. Most polymers degrade at temperature above 300 °C . In the WGS process, for example, the operation temperature is around 800°C.(Ockwig and Nenoff 2007) Even carbon membranes could only survive temperatures to 500 ^{o}C.(Dolan et al. 2006)

Table 1.2 Permeability and separation factors for polymeric membranes

Polymer	P_{H2}(x10^9cm^3(STP)/[cm^{2}scmHg])	Separation factor (H_2/N_2)
Silicone rubbers	100-500	1.5-3.0
Hydrocarbon rubbers	50-300	2.0-4.0
Polyphenylene oxides	50-100	10-20
Polyimides	10-100	50-200
Substituted polysulfones	20-70	15-25
Polycarbonates, polysulfones	0.5-20	25-75
Polyesters, nylons	0.5-3.0	50-150
Acrylonitrile copolymers	0.1-1.0	100->1000
PIM-7	860	20.5
PIM-1	1,300	14.1
Poly(trimethylsilylpropyne)	23,200	2.5

1.3 Inorganic membranes

Compared to organic membranes, inorganic membranes are more thermally stable and can withstand harsher environment. That gives inorganic membranes a wider range of applications than organic membranes. Here inorganic membranes are divided into non-metallic and metallic in materials. Examples of non-metal inorganic membranes are zeolites, silica, metal organic framework (MOF), and carbon molecular sieve (CMO) membranes. In these porous membranes performance is Knudsen-diffusion controlled. The separation factor for hydrogen from other components is better than that of other gases because of hydrogen's small molecular mass. Under standard conditions (of low temperature operation) porous inorganic membranes with pore size of 2-50 nm have no advantages over organic membranes with similar structure in gas separation performance. Because inorganic membranes are more resistant to higher temperatures, in which case

the permeability is higher. Zirconium oxides (ZrO_2), alumina (Al_2O_3), and silicon carbide membranes are commercially available.

Metal membranes include crystalline alloy and amorphous metallic membranes. (Dolan et al. 2006) Palladium (Pd)-based membranes are the bench-mark metallic membranes for hydrogen separation. Other metallic membranes are primarily body centered cubic (BCC) structured alloys that include vanadium-nickel (V-Ni) binary alloys, V-Ni-based alloys, and niobium (Nb)-based alloys. For non-Pd based metallic membranes a catalytic coating, usually Pd, with thickness approximately hundreds of nanometers is applied on both surfaces of the membrane to promote H_2 dissociation and recombination.

1.3.1 Non-metallic inorganic membranes

Zeolites are crystalline microporous aluminosilicates composed of TO_4 (T=Si,Al) tetrahedral units connected by oxygen resulting in pore frameworks. (Dong et al. 2008) More than 200 types of zeolite have been synthesized. Because of the porous framework structure which gives uniform molecular size, the zeolite is ideal for separation applications, although not many have been utilized as membrane materials. The MFI-type zeolite membrane is the most widely investigated membrane because the pore size (4.46Å) can separate many molecules important for chemical and petrochemical industries(Michalkiewicz and Koren 2015). The pore size of MFI (0.54 nm x 0.56 nm, 0.51 nm x 0.54 nm) is not ideal for H_2 from light gas mixture, some high selectivities is from the orientation of the zeolite and the amorphous species. Thus modification has been applied to change the pore size. (Masuda et al. 2001)

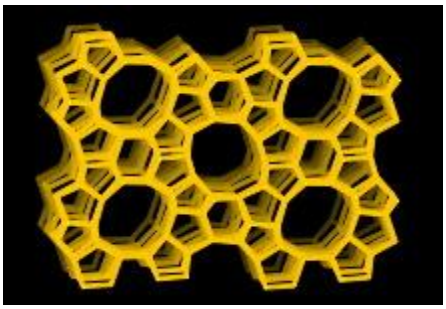

Figure 1.3 Chemical structure of MFI. Image reproduced from (Baerlocher and Mccusker)

MOFs (metal-organic frameworks) consist of a metal ion/cluster connected by organic linkers which can form 1-, 2- and 3-dimensional porous structures. Because of their highly tunable pore sizes and porosity, MOFs attract large interest for various applications. Some of the applications include: hydrogen storage, gas separation based on selective adsorption, and even catalysis.（Eddaoudi et al. 2002; Rosi et al. 2003; Lee et al. 2009; Li et al. 2009）. Zeolitic imidazolate frameworks (ZIFs) are a sub-family of MOFs. The structure of ZIFs consists of transition metal ions (Co^{2+}, Cu^{2+}, Zn^{2+}, etc.) and imidazolate linkers which form tetrahedral framework similar to zeolites with pore sizes of 0.2-1.5 nm.

CMSs (carbon molecular sieves) are porous solids which contains pore constrictions comparable to the diffusion path length of gases. The membranes are usually synthesized from pyrolysis and carbonization of polymer precursor membranes under a non-oxidative atmosphere(Jones and Koros 1994). Figure 1.4 is reproduced from (Kiyono et al. 2010) and shows the schematic pore structure of an ideal CMS. The pore

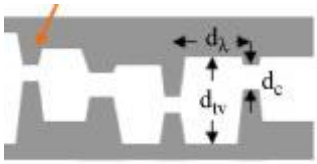

Figure 1.4 Schematic drawing of CMS pore structures reproduced from (Kiyono et al. 2010)

structure of CMS membrane is idealized to be slit-like. In CMSs the pore constriction, as is shown in Figure 1.4, is the critical dimension (d_c). This d_c , which performs the sieving action in the CMS, is comparable to the kinetic diameter of the diffusion molecules. The selectivity of CMS is measured to be much higher than the selectivity conventional polymeric membranes. Because of their unique structure, CMS membrane performance exceeds the Robeson upper bound. Parsley et al. prepared full-scale CMS modules and field tested the modules with syngas and found that the process delivers more than 90% of hydrogen recovered with purity greater than 90%. (Parsley et al. 2014)

1.3.2 Pd-based and other crystalline dense metallic membranes

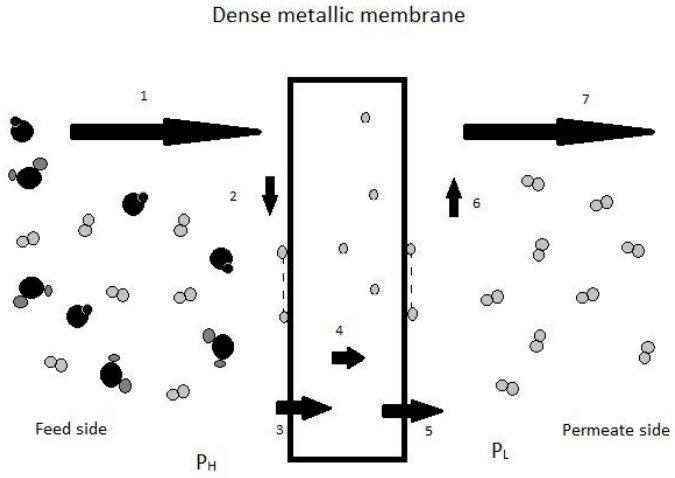

Figure 1.5 Schematic showing the process of hydrogen separation and diffusion through a dense metallic membrane. reproduced from (Phair and Donelson 2006). Step 1: H_2 transfer to surface; step 2 : dissociation of H_2 into atoms; step 3:adsorption of H atoms; step 4: diffusion of H atoms; step 5: desorption of H atoms; step 6: recombination of H_2; step 7: H_2 move away to downstream.

Metal membranes have the potential for very high selectivity provides the solution of manufacture fuel-level hydrogen. Figure 1.5 reproduced from (Phair and Donelson 2006) schematically shows the process of hydrogen separation through dense metallic membranes. There are 7 steps in total i) H_2 transfer to the surface of the feed side;

ii) H_2 dissociate into H atoms; iii) H atoms transfer into membrane bulk; iv) H atoms diffuse through the membrane; v) H atoms transfer into the surface of the permeate side; vi) H atom recombination into H_2 vii) H_2 leaves the surface of the permeate side. The following paragraphs will cover 1) Pd-based crystalline membranes and 2) Non-Pd-based crystalline membranes.

1.3.2.1 Pd-based membranes

Figure 1.6 A hydrogen purifier from Jonson-Matthey Company

Pure palladium membranes have been commercially available since 1960s. Figure 1.6 is a picture of a small-scale hydrogen purifier, manufactured by Johnson-Matthey in the United States, that uses palladium alloy membranes. Pure palladium is highly permeable to and selective for hydrogen at high temperatures (400 °C-700 °C)with infinite H_2/N_2 selectivity and permeability of ~ 10^{-8} mol m^{-1} s^{-1} $Pa^{-0.5}$. (Dolan et al. 2006) The high selectivity and flux enables Pd membranes to be used in some process which requires high purity hydrogen. The Pd can withstand high temperature (400 ℃ plus) and can be made into a module and incorporated into the syngas facility to produce hydrogen more efficiently because constant removal of hydrogen from the syngas production can accelerate the reaction speed.

However, there are some problems with palladium. First, the high cost of Pd hinders the large-scale application. Also, the Pd–H system features an α (interstitial solid solution)-β (Pd hydride) phase transformation below 293°C, e.g. there is a miscibility gap. (Alashab and Harris 1988; Lewis 1995) Figure 1.7 from ASM handbook shows the phase diagram of Pd-H. Both α and β phases have face center cubic (FCC) crystalline structures. But there is lattice mismatch between the two phases. Pure Pd has a lattice parameter of 3.89 Å. The α phase exists up to the H/Pd ratio of 0.02 when the α phase has the maximum lattice parameter (α_{min}) of 3.895 Å. β phase exists at a range of H/Pd = 0.6 at which the β phase has minimum lattice parameter (β_{min}) of 4.025 Å. At room temperature, the maximum mismatch between the α and β phases is when the H/Pd atomic ratio is around 0.6. The lattice expansion mismatch of the two phases of palladium gradually generates micro-cracks which ultimately results in mechanical failure after long time applications. To alleviate the problem of the lattice expansion and to suppress the α-β transition below room temperature and lower the price, various metal elements have been alloyed with palladium. Wise et al. alloyed Pd with Sc, Ti, Fe, Y, Zr, Ag, In, Ce, Eu and Gd. (Wise et al. 1975). They found Pd with 23 at% Ag undergoes only a 0.031% expansion during α-β transformation, which is the smallest among all the alloys compositions investigated. In addition to the Pd-Ag system, there are other Pd binary alloys that have hydrogen permeability higher than or comparable to pure Pd, for example, Pd-Au, Pd-Y, Pd-Cu and Pd-V.

Pd-Y is reported to have higher hydrogen permeability than Pd-Ag. Even though the Yttrium atom is 30% larger than Palladium atom, Y is soluble in Pd up to 12 at%. (Harris and Norman 1968) One of the problems with Pd-Y is that Pd-Y suffers from cold hardening which requires several annealing steps to enable it to be processed into membrane modules. So the manufacturing cost increases as a reault. Pd-Cu is another promising system. (Acha et al. 2012; Galipaud et al. 2013; Krisyuk et al. 2015) Pd-Cu is mechanically more durable than Pd-Y and Pd-Ag and also has comparable hydrogen permeability to pure Pd.(Al-Mufachi et al. 2015) An additional advantage of Pd-Cu is that it has more resistance to H_2S than pure Pd and Pd-Y. (Morreale et al. 2004) Atomic

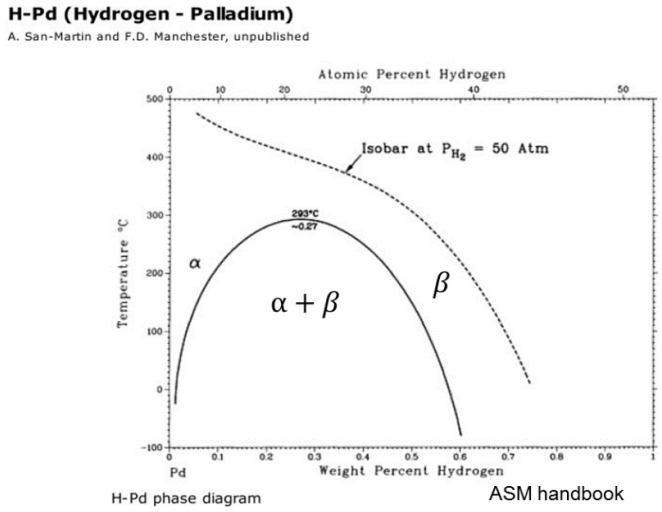

Figure 1.7 Pd-H phase diagram reproduced from the ASM handbook

modeling of sulfide interactions shows that the electronic characteristics of Pd-Cu has more influence than the surface site geometry.(Opalka et al. 2011) Besides binary Pd-based alloy membranes, ternary Pd-based alloys are under development. The major purpose of ternary alloy is to improve the stability under H_2S, decrease the raw materials cost without compromising hydrogen permeability. Sulphur tolerance investigation was conducted on Pd-Ag-TM (TM=Au, Y, Mo and Cu). With presence of 20 ppm H_2S,

$Pd_{75}Ag_{22}Au_3$ has the permeability of $1x10^{-9}$ mol m^{-1} s^{-1} $Pa^{-0.5}$ which was two order of magnitude higher than $Pd_{77}Ag_{23}$ at the same condition, three percentage of Au addition could improve the Sulphur resistance.（Peters et al. 2013; Braun et al. 2014）Another ternary system is Pd-Cu-TM (TM=Au, Ag, Ru, Mo, Ta and Y). With the addition of small amount of Ta and Y to Pd-Cu alloys, an increase of 10%-45% in permeability was observed. $Pd_{65}Cu_{21}Ag_{14}$ showed an increase of 65% in permeability ($4.7x10^{-9}$ mol m^{-1} s^{-1} $Pa^{-0.5}$) compared to the $Pd_{70}Cu_{30}$ at 673 K with membrane thickness of 2 μm.（Peters et al. 2011a; Guerreiro et al. 2014; Tosques et al. 2014; Zhao et al. 2014a; Tarditi et al. 2015a; Tarditi et al. 2015b）

To help selection of Pd-based alloys and understand the hydrogen interaction with Pd-based alloy membranes during transportation, theoretical study has also been conducted. Computation simulations majorly applied density functional theory (ab initio simulation(Cha et al. 2008)and first principle calculations(Hyman et al. 2007; Ling and Sholl 2007)). Also, modelling has been utilized to predict the mass transfer through the Pd-based membranes or the membrane separators.(Ayturk et al. 2009; Boon et al. 2012)Because Sulphur is the major contamination to metallic membranes, the sulphur interaction with Pd-based membrane surface was simulated by first-principles. Using first-principle calculations, Lovvik et al.(2014)found that elements addition like Cu, Zn etc. could improve the sulphur resistance of Pd-Ag membranes. Ling et al. (2011)calculated hydrogen permeability as a function of composition for ternary Pd-Cu-Ag alloys by first-principle theory. They found that the addition of Ag in Cu rich compositions help improve permeability, this is due to the solubility increase caused by higher Ag addition. Another density functional theory calculation by Chandrasekhar et al.

(2014) investigated 78 binary Pd intermetallics, but found no intermetallic has hydrogen permeability higher than pure Pd. These simulation work help eliminate the experimental work needed to screening the Pd-based compositions.

Pd-based metallic membranes are usually fabricated by depositing on substrate. To maximize the flux, efforts have been made to minimize the thickness. Thin films with thickness of 1-2 μm or ultrathin film under 500 nm Pd-based membranes are usually deposited on alumina (Jayaraman et al. 1995)or stainless steel (Tong et al. 2005)substrate to provide mechanical support. Common technology to prepare the Pd alloy thin film includes Physical Vapor Deposition (thermal evaporation, magnetron sputtering and pulsed laser evaporation), Chemical Vapor Deposition (CVD), electroplating and electroless plating (ELP). ELP is widely used because of its ability to deposit on supports with any shapes and the ease of operation with low cost. To achieve thinner thickness and promote better adhesion between the metallic film with the porous structure, improvement with deposition technologies as well as substrate optimization were utilized, including: novel seeding procedure (Abate et al. 2009), surfactant addition (Islam and Ilias 2010) and bath improvement（Tong et al. 2005; Volpe et al. 2006; Ryi et al. 2010）. Metal-Organic CVD has better film integrity compared to magnetron sputtering and ELP. (Huang and Dittmeyer 2007)Other techniques, for example, coating photolysis process (CPP) has been utilized to fabricate Pd film. CPP is conducted with two processes by first using spin-coater to coat substrate with metal-organic (MO) compounds solutions and then using an excimer laser or a UV lamp to irradiate the coated substrate. The laser or UV lamp would decomposes MO compounds and produce the metallic film on the

substrate.(Imai et al. 2006) Self-supporting Pd alloy can be fabricated through cold rolling and magnetron sputtering. (Gade et al. 2010)

In summary for Pd-based membranes: 1) the bench-mark metallic membranes with high selectivity (infinite H_2/N_2) and high permeability ($1x10^{-8}$ mol m^{-1} s^{-1} $Pa^{-0.5}$ at ~ 673 K); problems need to resolved: 2) high materials cost ; 3) the adhesion issue of the dense Pd alloy film with the substrate; 4) H_2S resistance. Several reviews covered different aspects of Pd-based membranes are introduced here. Paglieria and Way (2002) reviewed novel research related to Pd composite membranes; summarized fabrication techniques/issues and applications pertain to Pd-based composite membranes. Nenoff et al. , Basile and Tosti et al. reviewed Pd-based membranes for industrial applications, specifically in water gas shift reactions.（Nenoff et al. 2006; Basile 2008; Tosti et al. 2009）Recent review by Al-Mufachi et al.(2015)focused on the materials' aspect of Pd-based alloy membranes.

1.3.2.2 Non-Pd-based crystalline membranes

The body centric cubic (BCC) structure alloys are the most promising class of the non-Pd-alloys. Tungsten's (W) crystalline structure is a typical BCC structure. Besides W, vanadium, chromium, niobium and etc. all exhibit BCC structures. By comparison, pure Pd and most of the Pd alloys are FCC structure. The difference in crystalline structure results in the alloys having different numbers of tetrahedral and octahedral sites. BCC structures have 3 octahedral sites and 6 tetrahedral sites; while FCC structures have 1 octahedral site and 2 tetrahedral sites. Over all, the atoms in a BCC structure are less packed than in a FCC structure. Because of this the structure difference in atomic structure, the solubility of H atoms and their transport mechanism through is different in

the two crystalline structures. It has been reported that BCC alloys have higher hydrogen permeability than Pd-alloys. (Dolan 2010)

There are several pure metals with hydrogen permeability larger than pure Pd. Ta, V, Nb (Group V) and α-Fe have the BCC structures; followed by Ni which is a FCC structure (Pd is also in FCC structure). The problem with those pure metals, however, is that the large hydrogen solubility leads to hydrogen embrittlement and they form surface oxides and nitride which decrease the permeability over time.(Nishimura et al. 2002) Recent research shows that with Pd coating, pure Nb showed higher resistance to embrittlement. (Nambu et al. 2007). Nb-based and V-based alloys attract attention due to its potential as good hydrogen separation materials with lower materials cost compared to Pd-based alloys. First-principle calculations shows the pure Nb and pure V have good hydrogen solubility.(Ouyang and Lee 2011; Rao et al. 2012) The common metal elements are refractory metals, for example, W, Ta and Hf; and Ti, Zr metals which potentially could improve hydrogen permeability by its low hydride formation enthalpy; Al, Cu, Co and Fe for impurities resistance on surface. Pd-coating was also utilized. to promote hydrogen dissociation and recombination also surface resistance to impurities.（Tang et al. 2008; Ishikawa et al. 2009; Watanabe et al. 2009a; Watanabe et al. 2009b; Il Jeon et al. 2012; Suwarno et al. 2012; Kim et al. 2013; Li et al. 2015; Nakamura et al. 2015）The amount of substitution usually will keep the BCC structure to maintain the structure's advantage of good hydrogen solubility. The non-Pd crystalline membranes share the fabrication technologies with Pd-based membranes.

$V_{85}Ni_{15}$ is the bench-mark BCC alloy with embrittlement resistant that also has hydrogen permeability larger than pure Pd.(Ozaki et al. 2003) The hydrogen

permeability is 2-3 x 10^{-8} mol m^{-1} s^{-1} $Pa^{-0.5}$ at 673 K. Partially substituting Ni in the $V_{85}Ni_{15}$ with Al or Nb improves the hydrogen permeability. (Ozaki et al. 2003; Yukawa et al. 2009) Also dopants of Ti, Zr and Y would promote hydrogen permeability. Besides the ternary additions, a quaternary addition is also under investigation to optimize the composition. One of the major concerns is always the interaction between the H atoms and the metal which may cause embrittlement and hinder the application as a membrane material.

1.4 Amorphous metals

Amorphous metals are formed by rapidly cooling a molten alloy to bypass crystallization. These materials have unique thermal, crystallographic, and mechanical properties. The first amorphous metal developed was the Au-Si alloy which was found in 1960 by Klement et al. at the California Institute of Technology(Klement et al. 1960). To achieve very high critical cooling rates of 10^5-10^6 K/s, molten alloys were spread on substrates which have high thermal conductivity(Tosti 2010). The rapid solidification technology later developed into a commercial planar flow casting technology which produces ribbons and sheets of amorphous alloys.(Michalkiewicz and Koren 2015) Many more binary and ternary amorphous-metallic alloy forming compositions have been developed since the 1960s. Alloys ($(Pd_{1-x}M_x)_{0.835}Si_{0.165}$, M=Ni,Co and Fe) that cool into amorphous metals at much lower critical cooling rates (~1000 K/s) was achieved by mold suction casting and their dimension could reach up to 1 mm(Chen 1974). Then, in the 1980s, William Johnson's group at Caltech developed Zr-based alloys with critical the cooling rate below 100 K/s with the largest dimension to centimeters(Johnson 2002a).

Around the same time, the Inoue group in Japan conducted a series of research on multicomponent amorphous metals; they fabricated bulk metallic glass with a variety of alloys based on Mg, Zr and La. A bulk metallic glass (BMG) is defined as an alloy system can be cast amorphous into a minimum dimension of one millimeter.

The primary application of amorphous metals during 1970s to 1980s was as soft magnetic properties for transformer cores and magnetic devices. Later, their good

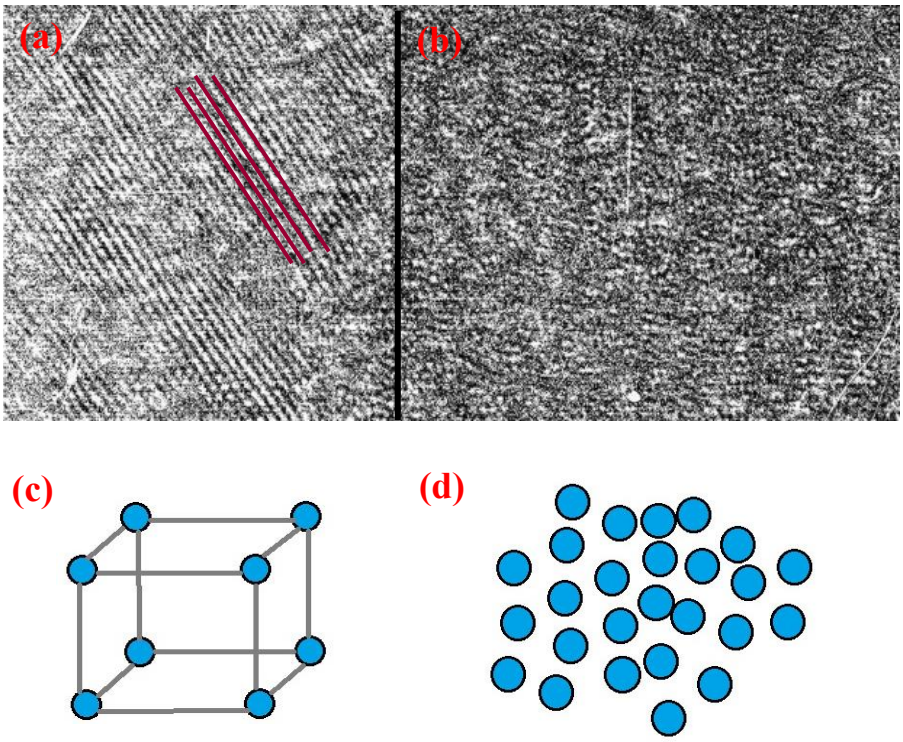

Figure 1.8(a) TEM image of crystalline materials at 5Xmillion; (b) TEM image of amorphous material at 5Xmillion; (c) schematic drawing of a crystalline material with simple cubic unit cell; (d) schematic drawing of atoms in amorphous material reproduced from (Peker 1994)

mechanical properties drew large attention. Some of the parameters, for example, plane-strain fracture toughness of amorphous metals are much higher than that of ceramics, oxides and other materials. The potential to use amorphous alloys as structural engineering materials is one of the motivations to continue to further develop BMGs. One

of the most successful composition is Vitreloy 1:$Zr_{41.2}Ti_{13.8}Ni_{10}Cu_{12.5}Be_{22.5}$(Peker and Johnson 1993). The alloy Vitreloy 1 has been applied to fabricate items such as pipes, golf clubs, and cell phone hinge pins by Liquid Metal Technologies, CA.

This following section will first introduce major structural, thermal and mechanical properties of amorphous metals and their application as hydrogen separation membrane materials.

1.4.1 Structural, thermal and mechanical Properties

Amorphous metals, also called liquid metal or metallic glass (MG), are metallic alloys with a atomic structure significantly different from crystalline metals and are in a thermodynamically metastable state. There is no long-range atomic order in amorphous metals. The atoms packed randomly, appearing more like a frozen liquid.

Figure 1.8shows the transmission electron microscope (TEM) images reproduced from (Peker 1994) and schematic pictures of atoms in crystalline metals in (a),(c) and amorphous metals (b),(d). The lines on Figure 1.8 (a) are the evidence of atoms arranged in ordered manner. In a perfect crystal, the position of atom can be defined relative to other atoms. While in Figure 1.8 (b), there are no patterns of the atoms, all the atoms are randomly packed, similar to glass or a liquid. The reason this occurs is that the high cooling rate, as mentioned before, freezes the structure of alloys above melting point. This process could also be explained by Free volume model. (Turnbull and Cohen 1961) Free volume v_f is defined as that part of the thermal expansion, or excess volume $\Delta\bar{v}$ that can be redistributed without energy change. This model described the glass transition from liquid to amorphous state as the decrease of free volume. When the

free volume does not decrease anymore and the crystallization does not intervene, the amorphous state formed.

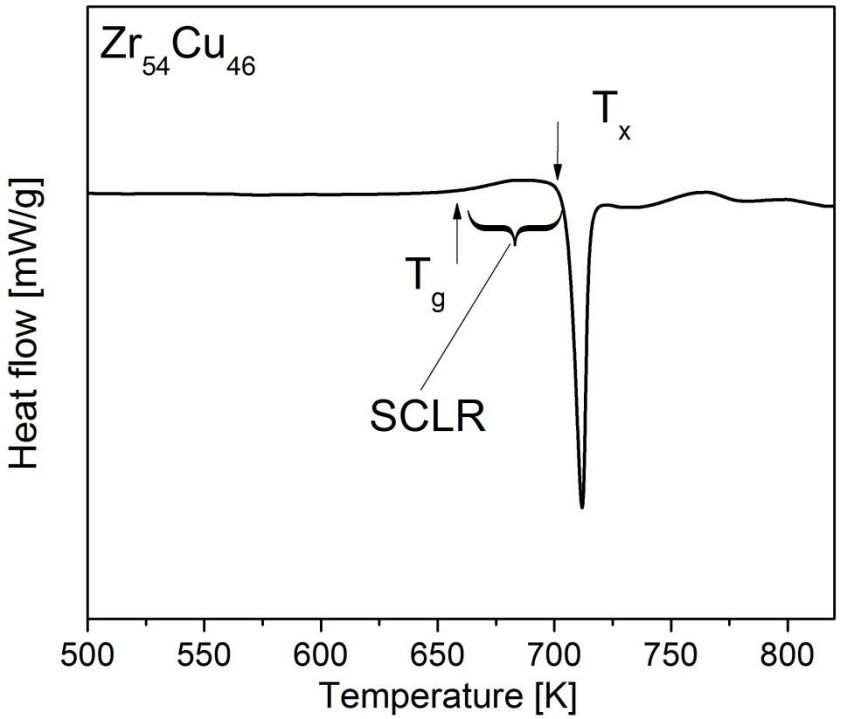

Figure 1.9 DSC curve of a $Zr_{54}Cu_{46}$ amorphous metallic membrane

The glassy structure of amorphous metals results in some important properties for amorphous metals that crystalline metals do not have. Because these materials are thermodynamically metastable, they have a super cooled liquid region (SCLR) which is bound by the glass transition temperature (T_g) (on the low end) and crystallization temperatures (T_x) (on the high end). T_g is defined as the temperature at which viscosity becomes $1012Pa^{-s}$(Ojovan 2008). Above T_g, and below T_x, the material behaves more like liquid with high viscosity, however it is still not in liquid state. Crystallization is irreversible, once the temperature is higher than T_x, the atoms become ordered. Figure 1.9 shows a characteristic differential scanning calorimetry (DSC) curve of an amorphous

$Zr_{54}Cu_{46}$ alloys with ramp rate of 0.33 K/s at N_2 atmosphere. Key features of Figure 1.9 are the glass transition and crystallization events.

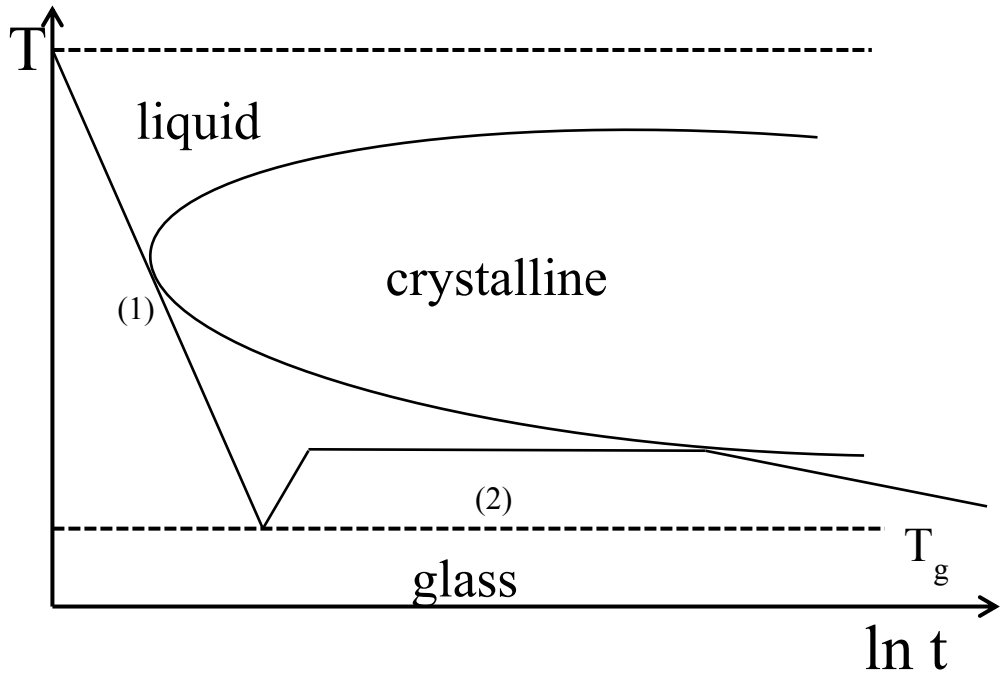

Figure 1.10 Schematic drawing of Time-Transition-Temperature curve

As mentioned before, different alloys have variations in minimum critical cooling rate required to become amorphous. This is called glass forming ability (GFA). The better the GFA, the lower the critical cooling rate, and the easier an alloy system can be fabricated amorphous. The critical cooling rate (and corresponding GFA) strongly depends on the alloy composition. There are several methods to evaluate the GFA. Reduced glass transition temperature, defined as T_g/T_x, has shown strong correlation with GFA. (Lu et al. 2000) Also, time-transition-temperature (TTT) curve, both experimentally tested and computational calculated, can show an estimate for determining the GFA. Figure 1.10 shows a schematic drawing of a TTT curve. The 'nose' of the TTT curve determines the critical cooling rate (line (1)). Only when the cooling

rate is larger than the critical cooling rate, the system could bypass the crystalline region from the liquid state and becomes glassy state. Line (2) illustrates that during a long annealing process the amorphous alloy can be also crystallized. It is well established that holding an amorphous metal at the T_g or at temperatures within the SCLR for long times results in crystallization(Murali and Ramamurty 2005).

Mechanical properties are one of the areas in which liquid metals have drawn extensive attraction. Liquid metals usually have similar elastic moduli compared to their crystalline counterparts, however, the room-temperature yield strength generally exceeds its conventional engineering polycrystalline compartment. The potential to exhibit high strength and good toughness at the same time has inspired much research of room-temperature applications(Johnson 2002b). Figure 1.11 reproduced from John's group website shows the elastic limit and strength of glassy alloys compared to other common materials.

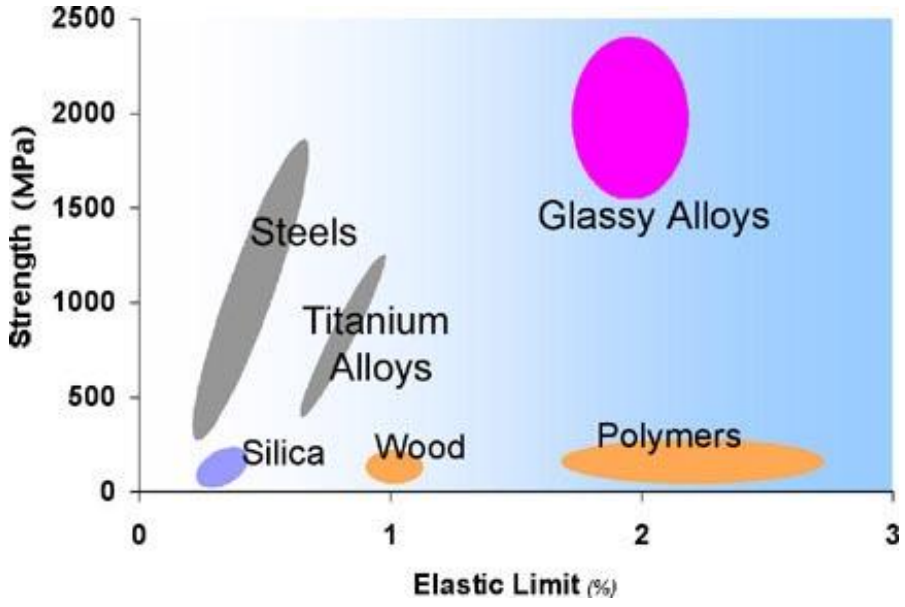

Figure 1.11 Elastic limit and strength of glassy alloys compared to some conventional structural materials figure reproduced from
http://www.its.caltech.edu/~vitreloy/development.htm

The deformation of crystalline metals depends on the defects and dislocations, which amorphous metals do not have. So the strain needs to be readily accommodated at atomic level. The exact atomic motion during the deformation of an amorphous metal is not yet fully understood. One explanation is that the deformation occurs as configurations' change of "shear transformation zone" (STZ)(Argon and Kuo 1979). A STZ allows inelastic shear distortion from low energy configurations. Computational models have been employed to investigate the deformation of amorphous metals. STZs with a few or hundreds of atoms are observed in simulation works. STZs are not specific structure in amorphous metals, but they can be observed during the strain process. Besides STZ, the free-volume model has also been applied to help describe the mechanism of plastic flow(Spaepen 1977). This model regards deformation as a series of discrete atomic jumps in the amorphous metals. The free volumes act similar to the defects in crystalline materials. There are also atomic-level quantitative model which combines the two models(Schuh et al. 2007).

1.4.2 Amorphous metallic membranes for hydrogen separation

Amorphous metals are another alternative to replace palladium-based membranes. Density functional theory calculations and quantum Monte Carlo simulations have demonstrated that amorphous metallic films can have hydrogen permeability close to pure Pd, and predict less hydrogen-induced expansion compared to their crystalline counterparts.(Hao and Sholl 2011a) Experimentally, Hara et al. found that the amorphous alloy $Zr_{36}Ni_{64}$, without a Pd surface coating, has hydrogen permeability only one order of magnitude lower than $Pd_{77}Ag_{23}$ at 350°C.(Hara et al. 2000) With its unusual atomic

arrangement, more channels are available for hydrogen diffusion, thus higher flux may achievable for amorphous metals.

The model of hydrogen permeation in amorphous metals is based on the solution-diffusion mechanism, assuming that all the other processes are faster than the diffusion rate. One of the important parameters to quantify the performance of hydrogen permeation membranes is steady-state flux (J) of hydrogen through the membrane. And the flux can be measured directly by using a permeation cell. J (mol/m^2s) represents moles of H_2 permeating through a certain area of membrane at given temperature and applied pressure difference. Fick's law can be used to describe the transport of hydrogen:

$$J = D\frac{\partial C}{\partial x} \quad (1.1)$$

Where D is the diffusion coefficient in unit m^2/s, C is concentration gradient, x is the distant. The concentration gradient is the result of pressure gradient, and Sievert's law describes the relationship between concentration and pressure.

$$C = K\sqrt{P} \quad (1.2)$$

Here, K is a temperature dependent constant, called Sievert's constant. By substitute equation (1.2) into (1.1) the following relationship between flux and pressure turns out.

$$J = \frac{DK}{t}(\sqrt{P_H} - \sqrt{P_L}) \quad (1.3)$$

Here *t* is the thickness of the membrane. P_H is hydrogen partial pressure at feed side, P_L is hydrogen partial pressure at permeate side. Ward and Dao refer to the quantity *DK* as the Sievert's law permeability, $\bar{P}$. Although hydrogen flux can be detected directly, permeability is more practical to refer to when comparing different membranes, because the thickness varies between membranes.

As is stated before, equation (1.3) is for the ideal situation in which bulk diffusion is the rate limiting step to permeation. Complications of the membrane need to be considered, for example, surface morphology, grain boundaries, microcracks. On the downstream side, the removal can also affect the model used. A more general model was stated by the following equation:

$$J = \frac{\bar{P}}{t}(P_H^n - P_L^n) \quad (4)$$

The number of exponent n indicates the rate-limiting step. Deviation from 0.5 may due to non-diffusion-limited permeation process or change of Sievert's constant caused by pressure and temperature change.

Various alloy systems have been experimentally investigated for hydrogen purification. $Zr_{36}Ni_{64}$ ($1.2x10^{-9}$mol m^{-1} s^{-1} Pa^{-05}) membranes have comparable permeability with $Pd_{77}Ag_{23}$ ($15x10^{-9}$ mol m^{-1} s^{-1} Pa^{-05}) membrane at 623K. Because Zr easily forms hydride and causes fast failure by embrittlement, some refractory metal elements were substituted for part of the Zr. A series alloys were investigated based on the Zr-Ni system. Dolan et al. investigated partial substitution of Zr with Ti, Nb, Mo, Hf, Ta or W. They found Nb, Hf and Ta increased the glass transition temperature. Ti substitution decreased the T_g. Mo and W substitution leads to serious embrittlement. The Nb substitution was not detrimental to the hydrogen permeability and also improved hydrogen permeability.(Dolan et al. 2009b) Because Ni-Nb-Zr alloys have shown good hydrogen permeability while maintain the amorphous structure. Dolan et. al (2009a) investigated the hydrogen permeability of $Ni_{60}Nb_{40-x}Zr_x$ (X=0,10,20 and 30). The compositions with Zr concentration of 30 shows the local maximum pure hydrogen permeability of $6x10^{-9}$ mol m^{-1} s^{-1} Pa^{-05} at 673 K. However, the thermal stability over

time during the hydrogen permeability decreased as the increasing concentration of Zr. So a compromise of hydrogen permeability and thermal stability needs to be made. Hara et al. substituted hafnium (Hf) for Zr in the ZrNi alloy. All the $Zr_{36-x}Hf_xNi_{64}$ ($0 \leq x \leq 36$) membranes showed stable permeability to hydrogen in the range of 200-300°C. Over 573 K, the permeation rate slowly decreased over time. Permeability was found to decrease with Hf substitution for part of the Zr. Another ternary alloy system is Ni-Nb-based. This is because the $Ni_{60}Nb_{40}$ has good glass forming ability as well as high glass transition temperature which makes the Ni-Nb-based alloys have potentially better thermal stability. Zhang. W et al investigated the glass-forming ability (GFA) of the $Ni_{60}Nb_{40-x}Ti_x$(x = 0 to 40) glassy alloys(Zhang and Inoue 2002). As the Ti content increases, the super-cooled liquid region and reduced glass transition temperature increase, the maximum ΔT_x (super cooled liquid region area) of 54 K are obtained at 22.5 at% Ti and 15 at% Ti, respectively. For $Ni_{60}Nb_{25}Ti_{15}$ glassy alloy, the T_g and T_x of the bulk glassy alloy were 859 K and 906 K, respectively.

Quaternary and multi component-alloy systems with improved glass forming ability have also been investigated for the potential for hydrogen separation. For example, the addition of Ta or Co with Ni-Nb-Zr to for the purpose of increased thermal stability. $Nb_{42}Ni_{40}Co_{18-x}Zr_x$ (x = 0, 4, 12 or 20) and $Nb_{42}Ni_{32}Co_6Zr_{12}M_8$ (M = Ta, Ti, Zr) series amorphous alloys with major component of Nb were fabricated by melt-spinning.(Ding et al. 2013) The experimental hydrogen permeability of the $Nb_{42}Ni_{32}Co_6Zr_{20}$ alloy is 1.14 x 10^{-8} mol m^{-1} s^{-1} $Pa^{-0.5}$. The permeability of the Nb-Ni-Co-Zr-M alloys during the permeability test after 24 hrs decreased to 60% of the initial value while it still maintains amorphous structure. Thermal stability and mechanical properties of various

compositions of Ni-Nb-Ti-Hf bulk glassy alloys have also been investigated(Zhang and Inoue 2003). The max T_g (875K) and T_x (926K) in this system is achieved at composition of $Ni_{60}Nb_{20}Hf_{15}Ti_5$, the SCLR has a width of 51 K. Nb-rich Nb-Ni-Ti alloys exhibit good hydrogen permeability. The preparation of Ni–Nb-based metallic glass wires by arc-melt-type melt-extraction method has been investigated which means the fabrication of Ni-Nb-based metallic glass won't be an obstacle(Nagase et al. 2009).

Palladium is usually coated on the surface of those amorphous metallic membranes to provide catalytic effect. Pd with ~ 100 nm thickness can help H_2 dissociation before diffusion through the membrane and recombination of H_2 to leave the membranes. Pd also prevents oxidation. Besides Pd, other metal elements also have catalytic effect of H_2 dissociation. Based on that, Yamaura et al. (2010) used Ni as the coating on amorphous $Ni_{40}Nb_{20}Ta_5Zr_{30}Co_5$ and compared the hydrogen permeability with those coated with Pd.(Yamaura and Inoue 2010) The Ni-coated samples exhibited hydrogen permeability one order of magnitude lower than the Pd-coated sample. Also, because Ni atoms can diffuse into the membranes easier than Pd atoms, this results in faster degradation of catalytic activity of the Ni-coatings than the Pd coatings. They found that the catalytic effect of element deposited on the surface seems more important on permeate side of the membrane than feed side of the membrane. Adibhatla et al. (2014) used heat treatment in H_2 atmosphere to activate catalytic effect of the surface Ni. The heat treatment promotes the development of sub-micron Ni particles at the surface and drastically increased the catalytic effect. (Adibhatla et al. 2014)While heat treatment at certain temperature lower T_g at H_2 would cause crystallization. So caution needs to be made to determine the heat treatment temperature and duration. The appropriate

treatment condition which promotes surface enhancement while does not cause bulk crystallization showed improved hydrogen permeability. Those research indicate that surface morphology is crucial for hydrogen transfer between gas and solid phases.

Due to the random arrangement of atoms in amorphous metals, the behavior of hydrogen transport through the amorphous membranes is totally different from that in crystalline metals. In crystalline metals, the hydrogen solute in the metal by occupying the tetrahedral sites. As mentioned before, the BCC structure provides more closely packed tetrahedral than that in FCC structure, thus those sites have lower activation energy. With low activation energy, BCC structure provides a large tunneling contribution to hydrogen solution.(Naito et al. 1998) In amorphous metals, those interstitial sites still exist but are in irregular shapes and possess different site energy. The Harris model assumes the amorphous metals are made up of distorted tetrahedral.(Harris et al. 1987) The solubility of hydrogen depends on the probability of finding a tetrahedral site favorable for hydrogen to occupy. The diffusion of hydrogen in amorphous metals deviates from Arrhenius-type behavior which is followed by crystalline structure. This is due to the distorted tetrahedral sites and inconsistent site energy.(Eliaz et al. 1999) Not all the hydrogen dissolved is diffusible.(Wang et al. 2013) The hydrogen diffusion in amorphous alloys strongly depends on the hydrogen that dissolved than crystalline, the diffusivity increases as the hydrogen concentration increases.(Dolan et al. 2006; Lee and Lee 2014)

There are still not too much experimental research on the relationship between alloy composition and the solubility/diffusivity. Only limited information, for example, in Ni-Nb-Zr amorphous alloys the higher the Zr concentration the higher the hydrogen

permeability, was established. Thus the computational simulation becomes a useful tool to deal with multicomponent non-ordered structure. Theoretically, Prof. Sholl's group in Georgia institute of technology does a lot of work to predict the hydrogen permeability of amorphous metals by first principle modeling. Their methods do not need experimental parameter inputs and is comparable to the permeability of Ni-Zr and Ni-Nb-based amorphous alloys. One shortcoming of computational modeling is on the thermal stability of amorphous metallic membranes. Though the simulated temperature is usually lower than T_g, under hydrogen atmosphere, the structure change induced by hydrogen atoms solute into the bulk is usually not considered into the calculations. So the calculation gives the ideal situation where the hydrogen permeability does not degrade during the hydrogen permeation which is not very practical. Improved methodology incorporates thermodynamic calculation and molecular dynamic simulations. (Lee et al. 2014) Still, the computational modeling sheds light to the amorphous alloy system which potentially have good hydrogen permeability.

In summary, some of the amorphous alloys have hydrogen permeability comparable to Pd-based membranes. The thermal stability (crystallization) at hydrogen atmosphere and elevated temperature is a hurdle to long-term use. Compositions can form BMG and contain refractory elements may improve the stability. Catalytic coating, for example, Pd is necessary to overcome the hydrogen dissociation. Other methods by using different metal elements or heat treatment may also bring fundamental research on the interaction between hydrogen and amorphous metals at elevated temperature needs to be done. The fundamental research on hydrogen amorphous metals interaction will help give insights on how to better design the composition of the amorphous alloys.

1.5 Research objectives and significance

The overall goal of this research is to investigate the potential of binary and ternary amorphous metallic membranes for hydrogen separations. To better understand the relationship between energetic state of amorphous metallic membranes with hydride formation and crystallization during hydrogen separation process.

Previous research has shown that amorphous metallic membranes have the potential to separate hydrogen. But, hydride formation and crystallization inhibit the stability of amorphous membranes, thus limiting their hydrogen separation performance. Because of the different thermal, mechanical structural properties of amorphous materials compared to crystalline materials it is necessary to perform investigations of promising binary and ternary amorphous metallic systems.

Objective 1 is to investigate the surface influence on $Pd_{77}Ag_{23}$ crystalline metallic membranes and set-up the experimental apparatus for hydrogen permeability test. As mentioned in the previous sections, $Pd_{77}Ag_{23}$ crystalline metallic membranes for hydrogen separation. To investigate construct an experimental and theoretical procedure which could collect the hydrogen permeability of free-standing metallic membranes.

Objective 2 is to evaluate hydrogen permeation, thermal stability and mechanical properties of amorphous metallic membranes. Two series of alloy systems have been chosen. Cu-Zr binary system has shown potential good hydrogen permeability via first functional theory calculation. NiNb-X, with low substitution of Nb by Sn, Ti and Zr, has better thermal stability than Cu-Zr. The Sn substitution does not improve either hydrogen permeability or the mechanical properties of the $Ni_{60}Nb_{40}$ system. Various characterization methods have been applied. For example, X-ray diffraction, Differential

Scanning Calorimetry, Rutherford Backscattering, Scanning Electron Microscopy, and nanoindentation.

The following chapters will serve to address the objectives mentioned above. Chapter 2 fulfills objective 1 – investigate the surface state promoted by heat treatment and the influence on the hydrogen permeability of $Pd_{77}Ag_{23}$. Chapter 3 and 4 address objective 2. Several series of amorphous alloys systems which shows potential good hydrogen permeability have been investigated. Also, the thermal stability and the importance of surface states have been discussed. Chapter 5 summarizes the work reported in this thesis and provides recommendations for future advancement of the amorphous metallic membranes for hydrogen separation.

1.6 Structure of Chapters

The chapters in the dissertation are modified versions of the following papers published or to be submitted for publication:

Chapter 2

Lai, T. and M.L. Lind, Heat treatment driven surface segregation in $Pd_{77}Ag_{23}$ membranes and the effect on hydrogen permeability. *International Journal of Hydrogen Energy*, 2015. **40**(1): p. 373-382.

Chapter 3

Lai, T. Yin, H and M.L. Lind, The hydrogen permeability of Cu-Zr binary amorphous metallic membranes and the importance of thermal stability (In press in *Journal of Membrane Science*)

Chapter 4

Lai, T , Tianmiao Lai, Sudhanshu Singh, Arun Sundaram, Kaushik Sridhar Vadari, Nikhilesh Chawla and Mary Laura Lind, The hydrogen permeability and mechanical properties of NiNb-X(X=Sn,Ti and Zr) amorphous metallic membranes. (In preparation)

CHAPTER 2 THE EFFECT OF SURFACE STATE ON THE HYDROGEN PERMEABILITY OF $PD_{77}AG_{23}$ CRYSTALLINE METALLIC MEMBRANES

2.1 Introduction

As discussed in the introduction, $Pd_{77}Ag_{23}$ is the bench-mark metallic membranes for hydrogen separation. Surface diffusion could affect hydrogen permeability. And the surface composition, morphology and impurities of Pd-based membranes are factors that can influence surface diffusion.（Roshan et al. 1983; Paglieri and Way 2002） Surface diffusion is dominant when bulk diffusion is not the rate-limiting factor for permeation.(Ward and Dao 1999) This is one of the causes that results in deviations of experimental separation behavior from Sievert's law.（Mardilovich et al. 1998; Wu et al. 2000; Chi et al. 2010） According to the model proposed by Ward and Dao (1999), mass transfer is the rate limiting step for membranes when the membrane thicknesses is larger than 1 μm and at temperatures above 300 °C. There is other research showed that the surface state impacts wider thickness and temperature ranges.(Mejdell et al. 2008) H Amandusson et al.(2001) found that permeability of pure palladium membranes increased after depositing silver on the surface. They concluded that the hydrogen permeation was surface reaction controlled above 473 K.

Air treatment is a common procedure to promote hydrogen permeability of Pd-based membranes;（Mejdell et al. 2008; Tucho et al. 2009a; Tucho et al. 2009b; Ramachandran et al. 2010; Zhang et al. 2012a） it also improves the carbon monoxide (CO) resistance of Pd-based membranes.(Mejdell et al. 2010)Two hypothesized causes lead to the improvements after air treatment (1) carbon removal from the surface or (2)

changes in the surface roughness of the membrane(Mejdell et al. 2008). When exposed in air, Pd surfaces tend to collect hydrocarbons from the air.(Antler 1982) Air treatment can oxidized the adsorbed carbons into gas on surface.(Musket 1976) L. Yang et al. (2005)analyzed elements on Pd membrane surfaces by X-ray photoelectron spectroscopy (XPS), they attributed hydrogen permeability improvement to carbon elimination. Surface roughness is another possible explanation proposed for increased hydrogen permeability.(Mejdell et al. 2008) But the extent of the surface area increase was insufficient to explain hydrogen permeability increase(Roa and Way 2005). Higher sorption rates after air treatment may also explain the higher hydrogen permeability.(Ramachandran et al. 2010; Tarditi et al. 2012; Zhang et al. 2012a; Zhang et al. 2012b)

Surface segregation of elements in alloy membranes changes the surface composition as the result of the interaction with gases at high temperature.(Roshan et al. 1983) Theoretically, silver tends to segregate to the surface of Pd-Ag membranes because silver has a lower surface energy than palladium.(Vitos et al. 1998) This is observed by Ag segregation to the surface of Pd-Ag membranes after vacuum annealing.(Tarditi et al. 2012) However, after air treatment, Pd is enriched on the surface of Pd-Ag membranes.(Ramachandran et al. 2010; Tarditi et al. 2012) Similar segregation phenomena have been observed in Pd-Rh.(Joshi et al. 1986) After hydrogen permeation tests J. Shu et al.(1993) observed that Pd segregated to the surface of 50 μm $Pd_{75}Ag_{25}$ membranes. Løvvik et al. (2008) used first principle band structure calculations that support that Pd segregation happens at the surface in the presence of hydrogen. Other experimental studies, however, showed that Ag segregated after hydrogen permeation

tests.（Peters et al. 2009; Peters et al. 2011b） Ag segregation even happened after inert gas annealing (N2/Ar) at 300-450 °C and hydrogen permeability decreased afterwards. In summary, the literature shows conflicting segregation behavior results from different treatment temperatures and atmospheres.

The goal of this chapter is to investigate the impact of surface segregation on hydrogen permeability of crystalline $Pd_{77}Ag_{23}$ membranes. Although research has been done on segregation phenomena and surface state change, the relationship between segregation and hydrogen permeability has neither been fully understood nor established. Heat treatment at various conditions can trigger different segregation behaviors. In this study, heat treatment was conducted for the purpose of promoting either Pd or Ag segregation on the membrane surface. Surface composition and roughness information before and after the heat treatments was collected. Hydrogen permeability tests were performed to investigate the impact of heat treatment. After heat treatment, hydrogen permeability decreased when the surface composition was enriched with Ag and hydrogen permeability improved when the surface composition was enriched with Pd.

2.2 Experimental

2.2.1 Materials

$Pd_{77}Ag_{23}$ (thickness of 25 μm) alloy membranes were purchased from Alfa-Aesar. The samples were handled with gloves during the operations to limit carbonaceous surface contamination. Bulk composition of the membranes was verified with Particle-induced X-ray emission (PIXE, accelerator is a 1.7MV Tandetron by General Ionex Corporation). Table 2.1 summarizes the four different heat treatments that was conducted

on the samples. In the rest of this paper samples with A, B, C and D were denoted as indicated in Table 2.1 Samples A were the as-received membranes. Samples B were subjected to air treatment. Membranes were heated in a muffle furnace (Thermo Scientific, Thermolyne Furnace, Type F48000) at 1 atm and 400 °C (with a ramp rate ~4°C/min)for 24hrs then naturally cooled down. Samples B group has different heat treatment duration, Samples B.1 were annealed in the 400 °C muffle furnace for 10 minutes, and Samples B.2 were annealed in the 400 °C muffle furnace for 30 minutes. Samples B.1 and B.2 were added to the furnace after the furnace reached the annealing temperature and removed them from the furnace at the end of the annealing time and air-cooled in the laboratory environment. Samples C were vacuum annealed in order to promote Ag segregation of Pd-Ag alloy（Vitos et al. 1998; Svenum et al. 2012）. For vacuum annealed Samples C, the membranes were heated in a vacuum oven (Model EQ-DZF-6050-HT, MTI Corporation) at approximately 10-20 kPa vacuum level to 400 °C (with a ramp rate ~2°C/min), held them for 24 hours and cooled to room temperature with the oven. Samples D underwent 800 °C annealing in sealed quartz tube. Samples D were sealed inside a quartz tube under vacuum at a pressure of approximately 0.1 Pa and heated them in a muffle furnace (Thermo Scientific, Thermolyne Furnace, Type F48000) to 800 °C (with ramp rate ~4°C/min), hold for 24 hours and then water quenched the samples to room temperature. All samples were tested, at a minimum, in triplicate.

Table 2.1 Details of different heat treatments.

Sample	Temperature (°C)	Atmosphere (kPa)	Duration (hours)	Ramp rate (°C/min)	Cooling Method
A[a]	-	-	-	-	-

Table 2.1 Continued

Sample	Temperature (°C)	Atmosphere (kPa)	Duration (hours)	Ramp rate (°C/min)	Cooling Method
B	400	101	24	4	Inside furnace
B.1[b]	400	101	0.17	-	Air cool outside of oven
B.2[b]	400	101	0.5	-	Air cool outside of oven
C	400	10-20	24	2	Inside oven
D	800	$1x10^{-4}$	24	4	Water quenched
E	Sample B after hydrogen permeability test				

[a] as-received samples

[b] samples added to oven after oven reached annealing temperature

2.2.2 Characterizations

2.2.2.1 Surface composition

X-ray photoelectron spectroscopy (XPS VG ESCALAB 220i) were performed with an Al monochromatic source Kα (12 KV, 65 W, hν = 1486.6eV). The detector was perpendicular to the sample with spot size of 500 μm. survey scan and high resolution scans of Pd3d, Ag3d, C1s and O1s were obtained. Binding energy was calibrated with pure Ag with Ag $3d_{5/2}$ at 368.2eV (Nyholm and Mårtensson 1981) and Casa XPS software was utilized to analyze the composition and chemical shifts of elements. High resolution scans of Pd $3d_{5/2}$ and Ag $3d_{5/2}$ were used to calculate the atomic surface composition. Sensitivity factors were provided by the software library with Shirley-type baseline（Shirley 1972; Seah 1990）.

2.2.2.2 Surface morphology and roughness

Surface roughness was investigated with atomic force microscopy (AFM) in tapping mode (Digital Instrument dimension 3000) and image analysis was performed with the instrument software. All the images have been flattened in first order. Root mean square (RMS) roughness and surface area difference (SAD) were obtained for roughness comparison.

The surface morphology of membranes were observed via scanning electron microscopy (SEM) with a XL-30 ESEM-FEG and energy dispersive X-ray spectroscopy (EDX) was used to acquire bulk composition information of the membranes.

2.2.2.3 Hydrogen permeability measurement

Hydrogen permeability was used in custom-built cross-flow testing system based on the set up of V. Jayaraman et al(Jayaraman et al. 1995), shown in Figure 2.1. The

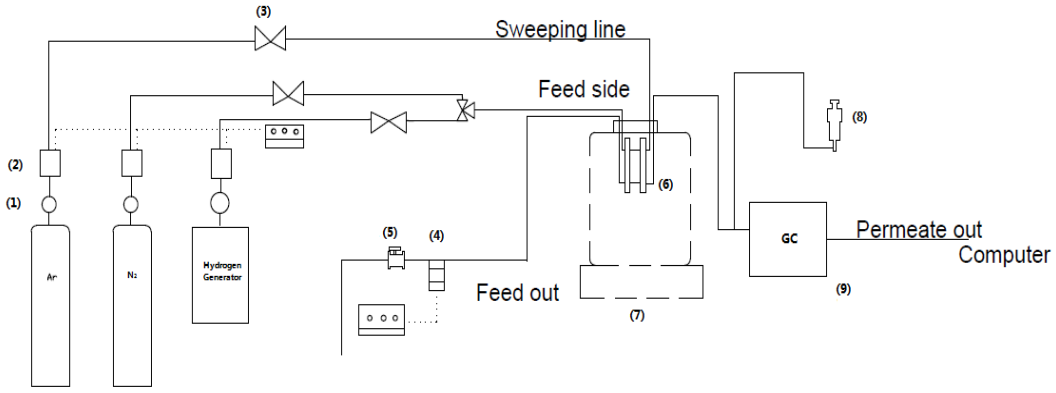

Figure 2.1 Schematic design of the system (1)regulator,(2)mass flow controller,(3)stop valves,(4)pressure sensor,(5) back pressure gauge,(6)permeation cell,(7)muffle furnace,(8)soap bubble flow meter,(9)gas chromatography

details of manufactures are provided in Appendix. The self-supporting membranes were sealed into a type 316 stainless steel module between two graphite gaskets. The sealing of the gaskets was tested with pressurized nitrogen before every permeation test. The

effective membrane permeation area was 1.53 cm^2. the module was placed inside a muffle furnace for heating to 400 °C with ramp rate of 4 °C /min. During the heating to operation temperature, a mixture of N_2/H_2 was flushed on the feed side and argon on permeate side. Mass flow controllers (MKS Instruments) controlled the flow rate of all gases. Nitrogen and argon were ultra-high purity grade (99.999%). A hydrogen generator (VWR International, Model H2PEM-100-L) provided H_2 with purity of 99.99%+. After reaching the desired temperature, the nitrogen feed purge was shut off and pressurized hydrogen was introduced using a back pressure regulator (PRAXAIR) and pressure sensor (OMEGA) to regulated the upper bound of the feed pressure to 200 kPa. A pressure gauge read the argon sweep of the permeate side, which had a total pressure of approximately 20 kPa to 40 kPa. An Agilent 7890 gas chromatograph (GC) measured the concentration of gases in the permeate stream. The GC was calibrated with a customized gas standard from Air Products (with error of ±2%). A soap bubble flow meter confirmed the permeate flow rate. The total testing duration was 24 hours. A detail illustration of the testing setup is below:

Step 1. Load the sample into the stainless steel module, and seal the membrane with torque wrench.

For $Pd_{77}Ag_{23}$ membranes, graphite gaskets were applied. The graphite gasket can be used at temperature lower than 500 °C without air introduced, otherwise they will be oxidized. Tighten the outer part of the modulus carefully. Use the method to tighten flanges which tighten the screws eccentrically.

Graphite gaskets is available.

Step 2. Use Para film to prevent dust go inside the module while put it into the furnace.

Step 3. Connect the four connections to the plastic tubing.

Be careful while tighten different materials of tubing, especially plastic and copper which are soft and susceptible to be over tighten. Follow the instruction of swagelock with the stainless steel tubing. A quarter less is recommended for plastic tubing.

Step 4. Flush the line with inert gas for 15-30 min.

Step 5. Setup the muffle furnace. Depends on the heat profile, trials are needed to optimized the heating program. Over heat needs to be taken into consideration.

Step 6. Set up the thermal couples which will give better indication of the temperature inside and outside the module.

Step 7. When the temperature is reached the desired testing temperature, turn on the hydrogen and close the N_2, let it flush ~ 2min. The hydrogen flow rate should be 2 times or more than the estimated flow rate. If the hydrogen flow is too small the static pressure will lead to hydrogen permeability order of magnitude lower than the actual permeability.

Step 8. Pressurize the feed side with back pressure regulator and pressure sensor. Do increase the pressure slowly if the membrane is self-supported.

Step 9. Setup the GC, the fastest GC run can be 2 min. Do calibrate the GC, especially the concentration range is changed, for example, from 1% to 20%. Use either standard which can be purchased from air product (expensive, hundreds of dollars) or use mass flow controllers. It is recommended to only use mass flow controllers when the hydrogen concentration is larger than 5% or more. When the concentration of hydrogen is lower than 1%, standards are highly recommended. The mass flow controllers are also needed to be calibrated with bulb soap meter. Calibration table needs to be updated after calibration.

Step 10. Use the GC's program to collect the concentration automatically. The results of each run needed to be collected manually. Have not found a way to output all the results in batches yet.

Step 11. After the run, shut off the hydrogen and introduce the nitrogen until room temperature.

Step 12. Clean the stainless steel module with ethanol and fine sand papers. Flush the lines with air.

The permeability was calculated according to Sieverts' law.

$$J = \overline{P}/t \cdot \left(P_H^{0.5} - P_L^{0.5}\right)$$

In the above equation, J [mol s^{-1} m^{-2}]is the flux of hydrogen, $\overline{P}$ [mol m^{-1} s^{-1} $Pa^{-0.5}$]is the permeability , t [m] is the thickness of the membrane; P_H [Pa] is hydrogen partial pressure of the feed side, and P_L [Pa] is hydrogen partial pressure of permeate side.

Detail calculations with measured parameters are shown below:
1 atm = 101.325 kPa = 0.1 MPa = 14.696psi

0.082 L atm / mol K

1 sccm= 4.1×10^{-5}mol/min=6.8×10^{-7}mol/s=$0.01667 \times 10^{-6}$$m^3$/s

$$J = \frac{\bar{P}}{t}\left(\sqrt{P_{H_2}} - \sqrt{P_0}\right)$$

$\overline{P}$ is permeability

J is flux

t is thickness

P_{H2} is hydrogen pressure on feed side

P_0 is hydrogen pressure on permeate side

$$\bar{P} = \frac{ac}{(100-c)A} t \frac{1}{\sqrt{P_{H_2}} - \sqrt{cP_0}}$$

Use P_0=0

$\bar{P}$: Permeability in mol/m s $Pa^{1/2}$

a: Flow rate of argon in sccm (standard cubic centimeter per minute)

c: Hydrogen composition detected by GC in %

A: Membrane permeation area in mm^2

t: Membrane thickness in mm

P_{H2}: Hydrogen pressure on feed side in kPa

After unit conversion

$$\bar{P} = \frac{ac}{(100-c)A} t \frac{1}{\sqrt{P_{H_2}} - \sqrt{cP_0}} \times 2.1503488 \times 10^{-5}$$

$$c = \frac{100}{1 + \frac{at \times 2.1503488 \times 10^{-5}}{\bar{P}A\ (\sqrt{P_{H_2}} - \sqrt{cP_0})}}$$

The stainless steel modules to seal the membranes are modified from Prof. Jerry Lin's lab. (1995) The design can be refereed to Appendix. Figure 2.2

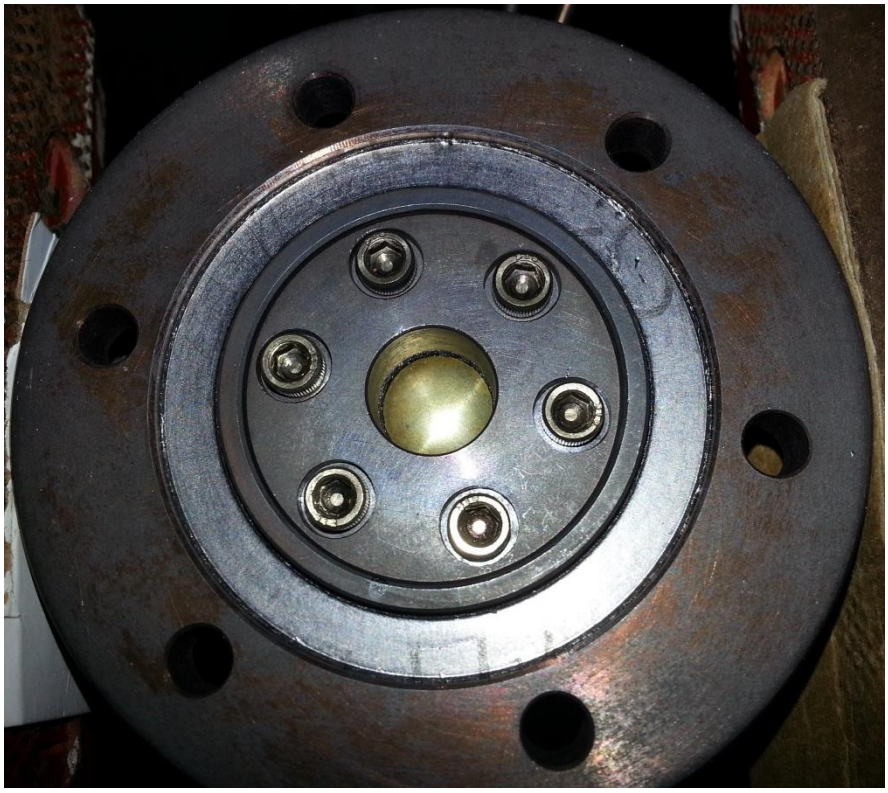

Figure 2.2 Stainless steel module to test the hydrogen permeability of the free standing metallic membranes. Here is a brass foil to test leak rate.

2.3 Results and discussions

2.3.1 Surface composition and elemental binding energy

Figure 2.3 presents a summary of the surface composition information measured by XPS after each type of heat treatment and after the hydrogen permeation tests. The Pd/(Pd+Ag) surface atomic ratio of as received samples (68/100) is lower than the nominal ratio (77/100) which may be a result of the intrinsic surface energy difference of two elements (Vitos et al. 1998). After the initial heat treatments, Samples B had a higher Pd/ (Pd+Ag) ratio than Samples A, while Samples C had a lower Pd/(Pd+Ag) ratio than Samples A. Samples D had a Pd/(Pd+Ag) ratio approximately equal to that of Samples A.

At the high vacuum level (~0.1 Pa) of Samples D, based on XPS results not included here for brevity, it was found that heat treatment at temperatures up to 800 °C resulted in insignificant change in the Pd/Ag surface ratio. At the lower vacuum level (10-20 kPa, local pressure is 101kPa) of Samples C, the Ag measurably segregates to the surface after 24 hours of annealing at 400°C. After air exposure, Pd-based membranes can form a surface layer of hydrocarbon up to 10 nm (Antler 1982). For Samples C, the residual oxygen present in the vacuum oven cleaned the surface and eliminated the barrier to surface diffusion. As seen in Figure 2.4 (d), Samples C have the lowest carbon level. The lower surface energy of Ag leads to Ag surface segregation of Samples C. Although Pd has lower vapor pressure than Ag (Alcock et al. 1984), the evaporation of both elements is not the major factor in changing the surface composition at temperatures as low as 400°C (the vapor pressures of solid Pd as $2.8x10^{-18}$ Pa and solid Ag as $4.2x10^{-11}$ Pa were calculated at 400°Cfrom Alcock et al.(Alcock et al. 1984)). Two possible explanations were hypothesized for the unchanged surface composition of Samples D (annealed at a lower pressure level / higher vacuum level than Samples C). First, taking into consideration that the case where the evaporation of both elements does not have significant impact on the surface composition; it is possible that at the high vacuum level of Samples D (~0.1 Pa) surface CH_x prohibited the diffusion of atoms. The presence of co-adsorbates can markedly influence surface diffusion, as carbon is known to considerably decrease the self-surface diffusion rate of copper(Somorjai 1994). Second, the case where the rate of evaporation between the two elements impacts surface composition – Ag evaporates faster than Pd because it has a higher vapor pressure. However, because of the lower Ag surface energy, the Ag tends to segregate on the

surface – which may compensate for the small loss of Ag because of evaporation. It is important to note that Samples D were sealed in a quartz tube, a closed system; therefor

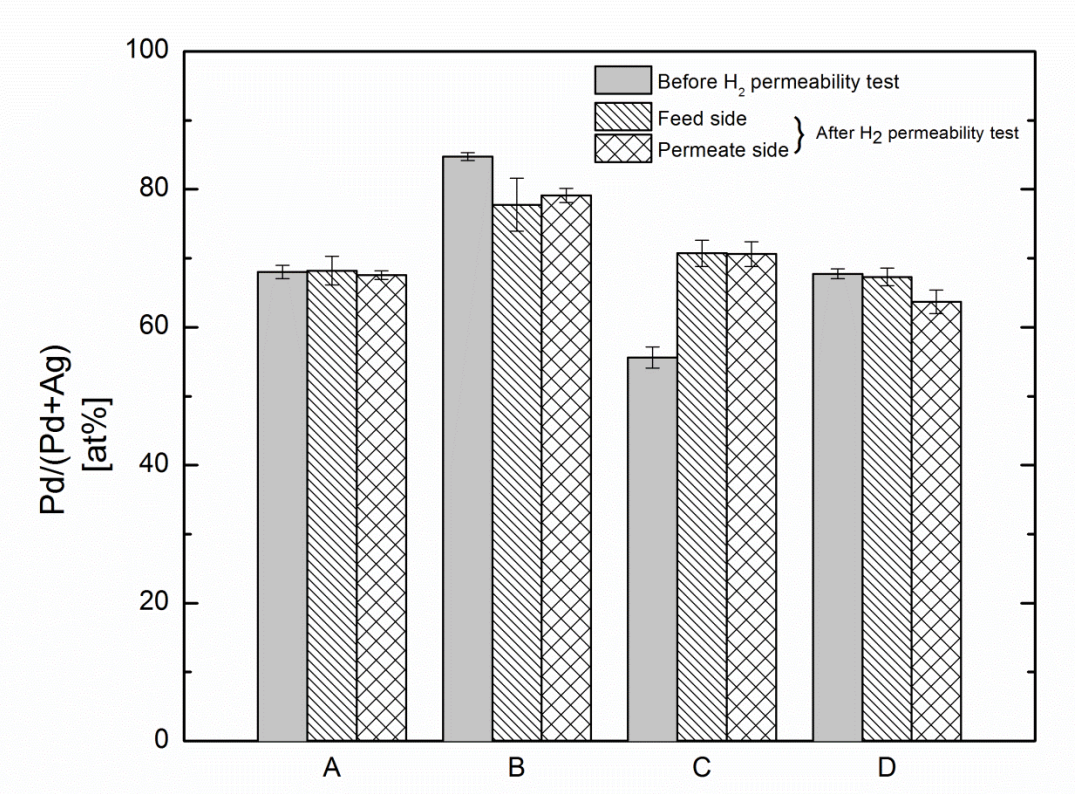

Figure 2.3 Surface Pd/(Pd+Ag) at% of all treatment samples before and after hydrogen permeability tests. Pd/(Pd+Ag) at% is calculated from high resolution XPS spectra.

the vapor pressure would reach an equilibrium state and further evaporation, beyond initial loss, would be limited. The vacuum level is believed to be crucial to promote Ag segregation.

Regardless of the initial treatment, the feed and permeate sides of a certain sample type have similar surface compositions after the hydrogen permeation test. For Samples A (the as-received samples), there was no significant change in Pd/(Pd+Ag) surface ratio compared to before the hydrogen permeation test. The results contradict the results of other studies（Wise et al. 1975; Alashab and Harris 1988; Tucho et al. 2009a; Tucho et al.

2009b）in which the Pd-Ag membranes show Ag segregation after hydrogen permeation tests. The difference between these results and others' published results is possibly because of the difference between permeation test conditions of this study and others' conditions. In samples of this study, both feed and permeate sides showed Ag segregation afterwards. Samples D (800 °C, high vacuum, water quenched) showed a similar trend to Samples A; in these only the permeate side exhibited slight Ag segregation. Samples B (air-treated) and Samples C (vacuum oven annealed) displayed the opposite trend with each other. Compared to samples within a treatment grou before the hydrogen permeation test, Samples B had a lower Pd/Ag ratio, while samples C had a higher ratio. For Samples B (air-treated samples), compared to as-received composition Samples A (the as-received membranes), Pd segregation still existed. A. Ramachandran et al. (Tucho et al. 2009b) found similar results to us. Reverse segregation (e.g. Pd segregation to the surface) occurred in Samples C. Other studies also have shown that hydrogen adsorption can cause reverse segregation (Pd segregation to the surface) (Ramachandran et al. 2010; Zhang et al. 2012a).

Table 2.2 and Figure 2.4 summarize XPS results of the samples. Table 2.2 Binding energy of Pd $3d5_{/2}$ and Ag $3d5_{/2}$ after heat treatment and after hydrogen permeation test presents the Pd $3d_{5/2}$ and Ag $3d_{5/2}$ core level binding energy (BE) of samples both after initial heat treatment and after hydrogen permeation testing. Figure 2.4 shows the XPS high resolution scans of Pd $3d_{5/2}$, Ag $3d_{5/2}$, O 1s/Pd 3p and C 1s of all samples after initial heat treatment before permeation testing. In Samples A (the as-received samples), the Pd $3d_{5/2}$ BE has two components in the position of 334.8 eV and 335.5 eV. The higher binding energy component was attributed to PdO_x ($0<x<1$) (Yang

et al. 2005). In Samples A, Ag $3d_{5/2}$ has BE of 367.5 eV which agrees with the literature（Mardilovich et al. 1998; Mejdell et al. 2008; Mejdell et al. 2010）. In Samples C and Samples D (after vacuum annealing) the Ag $3d_{5/2}$ BE position is unchanged, but the higher BE of the Pd $3d_{5/2}$ components shifted to lower binding energy of 335.1 eV. This downshift in the high BE component of the Pd $3d_{5/2}$ may be the result of a change in chemical states caused by Ag accumulation on the surface and the decomposition of PdO_x(Gabasch et al. 2006). All samples have the same binding energy of Ag $3d_{5/2}$ and Pd $3d_{5/2}$ after hydrogen permeation tests. There is no oxidized state peak present after permeation tests. The 2-3 nm PdO_x layer on the surface formed after air heat treatment has been reduced during permeability test (Ramachandran et al. 2010).

Table 2.2 Binding energy of Pd $3d_{5/2}$ and Ag $3d_{5/2}$ after heat treatment and after hydrogen permeation test

Sample	Binding energy (eV)			
	After heat treatment		After hydrogen permeation test	
	Pd $3d_{5/2}$	Ag $3d_{5/2}$	Pd $3d_{5/2}$	Ag $3d_{5/2}$
A	334.8/335.4	367.5	334.8/335.3	367.5
B	336.9	367.9	334.8/335.3	367.5
C	334.8/335.1	367.5	334.8/335.3	367.5
D	334.8/335.1	367.5	334.8/335.3	367.5

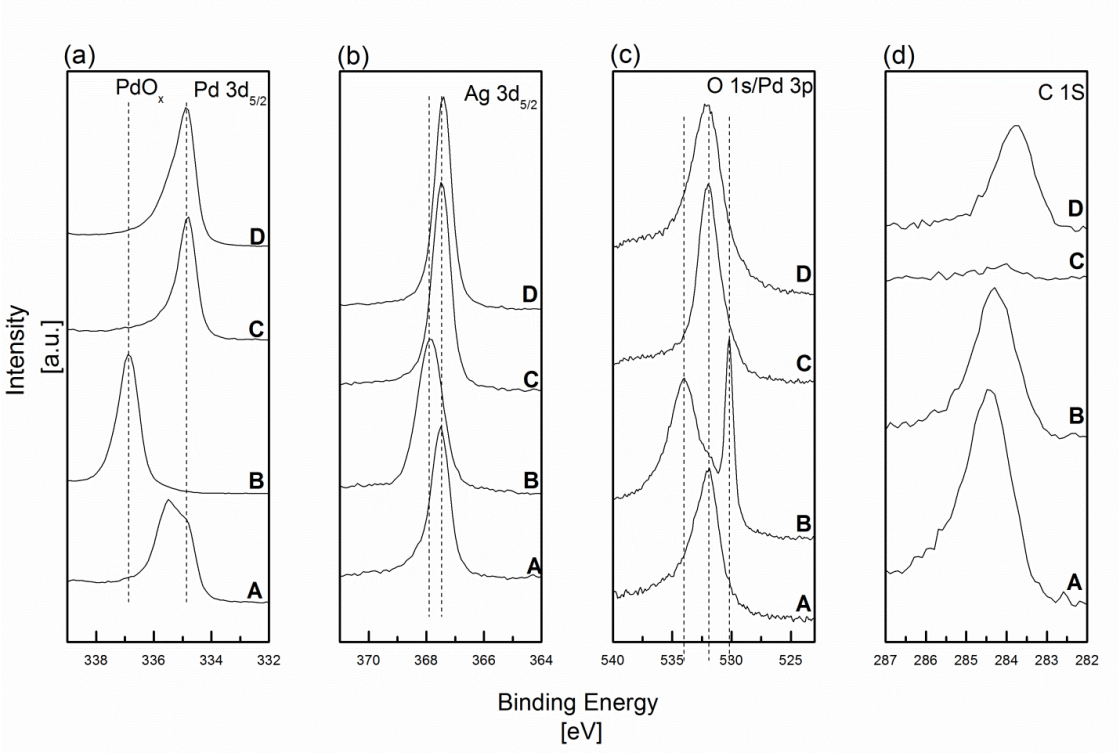

Figure 2.4 High resolution XPS scanning of Pd $3d_{5/2}$, Ag $3d_{5/2}$, O 1s/Pd 3p and C 1S for all treatment groups after heat treatment and before the permeation test.

Figure 2.4(a) and Figure 2.5 (a) show that after air treatment Samples B have a different BE peak centered at 336.9 eV, indicating oxidation of Pd; the BE of this oxidized state is comparable to that published by Wise et al. and Ward et al.（Wise et al. 1975; Ward and Dao 1999）. The metal component of Pd has the BE of 334.8 eV. Also, after long exposure to air, Figure 2.4(b) and Figure 2.5(b) show that for Samples B that the Ag $3d_{5/2}$ BE has a +0.4 eV shift. To investigate the oxidation process of Pd, experiments with different duration of annealing in air (samples B.1 and B.2) were performed. As seen in Figure 2.5, unlike the Pd $3d_{5/2}$ peak, the Ag $3d_{5/2}$ only displays a single peak during different air treatment of duration. The enthalpy of formation of Pd oxides and Ag oxides at 673 K are -118.6 kJ mol^{-1} (Warner 1967) and -29.4 kJ mol^{-1}

(Assal et al. 1997). Apparently, Pd is easier to be oxidized than Ag. But the difference between the enthalpy of formation of oxides cannot rule out the possibility of Ag oxides formation. However, it is believed that Ag was not oxidized according to the XPS results. For Ag, the oxidized state usually lowers BE of Ag core level（Weaver and Hoflund 1994; Bielmann et al. 2002）, while in these result, the core level shifts to a higher BE. Also, no O 1s component can be attributed to Ag oxide. The shift of Ag $3d_{5/2}$ may be the result of two factors: the formation of PdO_x on surface and the change of Pd/Ag ratio. Tarditi et al. found that differences in the Pd/Ag ratio of the surface could cause Ag binding energy shift (Tarditi et al. 2012). These two factors are probably interrelated; and a change in either of them changes the chemical state of Ag. Yang et al., however, observed no Ag core level change after air oxidation (Yang et al. 2005). They treated the samples in air for 1 hour compared to 24 hours in this study. Their Pd high resolution XPS spectra showed that the majority of Pd was not in oxidized states (Yang et al. 2005). In this case, the XPS spectra after 24 hours air treatment showed the presence of only oxidized Pd. The difference in heat treatment duration may account for the disagreement between results in this study and others' results.

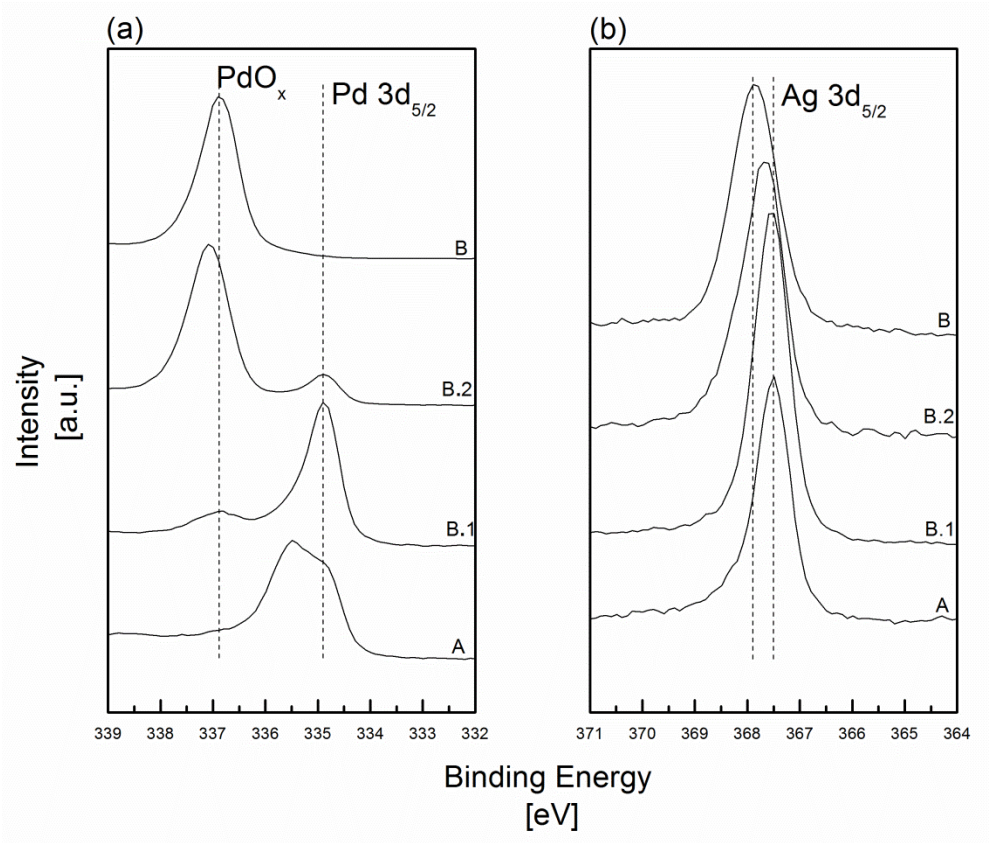

Figure 2.5 Pd $3d_{5/2}$ and Ag $3d_{5/2}$ high resolution XPS plots after different air treatment duration. Sample A is as-received sample, Sample D is air-treated at 400℃ for 24 hrs.

2.3.2 Surface roughness and morphology

Table 2.3 summarizes the roughness (RMS) and surface area difference (SAD) measured by AFM. Figure 2.6 shows the AFM Images of samples after each heat treatment. Surface roughness of the membranes changed after both heat treatment and hydrogen permeation tests. The images in Figure 2.6 are 2 μm x 2 μm with first order flattening applied. After the initial heat treatments Samples B, which were air treated, have the maximum roughness of 53 ± 6.3 nm and Samples A, which are the as-received samples, have the minimum roughness of 3.4 ± 1.4 nm. After hydrogen permeation tests, the feed sides of all sample groups had smaller roughness than the permeate sides of

samples within the same treatment group. For example, the feed side of Samples B had a roughness of 14.7 ± 5.6 nm compared to 45.3 ± 0.7 nm on the permeate side.

Table 2.3 Roughness and surface area difference after heat treatment and permeation test

Sample	Roughness (nm)			Surface area difference (%)		
	After treatment	After Hydrogen Permeation Test		After treatment	After Hydrogen Permeation Test	
		Feed	Permeate		Feed	Permeate
A	3.4±1.4	6.8±2.0	8.0±2.3	0.3±0.2	3.4±0.2	2.5±1.6
B	53.0±6.3	14.7±5.6	45.3±0.7	31.7±2.5	3.4±1.4	13.6±5.6
C	11.8±4.8	5.4±1.6	11.9±5.9	2.1±1.8	1.2±0.7	4.1±1.7
D	13.6±7.6	7.8±1.1	8.0±1.6	2.2±1.0	1.7±0.5	2.3±0.8

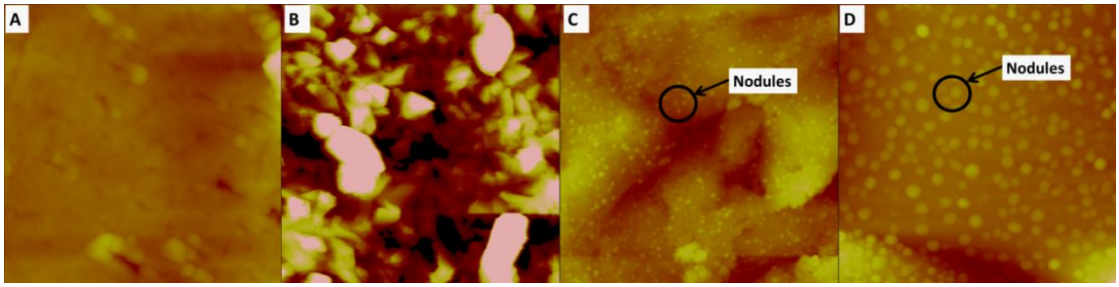

Figure 2.6 AFM height images of all treatment groups. Treatment details refer to Table 2.1. Image size is 2 µm x 2 µm with first order flattening. 50 µm height scale from dark to bright.

Figure 2.7 presents SEM images of the surfaces of the samples after each heat treatment. At a magnification of 250 X, Samples C maintained features similar to the as-received samples (Samples A). At higher magnification of 15 KX, Samples C showed more features. The roughness data presented in Table 2.2. also shows that Samples Cs are rougher than Samples A. From the AFM images of Figure 2.6, the black dots visible in the SEM images of Samples C were identified (2.5c.1) as nodules on the membrane surface. Samples D (2.5 d.1) have nodules that are larger than those found on Samples C. Another feature visible in the SEM images on surface of Samples D (Figure 2.7 d) is

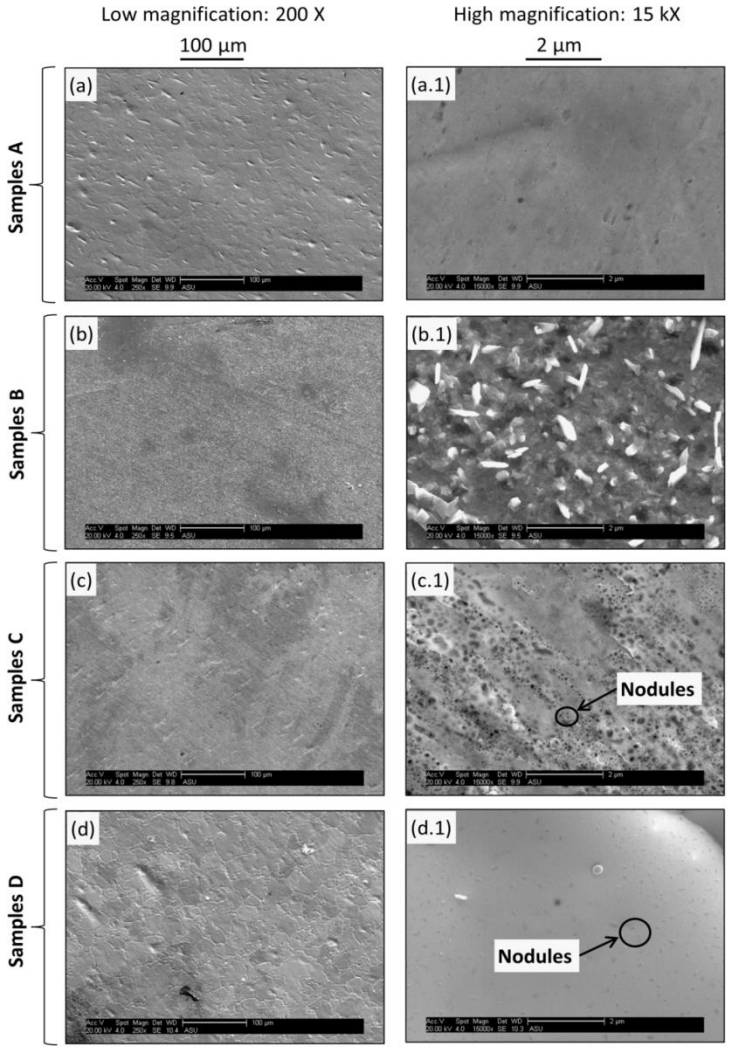

Figure 2.7 SEM images of all treatment groups at two scales. After 800 ℃ vacuum annealing (Sample D) grain boundaries are exposed.

grain boundaries. Tucho et al. and Uemiya established that the initiation of grain coarsening for Pd/Ag membranes occurs between 400°C-500°C（Uemiya 1999; Tucho et al. 2009b）, so the heat treatment of Samples D at 800°C was sufficient to activate coarsening.

As indicated in the AFM measurements and SEM images, nodules developed after vacuum annealing in both Samples C and Samples D. Other studies have also

observed nodule formation in Pd-based membranes after permeation test of air treated samples. These previous researchers hypothesized that the nodules result from the volume change accompanying the formation of palladium oxides. They also theorized that a smaller grain size with more grain boundaries would promote nodule formation.

However, it is hypothesize that the nodule formation is not the result of the formation of palladium oxides. The XPS data, presented in Table 2.2 and Figure 2.4, shows no chemical shift of the Pd $3d_{5/2}$ peak of Samples C and no traces of oxidation were observed. For Samples D, which were annealed under vacuum at 800°C, the vacuum level was ~0.1 Pa (~1 ppm O_2); therefore oxidation cannot explain the nodule formation. In Figure 2.6, the AFM images show that the large grain size of Samples D have nodule sizes larger (~100 nm) than those on Samples C (~40 nm), which is contrary to what was claimed by Tucho et al. and Aggarwal(Aggarwal et al. 2000; Tucho et al. 2009b). One possible explanation is that the nodules are fully coherent precipitates as a second phase(Porter 2009). The calculated phase diagram of Pd-Ag shows a miscibility gap at temperatures lower than 392 °C - so precipitation of a second phase is possible. Another possible explanation is that the high annealing temperature helped any bulk impurities (if present) diffuse to the surface of the membrane (Musket 1976; Yoshida et al. 1983). Existing surface impurities may contribute to nodule formation. After hydrogen permeation tests, part of the permeate sides of Samples C and Samples D retained nodules with sizes of approximately 100 nm.

2.3.3 Hydrogen permeability test

Each treatment group has at least 2 samples. The testing condition for each sample is consistent. The concentration was collected during a 24 hour period after the desired temperature was reached in the muffle furnace.

Table 2.4 Permeability raw data of a Sample A (as-received $Pd_{77}Ag_{23}$ membrane)

Time (hr)	GC data (ppm)	Permeability (mol m^{-1} s^{-1} $Pa^{-0.5}$)
2	8.70E+04	3.08E-09
3	1.22E+05	4.77E-09
4	1.59E+05	6.90E-09
5	1.90E+05	8.97E-09
6	1.97E+05	9.49E-09
7	2.01E+05	9.78E-09
8	2.06E+05	1.02E-08
9	2.09E+05	1.04E-08
10	2.10E+05	1.05E-08
11	2.13E+05	1.07E-08
12	2.15E+05	1.09E-08
13	2.17E+05	1.10E-08
14	2.19E+05	1.12E-08
15	2.19E+05	1.12E-08
16	2.22E+05	1.14E-08
17	2.22E+05	1.14E-08
18	2.25E+05	1.17E-08
19	2.26E+05	1.18E-08
20	2.28E+05	1.19E-08
21	2.29E+05	1.20E-08
22	2.30E+05	1.21E-08
23	2.31E+05	1.22E-08
24	2.32E+05	1.23E-08

Table 2.4 is one piece of the as-received $Pd_{77}Ag_{23}$ membranes. The hydrogen permeability is calculated as the average of hydrogen permeability of the 6^{th} hour to the 24^{th} hour. Because before the 6^{th} hour the flux increased drastically, while after the 6^{th} hour the hydrogen permeability has a slight increase over time. This may be due to the

activation effect of the catalytic effect of the Pd. Most precious metal catalysis needs to be activated before it can gets its full power. Also, the GC equipment may bring up error which will be taken into consideration later. So for this piece the hydrogen permeability is $1.12x10^{-8}$ mol m^{-1} s^{-1} $Pa^{-0.5}$ at 673 K with upper hydrogen pressure (feed side) of 200 kPa and lower hydrogen partial pressure (permeate side) of 140 kPa multiplied by the concentration detected by the GC. The Ar flow rate was 96 sccm. Table 2.5 shows permeability raw data of a Sample B. The analysis for this data set is the same with that of Table 2.4. So the permeability is 1.16 $x10^{-8}$ mol m^{-1} s^{-1} $Pa^{-0.5}$ at the same condition with that of Sample A. Table 2.6 is the permeability raw data of a sample C with Ar flow of 94.4 sccm, permeate side hydrogen partial pressure is 114 kPa multiplied by the concentration detected by the GC. Table 2.7 is the permeability raw data of a sample D (24 hr in vacuum sealed quartz tube) with Ar flow rate 97.45, feed H_2 pressure of 216 kPa, permeate H_2 partial pressure is 120 kPa multiplied by the concentration of H_2 collected by GC. Table 2.8 is the permeability raw data of a sample E (a second run of Sample B). All the other raw data is listed in appendix.

Table 2.5 Permeability raw data of a Sample B ($Pd_{77}Ag_{23}$ after 24 hours air treatment)

Time (hr)	GC data (ppm)	Permeability (mol m^{-1} s^{-1} $Pa^{-0.5}$)
0	1.20E+05	4.68E-09
1	1.44E+05	6.00E-09
2	1.68E+05	7.49E-09
3	1.84E+05	8.57E-09
4	1.95E+05	9.36E-09
5	2.01E+05	9.81E-09
6	2.05E+05	1.01E-08
7	2.05E+05	1.01E-08
8	2.12E+05	1.07E-08
9	2.14E+05	1.08E-08
10	2.17E+05	1.11E-08
11	2.18E+05	1.11E-08
12	2.20E+05	1.13E-08

Table 2.5 Continued

Time (hr)	GC data (ppm)	Permeability (mol m^{-1} s^{-1} $Pa^{-0.5}$)
13	2.21E+05	1.14E-08
14	2.23E+05	1.16E-08
15	2.24E+05	1.16E-08
16	2.26E+05	1.18E-08
17	2.29E+05	1.21E-08
18	2.30E+05	1.22E-08
19	2.32E+05	1.23E-08
20	2.33E+05	1.24E-08
21	2.34E+05	1.25E-08
22	2.34E+05	1.25E-08
23	2.35E+05	1.26E-08

Table 2.6 Permeability raw data of a sample C ($Pd_{77}Ag_{23}$ after 24 hours vacuum annealing)

Time (hr)	GC data (ppm)	Permeability (mol m^{-1} s^{-1} $Pa^{-0.5}$)
0.0	1.35E+05	5.17E-09
0.4	1.56E+05	6.30E-09
0.8	1.63E+05	6.70E-09
1.3	1.64E+05	6.76E-09
1.7	1.64E+05	6.76E-09
2.1	1.63E+05	6.70E-09
2.5	1.62E+05	6.64E-09
2.9	1.61E+05	6.58E-09
3.3	1.61E+05	6.58E-09
3.8	1.61E+05	6.58E-09
4.2	1.62E+05	6.64E-09
4.6	1.61E+05	6.58E-09
5.0	1.61E+05	6.58E-09
5.4	1.61E+05	6.58E-09
5.8	1.61E+05	6.58E-09
6.3	1.62E+05	6.64E-09
6.7	1.62E+05	6.64E-09
7.1	1.62E+05	6.64E-09
7.5	1.62E+05	6.64E-09
7.9	1.63E+05	6.70E-09
8.3	1.63E+05	6.70E-09
8.8	1.63E+05	6.70E-09
9.2	1.64E+05	6.76E-09
9.6	1.64E+05	6.76E-09
10.0	1.68E+05	6.99E-09

Table 2.6 Continued

Time (hr)	GC data (ppm)	Permeability (mol m^{-1} s^{-1} $Pa^{-0.5}$)
10.4	1.68E+05	6.99E-09
10.8	1.69E+05	7.05E-09
11.3	1.68E+05	6.99E-09
11.7	1.69E+05	7.05E-09
12.1	1.69E+05	7.05E-09
12.5	1.71E+05	7.17E-09
13.5	1.71E+05	7.17E-09
14.5	1.72E+05	7.23E-09
15.5	1.73E+05	7.29E-09
16.5	1.73E+05	7.29E-09
17.5	1.74E+05	7.35E-09
18.5	1.74E+05	7.35E-09
19.5	1.75E+05	7.41E-09
20.5	1.76E+05	7.47E-09
21.5	1.76E+05	7.47E-09
22.5	1.76E+05	7.47E-09
23.5	1.76E+05	7.47E-09
24.5	1.78E+05	7.60E-09

Table 2.7 Permeability raw data of a sample D (24 hr in vacuum sealed quartz tube)

Time (hr)	GC data (ppm)	Permeability (mol m^{-1} s^{-1} $Pa^{-0.5}$)
0	7.40E+04	2.40E-09
1	1.01E+05	3.52E-09
2	1.44E+05	5.60E-09
3	1.78E+05	7.54E-09
4	1.95E+05	8.62E-09
6	2.09E+05	9.57E-09
8	2.16E+05	1.01E-08
10	2.22E+05	1.05E-08
12	2.26E+05	1.08E-08
14	2.30E+05	1.11E-08
16	2.33E+05	1.13E-08
18	2.35E+05	1.15E-08
20	2.36E+05	1.16E-08
22	2.38E+05	1.17E-08
23.5	2.38E+05	1.17E-08

Table 2.8 Permeability raw data of a sample E (sedond run of Sample B)

Time (hr)	GC data (ppm)	Permeability (mol m^{-1} s^{-1} $Pa^{-0.5}$)
0.4	8.30E+04	2.89E-09
1.4	1.20E+05	4.63E-09
2.4	1.40E+05	5.70E-09
3.4	1.60E+05	6.87E-09
4.4	1.75E+05	7.81E-09
5.4	1.86E+05	8.54E-09
6.4	1.93E+05	9.03E-09
7.4	1.98E+05	9.38E-09
9.4	2.04E+05	9.82E-09
11.4	2.09E+05	1.02E-08
13.4	2.12E+05	1.04E-08
15.4	2.14E+05	1.06E-08
17.4	2.18E+05	1.09E-08
19.4	2.22E+05	1.12E-08
21.4	2.23E+05	1.13E-08
21.9	2.23E+05	1.13E-08
22.9	2.24E+05	1.14E-08

Table 2.9 Hydrogen permeability as the function of the surface composition after heat treatment

Sample	Pd/(Pd+Ag) (%)	Error	Permeability (mol m^{-1} s^{-1} $Pa^{-0.5}$)	Error
A	68.03	0.97	1.02	0.20
B	84.74	0.58	1.28	0.26
C	55.62	1.56	0.36	0.36
D	67.76	0.72	1.15	0.08
E	77.76	3.85	1.11	0.03

Hydrogen permeability tests after the initial heat treatments were performed. Samples B had the local maximum hydrogen permeability and Samples C has the local minimum hydrogen permeability. Samples D had permeability close to the as-received samples. After hydrogen permeability tests of Samples B (the air treated samples), XPS measurements showed Pd enrichment on surface （Figure 2.3). A second hydrogen

permeability test on these samples were performed (Samples E in Table 1) to see if the enriched Pd/Ag surface ratio still has influence on the permeability. Figure 2.8 plots the hydrogen permeability of all samples as a function of surface palladium ratio measured by XPS after heat treatment and before the hydrogen permeability test. Table 2.9 lists the actual data of 2.8. As seen in Figure 2.8, several phenomena can be observed. Sample A and Sample D share similar surface composition as well as hydrogen permeability within the error. The hydrogen permeability of samples after high vacuum and high temperature heat treatment (Sample D) is only slightly higher than the as-received sample (Sample A). The major change of the Sample D is the grain size according to the SEM images. The increase of grain size of Sample D leads to grain boundaries decrease. It is hypothesized that while the possible contaminates migrate to the grain boundaries, contaminants were collected by the grain boundaries which exposed more catalytic sites. However, the hydrogen may diffuse through the grain boundaries; the decrease of grain boundaries may block part of the diffusion path. These two factors may co-exist and result in the little change in hydrogen permeability. After air treatment (Sample B) there is significant increase in hydrogen permeability. The majority of the surface was covered by Pd_xO, the subsequent reduction process during the hydrogen permeability test may result in the relatively large error in hydrogen permeability. The air treatment brings about large surface roughness change which also contribute to the difference of different samples tested. Interestingly, after the first run of air treatment sample (Sample B), before the second run was performed, the surface composition has deviated from different samples (Sample E) this validated the hypothesis that the reduction process is different for different samples, thus the hydrogen permeability is different. Still the relatively high

Pd/(Pd+Ag) is remained after the testing of Sample B and Sample E still has higher hydrogen permeability than Sample A. Though not verified, it is possible that the Sample E after hydrogen permeability test have very uniform Pd/(Pd+Ag) surface compositions. For Sample C, according to the XPS result, the surface composition recovered after hydrogen permeability test. Reverse segregation ie, Pd segregation happened during the test of Sample C. Similar to the process of reduction of Sample B, this process involved complex segregation behavior during which the hydrogen permeability shows a large deviation from different samples. A second run of sample C may show comparable hydrogen permeability of Sample A and Sample D according to the XPS results.

When using Sieverts law for hydrogen permeability calculation, it is usually assumed that the transport process is diffusion-controlled. If the surface transport process is also involved the index would be larger than 0.5. However the trend which states the hydrogen permeability is higher when the surface Pd/(Pd+Ag) ratio is high still exist even when the index is 1. So it is possible that bulk diffusion and surface transport has comparable contribution to the hydrogen permeability. It is important to note that the heat treatment only modified the surface composition of the membranes, not the bulk composition. EDX measurements indicated no change in the bulk membrane composition after each heat treatment; EDX has a deeper penetration depth into a sample than XPS and, therefore, does not measure surface compositional changes (Turner et al. 2003). The X-ray diffraction pattern of Samples B (not shown for brevity) indicates that both PdO_x and Pd/Ag phases exist. That indicates that the oxidation developed within the penetration depth and detection limits of XRD (the calculated penetration depth for

$Pd_{77}Ag_{23}$ is about 3.7 μm - calculated with the data from(Henke et al. 1993)). Therefore, the bulk diffusion rate should not differ after heat treatment.

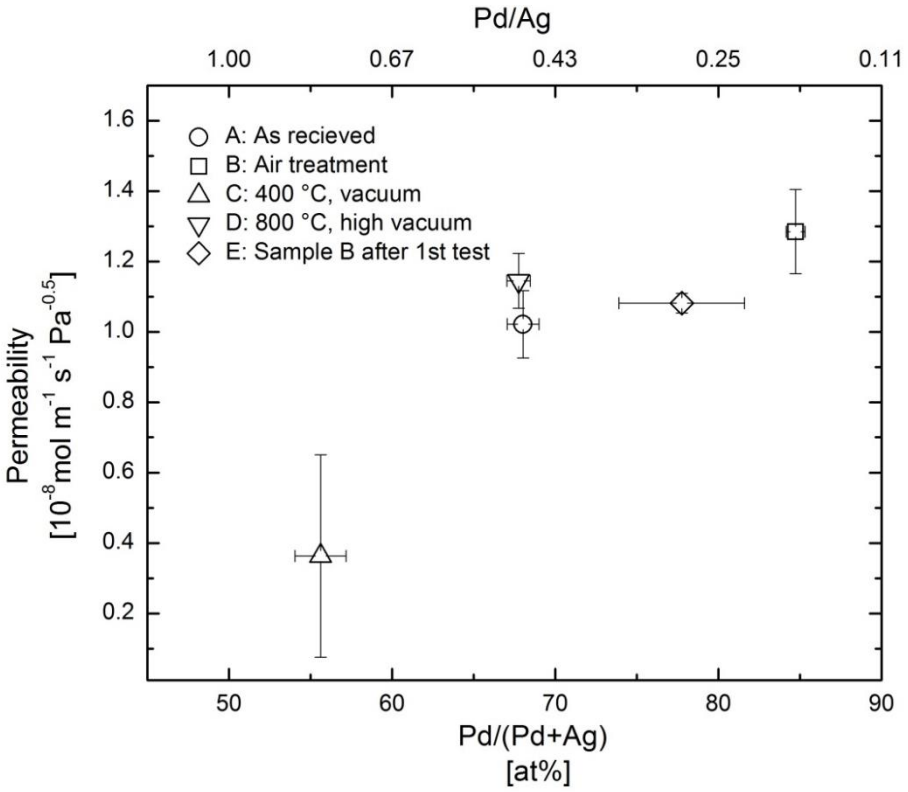

Figure 2.8 Surface Pd/(Pd+Ag) after heat treatment and before the hydrogen permeability test vs hydrogen permeability

After the heat treatments, both the higher concentration of palladium at the membrane surface and the increased surface area provides more catalytic sites for hydrogen dissociation/association. These two features helped increase the surface reaction rate. However, Samples C have larger roughnesses but lower hydrogen permeability than Samples A. Surface area difference cannot explain the trend of hydrogen permeability for Samples A and Samples C. Samples D have the same Pd/Ag surface ratio as Samples A, but higher hydrogen permeability. The higher roughness of Samples D may account for the permeability difference. When comparing high resolution

carbon peaks in Figure 2.4 d, Samples C had the lowest intensity and also had the minimum hydrogen permeability. The other three sample types shared a comparable level of carbon intensity. High resolution scans of S and Cl (not shown for brevity) of all sample types were also obtained. All sample types had the comparable intensity of surface S and Cl. Based on the discussion above, decarbonization and contamination removal do not cause the higher observed permeability of Samples B.

Ward reported that for a 25 μm thick PdAg membrane that the permeability at 400°C should be diffusion-controlled (Ward and Dao 1999). In this study, it has been shown that the membrane permeability varied as a result of heat treatment that only modified the surface composition. Ramachandran et al. showed that inert gas treatment suppressed permeability (Ramachandran et al. 2010). The surface composition may be a possible explanation to what Ramachandran et al. (Ramachandran et al. 2010) found.

2.4 Conclusions

Surface Pd/Ag segregation promoted by heat treatment has an impact on hydrogen permeability of $Pd_{77}Ag_{23}$ membranes. Three surface Pd/Ag ratios were achieved by heat treatment under different conditions. Roughness information shows the surface area is not the major factor resulting in permeability changes. XPS results of C, Cl and S eliminate the effect of decarbonization and impurity removal as a factor resulting in permeability changes. Previously, there has been little research emphasis on the segregation behavior of Pd-based membranes. For the first time, this research reports a relationship between surface segregation behavior and hydrogen permeability. Surface segregation plays an important factor in hydrogen permeability. In-situ tracking of the

surface segregation and surface area changes may better help establish these relationships according to this research.

CHAPTER 3 HYDROGEN PERMEABILITY OF CU-ZR AMORPHOUS METALLIC MEMBRANES AND STABILITY

3.1 Introduction

The Cu-Zr binary amorphous alloy system has drawn interest because of its good mechanical properties and low cost.（Lind et al. 2006; Ge et al. 2008）Xu et al. and Zhang et al. found a series of Cu-Zr binary compositions that are bulk metallic glass formers.(Xu et al. 2004a; Zhang et al. 2009) Calculation of the Time-Transformation-Temperature (TTT) curve is a method to predict the GFA of amorphous alloys (Ge et al. 2008) Ge et al. used the CALPHAD method to estimate TTT curves of Cu-Zr alloys.(Ge et al. 2008) They found that the critical cooling rate to form amorphous alloys within the Cu-Zr system is between 4.32×10^2 - 2.63×10^4 K/S. They calculated that the T_g of Cu-Zr alloys ranges from 620 K to 750 K.(Ge et al. 2008) This makes Cu-Zr alloys suitable for hydrogen separation at operation temperatures near 573 K. The specific composition $Zr_{54}Cu_{46}$ has critical casting thicknesses up to 2mm (T_g: 696 K, T_x: 746 K).(Xu et al. 2004a) Hao et al. used first principles density functional theory to calculate the hydrogen permeability of a series of binary amorphous metals.(Hao and Sholl 2011b) Their results predicted that $Zr_{54}Cu_{46}$ could have hydrogen permeability comparable to pure Pd at 600 K.(Hao and Sholl 2011b)

Thermal stability is an important parameter in membrane performance. A significant limitation to potential use of amorphous metallic membranes for high-temperature hydrogen separations is related to their metastability. Because these materials are thermodynamically metastable, they possess a super cooled liquid region

(SCLR) which is bound by the glass transition (T_g) (on the low end) and crystallization temperatures (T_x) (on the high end).(Park et al. 2010) It is well established that holding an amorphous metal at the T_g or at temperatures within the SCLR for long times results in crystallization.(Yamaura et al. 2006) For membrane separation applications, the hydrogen permeability is known to decrease after crystallization of the amorphous metal.(Park et al. 2011) Therefore, it is preferable to use amorphous metals with a T_g that is higher than the temperature at which the process is being performed, in order to maintain the amorphous structure. Additionally, the presence of hydrogen can impact the thermal stability of amorphous metals by promoting crystallization.(Eliaz and Eliezer 1999) Dini et al. found that electrolytically hydrogenated amorphous Cu-Zr alloys have lower T_x than as-cast amorphous Cu-Zr alloys.(Dini and Dunlap 1985)

In this chapter, the experimental hydrogen permeability of Cu-Zr amorphous free-standing membranes were measured. Alloys with three different Zr concentrations were investigated. The experimentally measured hydrogen permeabilities deviated from the result calculated by Hao et al. (Hao and Sholl 2011b). It was hypothesized that surface oxides created resistance for hydrogen transport into the bulk material. That hydrogen permeability decreased after 1-2 hours during the permeability test. It was hypothesized that this is the result of hydrogen induced crystallization. The importance of thermal stability under hydrogen exposure was also discussed. These results point to the importance of the thermal properties and thermal stability of amorphous alloys relative to the hydrogen permeation testing temperature.

3.2 Experimental

3.2.1 Materials

Raw metals (Cu and Zr) from Alfa-Aesar with purity of 99.999% were purchased. The raw metals were cleaned with ultrasonication in acetone and then in ethanol before the raw metals were weighed and arc melted (Edmund Buehler, model AM) in an argon atmosphere into 15 g buttons. Three compositions were chose with atomic percentages of Zr of 37, 54 and 60. During the arc-melting process, the buttons were flipped twice to ensure complete alloying of the metals.

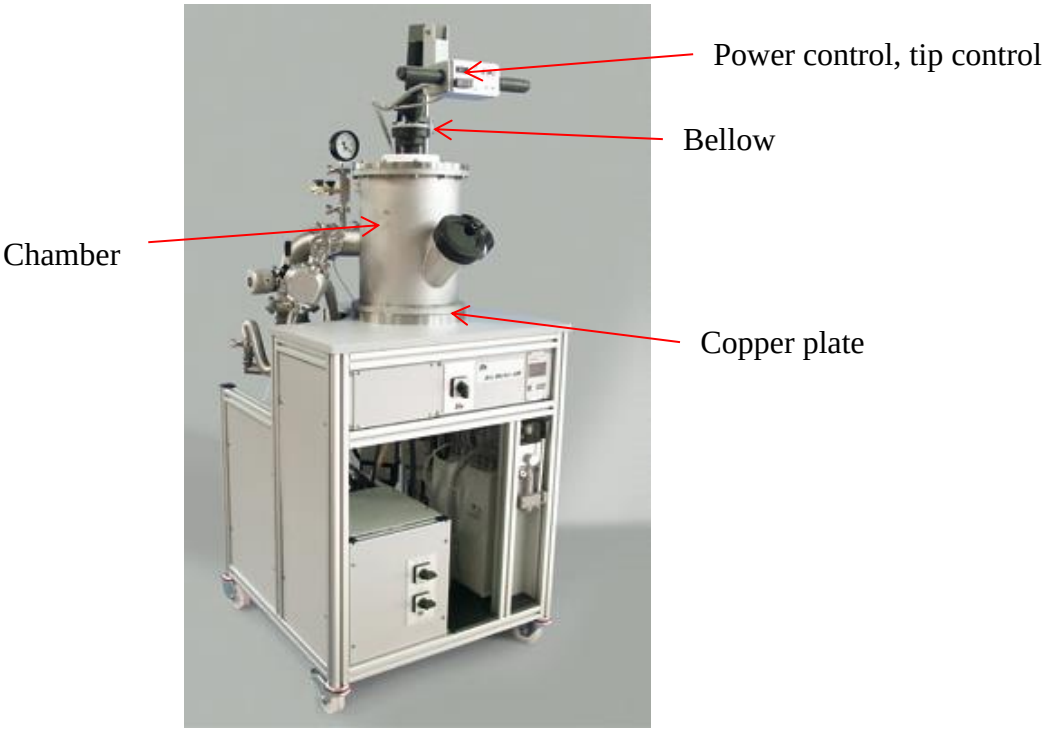

Figure 3.1 Arc-melter picture from Edmund Buehler

The detail operation of arc melting is shown below:

Step 1. Weigh metals, the total weight should not be over 15 grams

Step 2. Put a cleaned getter (Titanium metal) to remove oxygen of the chamber.

Step 3. Clean the metals with ultrosonication; clean the copper plate

Step 4. Put the metals inside the chamber on the copper plate

Step 5. Pump the chamber with rough pump V3 (valve), if it does not leak the pressure will get to number 3-4x10^{-2} easily. If the pressure decrease is slow, check the bellow and the O-ring. Bellow change may be necessary. Make sure the valve connected to the splat quencher chamber is closed.

Step 6. Turn on the turbo pump valve V7 and close V3 at the same time, before engage the turbo pump, open the back of the turbo pump (V6).

Step 7. When reading goes down to 8.3x10^{-6} turn off the turbo pump valve (V7).

Step 8. Make sure the turbo pump valve (V7) is closed before turn on V2 (gas refill pump), fill the gas to -15 Hg.

Step 9. TURN ON THE WATER before arc melting.

Step 10. Turn on the power source nearby the arc-melter (Blue source)

Step 11. Put on glasses for arc flash protection and the lid of the viewing window.

Step 12. Excite the arc and eliminate the oxygen inside the chamber. Lower the tip close/near to the getter but do not touch the tip, turn on the arc with the handle switch. Slowly lever the tip and increase the power. Melt the Titanium getter and observe the getter. If it seems the getter is not melting into hot liquid and oxidized instead, turn off the power and the power source check the leak. If not melt the getter to red hot for 2-3 minutes then turn off the power and wait the getter cool down. Pay attention not let the tip touch the melt getter.

Step 13. After the getter cool down, excite the arc the same way with step 12. Move the arc above the melts that needs to be alloyed. Pay attention to the arc which may

blow away the small pieces of the metals. Heat the metals into one bottom and red hot for 2-3 min and move to another batch until finished.

Step 14. Wait the chamber to cool down. Touch the chamber base until it is not super hot, ~20 min, feel the temperature by hand.

Step 15. Refill the chamber with air after cool down. Flip all the bottoms with clean tweezer and repeat.

Step 16. Fully alloyed can be achieved with two flip.

Step 17. Maintenance of the tip: sharpen the tip with gridding wheel if the arc is split or not strong with appropriate power (cannot quit melt the metals). Clean the tip with acetone and ethanol. Put the tip back and tighten it to make the tip fully contact with the connection.

Important note: a) It is recommended to turn on the cooling water at the very beginning; b) turn on the turbo pump valve only when the pressure is lower enough and the back of the turbo pump has been vacuumed by rough pump; c) turn on the refill gas valve only after turbo pump valve is closed; d) Never put the tip too close to the getter/buttons, if the arc seems not right, this may also due to the oxygen inside the chamber

Figure 3.2 Alloy buttons after arc melting. Button on the left is $Ni_{60}Nb_{35}Zr_5$, button on the right is $Ni_{60}Nb_{35}Sn_5$

3.2.2 Membrane Synthesis

A splat quencher (model: Edmund Buehler, model Buehler Splat Quencher) was used to synthesize the membranes. The thickness of the membranes is 45 μm ± 5 μm and the diameter of the membranes is 20-25 mm. The splat quencher reaches cooling rates of up to 10^6 K/S (Ge et al. 2008), which is capable of synthesizing amorphous Cu-Zr alloys

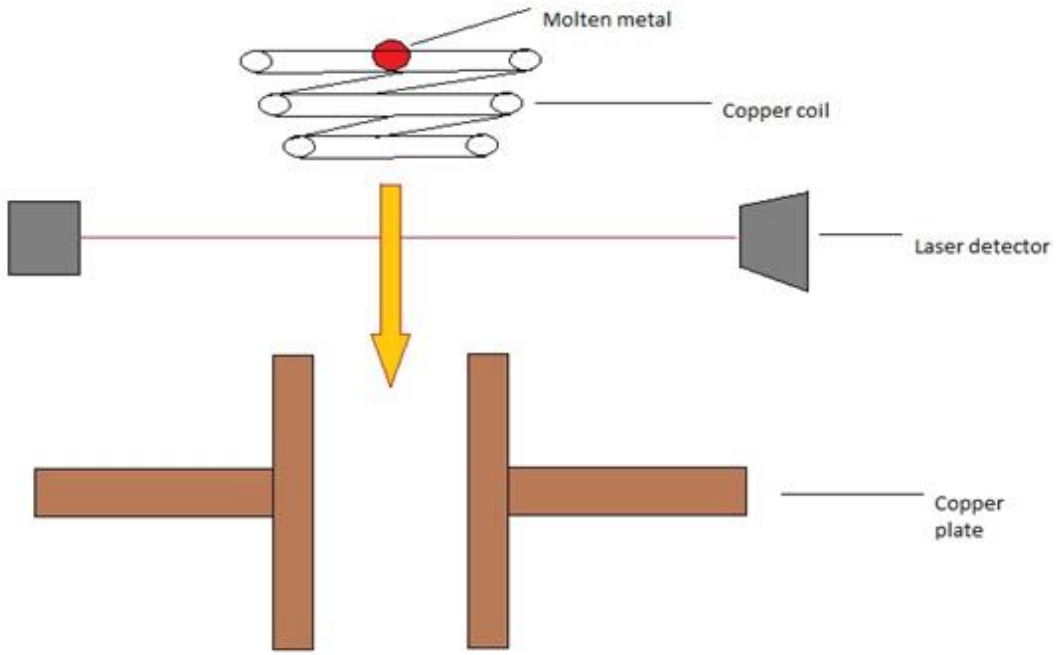

Figure 3.3 Schematic drawing of splat quenching process

according to the GFA predicted by Ge et al. (Ge et al. 2007). Small pieces of alloys were cut from the alloy buttons. A mini arc-melter from Edmund Buehler were utilized to getting the metallic pieces into sphere shape. The weight of the metal piece is between 90 mg – 190 mg, weight out of that range would cause levitation failure. The weight is composition dependent and has to match the power level of the copper coil (RF) coil. First the chamber was vacuumed down to 10^{-5} Torr in case there is arc during the process which would trigger the laser detector and the copper plate would splash before levitation.

When the power is on, the current through the RF coil provides heat and magnetic field to melt and levitate the metal pieces. When the metal piece is fully molten (white molten according to the color of the piece) cut the power. As soon as the power is cut, the molten metal drops and triggers the laser detector which would cause the copper plates closed together instantly. Thus the copper can rapidly cool down the molten metal piece.

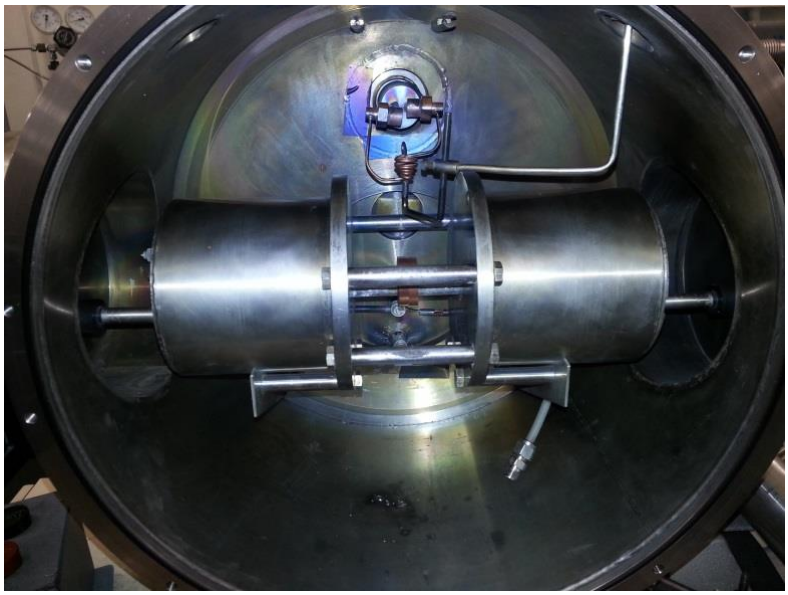

3.4 Splat quencher interior after splat is done, and the chamber is open

A detail operation of splat quencher is shown below:

Step 1. Cut the alloy into small chucks (~100mg).

Step 2. Arc melt the small chucks into balls that can be placed on the crucible for splat quenching.

Step 3. Align the laser so that the dropped molten metal could trigger the copper splats.

Step 4. Vacuum the chamber of the splat quencher. The procedure is the same with vacuum the chamber of arc melter. Turbo pump valve does not have to be closed during splat.

Step 5. Turn on the cooling water before doing splating

Step 6. Turn on the power, set the power and write down the number for record.

Step 7. Set the latent time of the splats.

Step 8. Turn on the laser and the laser sensor.

Step 9. Turn on the power and lower the crucible at the same time. If the metal does not levitate, the either power needs to be adjusted or the coil needs to be changed. Lower the crucible until it is out of the coil and get the crucible holder out of the way of the molten drop.

Step 10. When the metal chunk is red hot and levitate stable inside the coil, press the power shut off button near the chamber. If it is not successful, check the position of the coil.

Step 11. When finished, with or without the splats, turn off the turbo pump then back flash the chamber with air.

Step 12. Clean the chamber, polish the copper plate.

Step 13. There are many parameters that can be adjusted to maximize the operation:

i) The weight of the metal chunk, usually ~100-150 mg

ii) The power of the RF coil

iii) The position of the laser; pay attention to the window before the laser source and the mirror inside the window of the front door, dirty things can block the laser or the laser sensor

iv) The shape of the RF coil. More coils mean large power. The ideal levitation is when the molten metal is in the center of the RF coil and could trigger the laser sensor.

Step 14. Trials and errors are needed to optimize the levitation process.

Palladium was deposited on both of the surface of the membranes to promote hydrogen dissociation through direct current (DC) sputtering with a Lesker Supersystem II. The membranes were annealed at 250 °C for half hour in a vacuum oven (10 kPa) to promote Pd bonding to the amorphous alloy. Without annealing, the Pd layer delaminated from the membrane during hydrogen permeation testing.

Step I. Clean the gun parts. Ultra sonicate the gun parts in ethanol.

Step II. Vent the system

1. Turn off ion gauge, left, close to the plugs. Grey and blue.
2. Turn off the gate valve
3. Turn on the vent valve (gold one), always to remove lead bricks!
4. Turn on nitrogen leak valve (green one) slowly! Look at the gauge rise, more to perpendicular/parallel.
5. Until light through the slit, close the N2 green valve.

Step III. Pump the system

1. While waiting for the system to pump, fill the LN at for both sorption pumps. Be careful with the sound
2. Turn on the venturi pump (N2 valve then black valve) to the gauge reach -45.
3. Turn off the venturi pump first (black then close N2 small valve) then On left sorption pump till center gauge to 0.6
4. Turn on the right sorption valve then off the left sorption valve.
5. Wait until .005
6. Turn off yellow valve to isolate vent/pump system.

7. Turn off sorption pump

8. Turn on gate valve to intermediate wait to .001, then fully on.

9. Turn on the ion gauge to bayard alpert, press 2 then 3.left bottom.

Step IV.DC operation

1. Working pressure 2x10-7Torr

2. Gate valve to intermediate

3. Turn off the ion gauge

4. Open Ar leak valve to 10mTorr, number to 100. Slowly.

5. Turn on cooling water

Step V. Sputtering

1. Switch the sample holder, lock it and spin.

2. Main power to DC power.

3. Stby to watts, now plasma on. Power is 40 W. Clean the target for 1-2 min.

4. Then turn on the shutter and timing. 12min.

Annealing was conducted in tube furnace under inert gas ($He/N_2/Ar$) which is in LE-CSSS center in ASU.

3.2.3 Characterizations

3.2.3.1 Structure

The extent of amorphicity or crystallinity of the membranes was analyzed with X-ray diffraction (XRD, Philips PANalytical X'Pert Pro Cu Kα at 40 kV and 40 mA). Only membranes that exhibited an amorphous broad peak were used for hydrogen permeation tests. Because of the good GFA, most of the membranes fabricated are amorphous. After palladium deposition and annealing, the broad amorphous background was still showing

up; the crystalline peaks in the XRD patterns were found to be from the crystalline Pd coating only.

3.2.3.2 Surface depth profile

Rutherford Backscattering Spectroscopy (RBS) with a 2 MeV He + incident beam to was utilized determine the thickness of the deposited Pd layer. The RBS data was analysized using the RUMP software package (Rutherford Backscattering Spectroscopy Analysis Package, Genplot, Cortland,OH).

X-ray photoelectron spectroscopy was performed before Pd deposition, XPS VG ESCALAB 220i with an Al monochromatic source Kα (12 KV, 65 W, hν = 1486.6eV). Binding energy was calibrated with pure Ag with Ag $3d_{5/2}$ at 368.2eV (Nyholm and Mårtensson 1981) and Casa XPS software was applied to analyze chemical shifts of elements.

3.2.3.3 Thermal Properties

Differential scanning calorimetry (DSC, TA instrument Q20) was performed to investigate the thermal properties of the amorphous membranes. The heating rate is 20 K/min with nitrogen flow rate of 50 ml/min. The TA instrument software calculated the T_g and T_x (Universal Analysis processing software).

3.2.3.4 Hydrogen permeability test

The process can be referred to Chapter 2, section 2.2.2.3. (Jayaraman et al. 1995; Lai and Lind 2015) Here, the graphite gasket has been changed to copper gaskets. For copper gaskets, annealing in air at temperature over 430°C for 15-20 min is recommended to soften the gaskets before mounting. To maximize the sealing, polishing is also recommended to reduce the surface roughness. The copper gaskets were polished

up to 2400 grit sand paper and ultrasonically cleaned to optimize their sealing properties. The size of the membranes should be large enough to be self-supported between two gaskets.

The leakage rate of the copper gaskets were measured and found that it did not exceed 5% of the tested hydrogen flow rate at 573 K. The effective permeation area of the membranes sealed into the permeation module was 1.82 cm^2.A muffle furnace was used to heat the module to 300 K with a ramp rate of about 16 K / min. K-type thermocouples monitored the temperatures at both the exterior of the module and the interior of the module near the membranes. During the initial ramp to operating temperature N_2 was flushed on the feed side of the membrane and Ar on the permeate side. Mass flow controller controlled the flow rate of all gases. Nitrogen and argon were ultra-high purity grade (99.999%), and a hydrogen generator (VWR International, Model H2PEM-100-L) provided hydrogen with purity of 99.99%+. After reaching the desired temperature, the nitrogen feed purge was shut off and hydrogen introduced and pressurized the cell. A back pressure regulator controlled the feed pressure to 140 kPa. A pressure gauge displayed the pressure of the permeate side, which maintained at 1 atm at all times. An Agilent 7890 gas chromatograph (GC) was used to monitor the concentration of gases in the permeate stream. The total testing time was 5-6 hours. The GC was calibrated with customized gas standards from Air-Products. The permeate flow rate was confirmed with a soap bubble flow meter. The permeability was calculated using Sieverts' law.

$$J = \frac{\bar{P}}{t}(P_H^{0.5} - P_L^{0.5})$$ [Equation 1]

In Equation 1, J [mol s^{-1} m^{-2}]is the flux of hydrogen, $\overline{P}$ [mol m^{-1} s^{-1} $Pa^{-0.5}$]is the permeability , t [m] is the thickness of the membrane; P_H [Pa] is hydrogen partial pressure of the feed side, and P_L [Pa] is hydrogen partial pressure of the permeate side.

3.3 Results and discussions

3.3.1 Structure and thermal properties

Figure 3.5 shows a photograph of the as-cast membrane. The membranes have a diameter of approximately 20-25 mm with an average thickness of 45 μm ± 5 μm. 3.6 shows the XRD patterns of as-cast membranes and after Pd deposition and annealing. The as-cast XRD spectra only show a broad peak centered around 38 °; no sharp (crystalline) peaks exist in the as-cast membrane, confirming the amorphous structure. After Pd deposition and annealing, the broad amorphous peak remained and the sharp peaks matching the crystalline XRD pattern of Pd appear. No other crystalline peaks appeared after deposition, indicating that the annealing did not significantly change the amorphous structure.

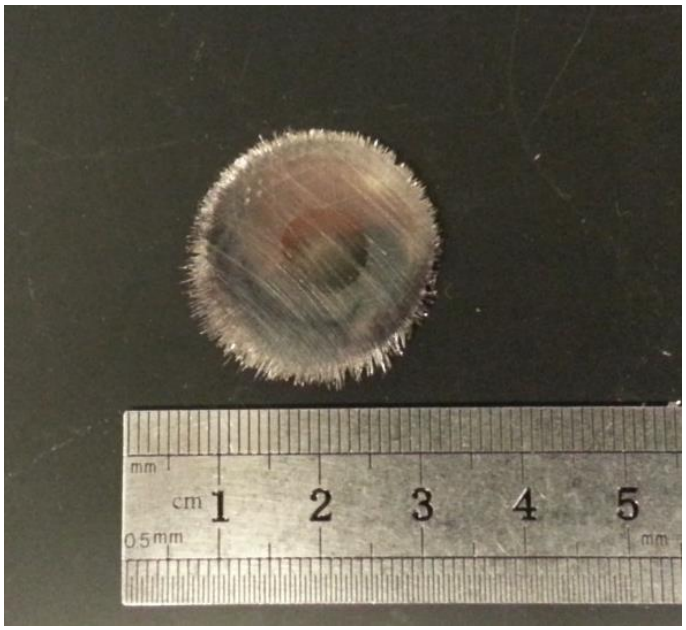

3.5 A picture showing an as-cast $Cu_{40}Zr_{60}$ amorphous piece

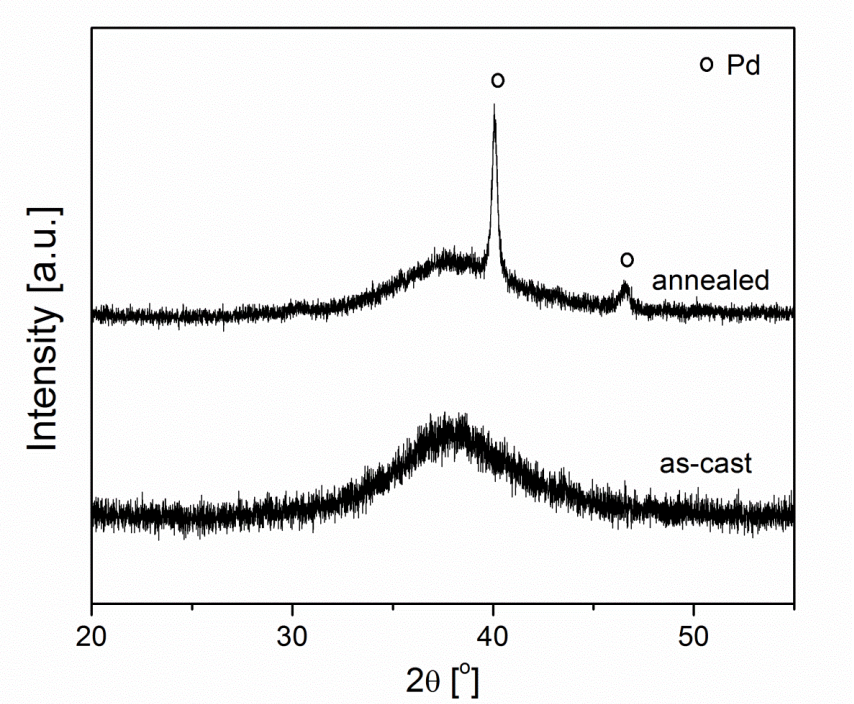

3.6 XRD pattern of $Cu_{46}Zr_{54}$ after casting and after Pd-deposition and annealing

The RBS measurements indicated that the thickness of the Pd layer was about 120 nm on both sides of the membranes. As mentioned before, annealing is necessary to promote the adhesion of Pd with the membranes.

Table 3.1 lists the T_g , T_x and ΔT of the three compositions. The T_gs are comparable to both the theoretical and experimental results.（Jang and Koch 1989; Xu et al. 2004b; Ge et al. 2007; Ge et al. 2008）As the concentration of Zr increased, T_g and T_x decreased. The T_gs do not change after Pd deposition and annealing. The minimum size of the SCLR is 49 K, which indicates that these three compositions have good glass forming ability. According to previous research on Cu-Zr systems, the three compositions that chosen can be formed into bulk metallic glass. (Xu et al. 2004a; Xu et al. 2004b; Zhang et al. 2009) 573 K is chosen to perform the hydrogen permeability test, which is at least 63 K lower than the minimum T_g of the alloys among the three. The previous work has shown that it is possible to anneal an amorphous Zr-based alloy in an inert environment at 50 K below the measured T_g for 8.5 hours and then cycle it to the T_g without changing the alloy properties as measured ultrasonically.(Lind et al. 2006)

Table 3.1 Measured T_g , T_x and ΔT of amorphous metals.

Composition	T_g (K)	T_x (K)	ΔT (K)
$Cu_{63}Zr_{37}$	732	788	56
$Cu_{46}Zr_{54}$	664	713	49
$Cu_{40}Zr_{60}$	640	690	50

The stability tests were performed with $Zr_{54}Cu_{46}$ with DSC. Samples were annealed for two hours at 580, 633 and 653 K under nitrogen. After holding at these temperatures, a regular DSC scan was performed (from the holding temperature to 773 K, with a heating rate of 20 K/s). The samples annealed at 580 and 633 K have the same DSC curves (including T_g, T_x and heat of crystallization) as the as-cast samples. However, after annealing the samples at temperatures 11 K less than the measured T_g of the as-cast

alloy (i.e. annealing at 653 K), the heat of crystallization is slightly different from the as-cast sample.

3.3.2 Hydrogen permeability of Pd-coated and uncoated samples

Figure 3.7 shows the permeability of uncoated and coated Cu-Zr membranes at 573 K with a feed of pure hydrogen at a pressure of 140 kPa (the permeate side of the membrane was kept at atmosphere pressure with an Ar sweep). The raw permeability data is in appendix. The permeability is the maximum data during the testing, because there is no steady state during the test. There is no significant difference in the permeabilities of uncoated and palladium coated $Cu_{63}Zr_{37}$ and $Cu_{46}Zr_{54}$. However, there is a significant difference in the permeability of the uncoated and palladium coated $Cu_{40}Zr_{60}$. The hydrogen permeability shows 1) there appears to be no correlation between the Zr-content of the membranes and the overall hydrogen permeability; 2) the Pd coating does not seem to improve the hydrogen permeability compared to the as-synthesized membranes; 3) the hydrogen permeability at 573 K is much lower than the simulated data with same temperature and feed hydrogen partial pressure. Two hypotheses can explain these observations. First, there are surface oxidation on the surface of the membranes which create transport resistance. Second, the thermal stability needs to be re-evaluated under hydrogen atmosphere. Though the testing temperature is much lower than the glass transition temperature, the presence of hydrogen facilitates the crystallization process. While in simulated conditions, the short range structure change brought by hydrogen solute into the bulk is not taken into consideration. The process is very complicated to simulated instantaneously. There are limited data on the structure (enthalpy of state) relationship with the hydrogen permeability at certain temperature. That is the reason of

actual experimental results deviated from the simulated results, especially at elevated temperature. The following characterizations results will validate the explanations.

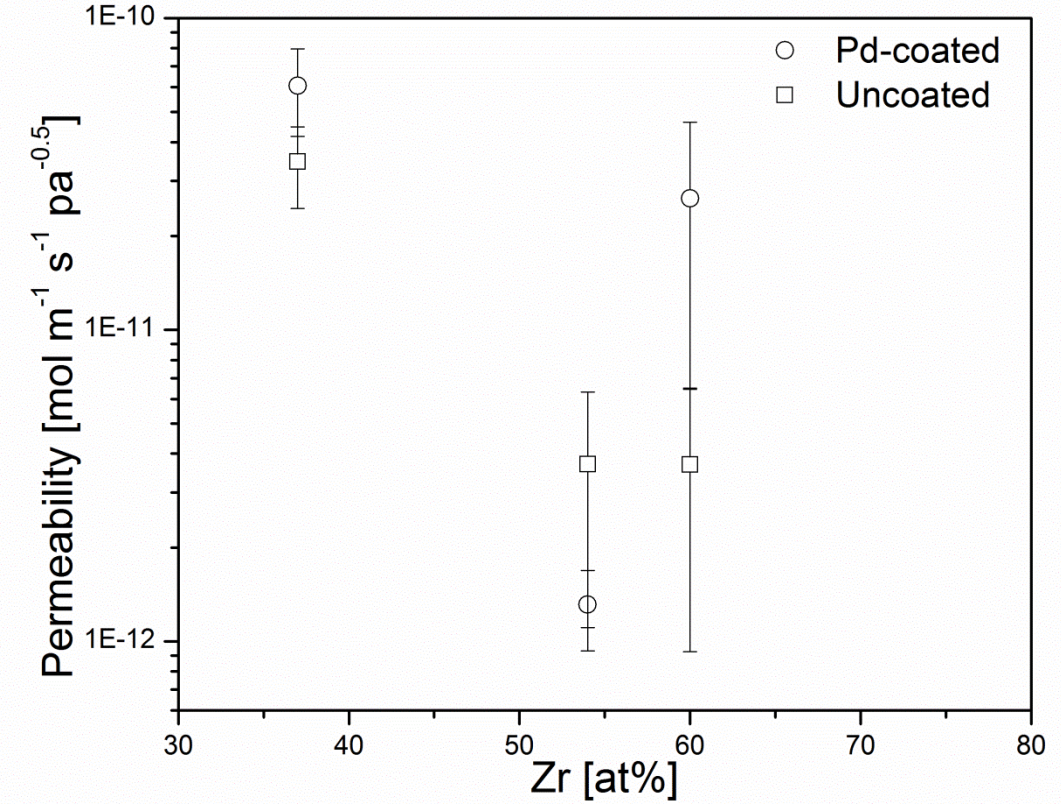

Figure 3.7 Hydrogen permeability of uncoated and Pd-coated amorphous metallic membranes

3.3.3 Surface oxidization and thermal stability

Figure 3.8 shows the RBS spectra of as-synthesized membranes (before coating with Pd and before permeation testing). The penetration depth of RBS can exceed 10 μm with a resolution limit of 3 nm.(Sie 2003) The RBS test could enable us to collect the depth profiles of the surface region of the tested samples.(Sie 2003) The simulation results show that the oxides layers are present on the surface of the samples. In, a RUMP

simulation shows that peaks around 1.65 MeV (Channel 330) indicate the presence of zirconium oxides and a peak around 1.5 MeV (Channel 300) indicates the presence of copper-zirconium oxides. In (a), $Cu_{63}Zr_{37}$ samples have zirconium oxide and copper-zirconium oxide layers of total thickness about 130 nm. In (b), there is zirconium oxide layer of approximately 8 nm and copper-zirconium oxides approximately 10 nm on the surface of as-synthesized $Cu_{46}Zr_{54}$. In (c), there is about 5 nm of zirconium oxides on the surface of $Cu_{40}Zr_{60}$. XPS was also performed which has a penetration depth of a few nanometers.(Schulz et al. 1984) The XPS results (not shown here for brevity) indicate that all the three compositions have small amounts of zirconium and copper oxides present on the surface. The presence of surface oxides on the $Cu_{63}Zr_{37}$ (surface oxides ~130 nm thick) and $Cu_{46}Zr_{54}$ (surface oxides ~18 nm thick) amorphous metallic membranes explain the insignificant difference in permeability between uncoated and Pd-coated samples. This also explains why the Pd-coated $Cu_{46}Zr_{54}$ membranes exhibit a slightly lower average permeability (although not one that is statistically different) than the un-coated $Cu_{46}Zr_{54}$ membranes. Although Pd effectively dissociates hydrogen, the

surface oxides on the amorphous metallic membranes may act as a transport barrier, counteracting the catalytic effect of the Pd. In the case of $Cu_{40}Zr_{60}$, there is limited, if any,

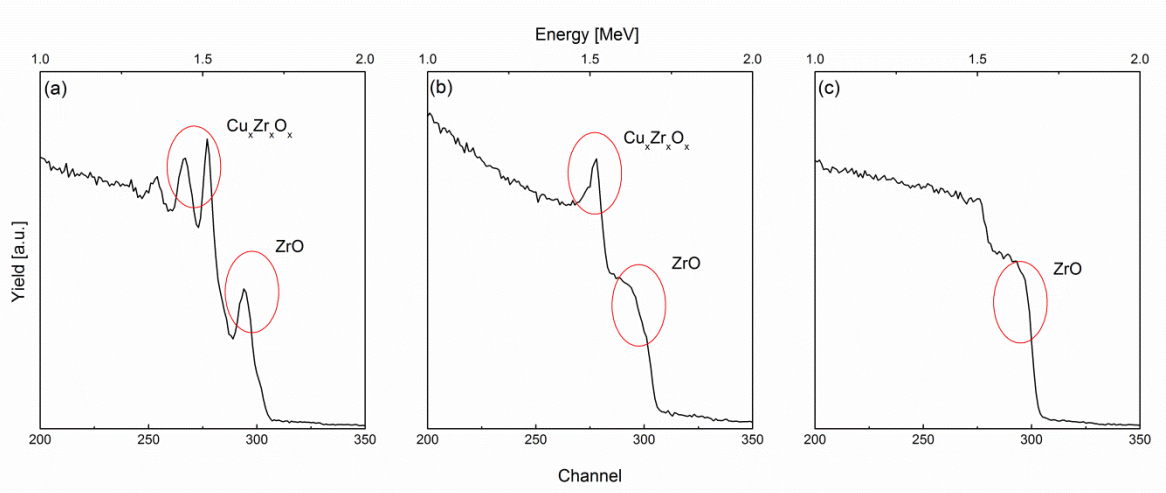

Figure 3.8 RBS spectrum of as-synthesized (a) $Cu_{63}Zr_{37}$, (b) $Cu_{46}Zr_{54}$ and (c) $Cu_{40}Zr_{60}$ (before coating and before hydrogen permeation testing). The red circles indicate the presence of oxides

oxide (~5 nm thick) present on the membrane surfaces, therefore the catalytic effect of the Pd is still seen in increasing the hydrogen permeability. Thin layers (10s of nanometers) of surface oxide could readily result in large resistance to the hydrogen transport because hydrogen transport through dense metallic membranes is by a dissociation-solution-diffusion process.(Ward and Dao 1999)

It is very difficult to eliminate all oxides in the synthesis of a metallic glass.(Gebert et al. 1999; Schroers 2010) Thermodynamically, it is favorable for oxides to migrate to the surfaces of a metallic glass.(Gebert et al. 2010) Zirconium-oxides have a larger negative heat of formation than copper-oxides (at 298 K the heats of formation of oxides are CuO: -156.1 KJ/mol, Cu_2O: 170.7 KJ/mol, ZrO_2: -1097.5 KJ/mol (Ihsan Barin 1989)). However, according to the RUMP simulation, the composition with the highest concentration of Zr ($Cu_{40}Zr_{60}$) has the least oxides on the surface. Sen et al. found the Cu-

Zr alloy with higher Zr concentration has a lower surface oxidation rate both in crystalline and glassy states.(Sen et al. 1984) This could be attributed to the different growth rate of different oxides which is determined by the Cu/Zr composition ratio as shown by Hickman et al. found that between 573 K to 773 K only copper oxides can form in $Zr_{20}Cu_{80}$.(Hickman and Gulbransen 1948) Both reported by Sen et al. (Hickman and Gulbransen 1948) and Hickman et al. (Sen et al. 1984) agree with the observations. Also, it is possible that the surface composition of the as-cast membranes is different than the bulk composition. Because Cu has a lower surface energy (1.79 J/m) than Zr (2.0 J/m) (Schroers 2010), copper has the tendency to migrate to the surface of the alloy.

Figure 3.9 (a) shows the hydrogen permeability of a Pd-coated $Cu_{63}Zr_{37}$ membrane as a function of time during the permeation test. Figure 3.9 (b) shows the

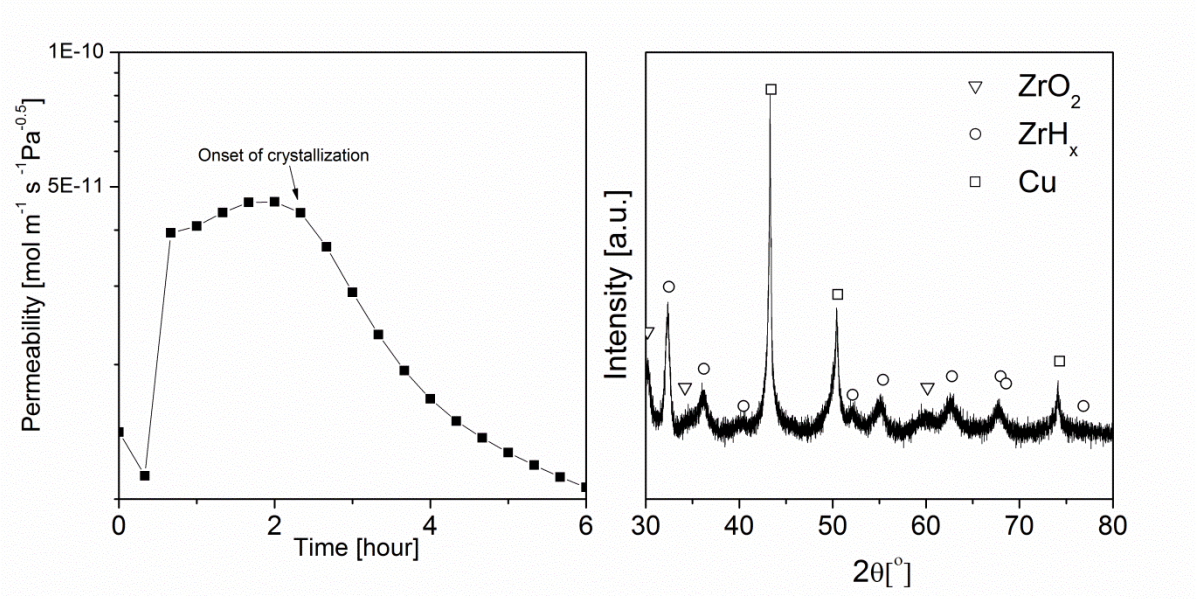

Figure 3.9 (a) Permeability vs time during the hydrogen permeation test of a Pd-coated $Cu_{63}Zr_{37}$ sample (b) XRD pattern of an uncoated $Cu_{63}Zr_{37}$ membrane permeate side after completion of the hydrogen permeation test.

XRD spectrum of the permeate side of $Zr_{37}Cu_{63}$ after the completion of the hydrogen permeation test. The system permeation error is within 10%. As Figure 3.9 shows, after

two hours of testing, the permeability starts to decrease and the permeability continues to decrease through the end of the test (~ 6 hours). This may be the result of the presence of the oxides (the reduction during the test) and amorphous structure relaxation.(Dini and Dunlap 1985) The onset of crystallization may happen sometime during the third hour of testing (as indicated by the decrease in permeability seen around 2.5 hours of testing). Although a testing temperature of 573 K was used, which is 159 K lower than the T_g of $Cu_{63}Zr_{37}$, it is hypothesized that with the presence of hydrogen, the structure relaxation and formation of hydride may left shift the TTT curve of Cu-Zr alloys (the nose moves to a lower temperature) which accelerated the crystallization of amorphous membranes. (Dini and Dunlap 1985; Eliaz and Eliezer 1999) Crystallization of an amorphous alloy further decreases the hydrogen permeability.(Paglieri et al. 2011a; Paglieri et al. 2011b) The crystallization of Cu-Zr may be the result of the formation of hydrides. As is shown in Figure 3.9(b), there are peaks corresponding to zirconium hydrides and zirconium oxides after permeability test. Zr has a large, negative hydride heat of formation.(Griessen and Driessen 1984) The strong affinity of Zr for hydrogen facilitates hydrogen absorption of the alloy with higher concentration of Zr.（Yamaura et al. 2005; Paglieri et al. 2011a） But the formation of zirconium hydride promotes crystallization and is detrimental to the thermal stability. The compositions with refractory elements may be better in thermal stability perspective.

3.4 Conclusions

Three compositions of Cu-Zr (Zr at% = 37, 54, 60) amorphous metallic membranes were fabricated by splat quenching. The amorphous nature of the as-cast

membranes was verified with XRD. A palladium catalytic coating was applied to promote hydrogen dissociation and recombination. Hydrogen permeability of the amorphous free-standing membranes was tested at a feed hydrogen pressure of 140 kPa. The hydrogen permeability was lower than that predicted by the first-principle calculation. The observed permeability was explained by oxide formation on the surface. The variation in oxide thickness may be the result of the formation of different oxides as a function of the Cu/Zr composition ratio and different growth kinetics of them. The stability test and the permeability test indicate that the presence of hydrogen accelerated crystallization which leads to significant permeability degradation. Overall, the thermal stability of amorphous metallic membranes is very important for hydrogen separation applications.

CHAPTER 4 HYDROGEN PERMEABILITY OF NI-NB-X (X=SN, TI AND ZR) AMORPHOUS METALLIC MEMBRANES AND MECHANICAL PROPERTIES CHANGE BY HYDROGEN

4.1 Introduction

Amorphous metals are formed through rapid cooling. The amorphous structure exhibits a crystallization temperature (T_x) and glass transition temperature (T_g). In hydrogen membrane separations, higher temperatures can promote increased hydrogen transfer through the membranes. When amorphous metals are held at temperatures near T_g for extended periods of times, crystallization occurs. Therefore, for hydrogen separation applications, amorphous metals with higher T_g relative to the temperature of the hydrogen separation are preferable to those with lower T_g. (Lai et al. 2015) Binary Ni-Nb based amorphous metals have high T_gs.(Klement et al. 1960; Lovallo et al. 1998) According to Inoue, the more the elements, the more stable an alloy system can form in glassy states.(Inoue 2000) Ternary NiNb-based systems like $Ni_{60}Nb_{35}Sn_5$,(Choi-Yim et al. 2003) $Ni_{60}Nb_{35}Ti_5$ (Klement et al. 1960) and $Ni_{60}Nb_{35}Zr_5$ (Lovallo et al. 1998) etc. have shown good glass-forming ability and also high T_gs.（Qiang et al. 2007; Zhu et al. 2007; Qiang et al. 2009） It is necessary to find a delicate balance between hydrogen permeability and thermal stability of the amorphous metallic alloys. Zirconium has a very strong affinity for hydrogen.(Griessen and Driessen 1984) While Suh et al. found that Zr concentration greater than 20 at% in Ni-Nb alloy does not improve hydrogen permeability further, because the mobile hydrogen does not increase.(Wang et al. 2013)

Also compositions with higher Zr concentration have lower T_g which is detrimental for the thermal stability.

Hydride formation during hydrogen separation in amorphous metallic membranes promotes hydrogen embrittlement and crystallization, both of which can result in mechanical failure. The potential hydride formation causes mechanical failure and thermal stability decreases over time. The effects of hydride formation have been widely investigated for crystalline alloys.(Mueller et al. 2013) Because there are no defects (grain boundaries, etc) in amorphous metals, the failure mechanism of crystalline materials is different from that of amorphous materials.(Murali and Ramamurty 2005; Zhao et al. 2014b) Thus it is necessary to investigate the behavior of amorphous metals with the influence of hydrogen. The deformation involves more with shear band for amorphous alloys than slip bands in crystalline alloys.(Schuh et al. 2007) Nanoindentation is a method widely used to investigate the mechanical properties of materials with submicron dimensions that are not suitable for traditional indentation.(Deng et al. 2004; Dudek and Chawla 2010; Singh et al. 2014) For example, solders form an intermetallic phase during service which causes mechanical failure. The mechanical properties of the intermetallic phase are difficult to access through microindentation and macroindentation techniques but could be easily probed by nanoindenter. (Choi-Yim et al. 2003; Murali and Ramamurty 2005) Continuous measurement of stiffness (CSM) nanoindentation has advantages over the traditional method developed by Oliver and Pharr(Oliver and Pharr 1992) by instantaneously obtaining the information over the test depth.(Fischer-Cripps and C. 2004; Hay et al. 2010) Zhao et al. utilized nanoindentation to probe Ni-Nb-Zr amorphous metals after

hydrogen charging, they found a softening effect happened within the high Zr content systems.(Zhao et al. 2014b) In this study, the effects of different substitutions to the NiNb base alloys on the nano-modulus and nano-hardness will be discussed.

In this chapter, $Ni_{60}Nb_{35}X_5$ (X=Sn, Ti and Zr) amorphous metallic membranes were synthesized. The membranes with XRD were characterized to verify the structure and the thermal properties were measured with differential scanning calorimetry (DSC). CSM nanoindentation was applied to investigate the mechanical properties change incurred by hydrogen. The hydrogen permeability of amorphous membranes was tested at 673 K. Results show that low levels of substitution of a third element (5 at%) into the NiNb binary alloy (for Nb) influence the hydrogen permeability according to the hydride formation enthalpy of the elements. The hydrogen permeability still decreased during the testing time, which may due to free volume decrease. These ternary $Ni_{60}Nb_{35}X_5$ exhibit better thermal stability than CuZr binary system. This is the first report of the experimentally measured hydrogen permeabilities of amorphous metallic $Ni_{60}Nb_{40}$ membranes with a low concentration substitution for Nb.

4.2 Experiments

4.2.1 Materials

Raw metals (Ni,Nb,Sn,Ti and Zr) were purchased from Alfa-Aesar with purity of 99.999%. The raw metals were cleaned with ultrasonication in acetone, then in ethanol; weighed and arc melted (Edmund Buehler, model AM) under argon atmosphere into buttons. The buttons were flipped twice to guarantee complete alloying during arc-melting process.

4.2.2 Membrane synthesis

Membranes were synthesized by splat quenching (Edmund Buehler, model Buehler Splat Quencher). The splat quencher can provide a cooling rate up to 10^6 K / s The thickness of the membranes is 45 μm ± 5 μm with diameter of 20-25 mm. Palladium was sputtered (DC, Lesker Supersystem II) on both surfaces of the membranes to promote hydrogen dissociation and recombination. Before sputtering, the membranes were polished by 2400 grit SiC sand paper to remove the surface oxides and cleaned ultrasonically. After sputtering, the membranes were annealed at 573 K for one hour in tube furnace (Thermo Scientific Lindberg Blue M 3 Zone Tube Furnace) with UHP He/Ar flushing to promote Pd adhesion to the membranes. The details of alloying and splat quenching can be refereed to Chapter 3.

4.2.3 Characterizations

4.2.3.1 Structures

The amorphous nature of the as-cast membranes was verified by using X-ray diffraction (XRD, Philips PANalytical X'Pert Pro Cu Kα at 40 kV and 40 mA). The majority of membranes synthesized are amorphous. After palladium deposition and annealing, the samples still maintain their amorphous nature; crystalline peaks present in the XRD patterns are only from the Pd coating.

Rutherford Backscattering Spectroscopy (RBS) with a 2 MeV He + incident beam was used to determine the thickness of the deposited Pd layer. According to the RUMP software package (Rutherford Backscattering Spectroscopy Analysis Package, Genplot, Cortland,OH), the thickness of the Pd layer is about 120 nm.

4.2.3.2 Thermal Properties

Differential scanning calorimetry (DSC, Netzsch STA 449C) with a heating rate of 20 K/min and nitrogen flow rate of 50 ml/min was used to investigate the thermal properties of the amorphous membranes. The Proteus® software calculated the T_g.

4.2.3.3 Nanoindentation

4.1 Equipment used to collect nanoindentation data from the membranes.

Nanoindentation was performed before and after hydrogen permeability tests using a commercial nanoindenter (Nanoindenter XP-II, Agilent) equipped with a Berkovich tip. The membranes were first glued to a flat rectangular Al 7075 alloy blocks using super glue (All Purpose Krazy Glue®). The membrane was then polished to a 1 µm diamond finish and to a final finish of 0.05 µm colloidal silica. The polishing also removed the top layer of the palladium deposited on the surface. The Al 7075 blocks, with polished membranes attached to it, were mounted on aluminum stubs for nanoindentation testing using spur glue. The nanoindenter was first calibrated by measuring Young's modulus and hardness of a silica standard. Tests were conducted in strain rate control mode with a strain rate target of 0.05 s^{-1}. A continuous stiffness

measurement (CSM) technique was used during indentation, where a load is applied to the indenter tip to drive the indenter into the specimen surface while concurrently superimposing an oscillating force with a small amplitude (significantly smaller than the nominal load). An accurate measurement of contact stiffness at all indentation depths is provided by separating the in-phase and out-of-phase components of the load-displacement data(Dudek and Chawla 2010; Singh et al. 2014). The advantage of CSM is that the modulus and hardness can be measured with indentation depth and therefore multiple indentations at different depths are not necessary. Nanoindentation was carried out on at least 20 locations to a depth of 1000 nm per indentation. Young's modulus and hardness for an individual indentation were measured as the average value over a depth range where both modulus and hardness were independent of depth. Scanning electron microscopy (Philips XL-30) was used after the experiments to observe the indentions and energy dispersive spectroscopy (EDS) was used to confirm the composition of the membranes and absence of palladium of the surface.

Young's modulus of a membrane can be calculated from the reduced modulus (E_r) according to the following equation(Deng et al. 2004):

$$\frac{1}{E_r} = \frac{1-\nu^2}{E} + \frac{1-\nu_i^2}{E_i}$$

Where E_i and ν_i are Young's modulus and Poisson's ratio for the indenter and$E$ and ν are for the membranes. Poisson's ratio of the amorphous Ni60Nb40 and Ni60Nb35Sn5 were calculated to be 0.37,(Libowitz and Maeland 1984; Choi-Yim et al. 2006) thus all the compositions' Poisson's ratio is assumed to be 0.37. Hardness (H) of membrane is

calculated as the ratio of the applied load to that of the contact area (A), i.e. H = P/A.

4.2.3.4 Hydrogen permeability test

The hydrogen permeability was measured in aforementioned custom-built cross-flow testing system (Lai and Lind 2015; Lai et al. 2015). Annealed copper gaskets were utilized to maximize the sealing(Lai et al. 2015). Copper gaskets were manufactured by Copper Gasket Unlimited in Arizona. The leakage rate of the copper gaskets did not exceed 5% of the tested hydrogen flow rate at 673 K. Tests detail procedures can refer to previous chapter. In order to minimize the ramp duration, the heating procedure needs to be adjust. A maximum heating rate is possible with much higher targeted temperature. By controlling the heating time, duration of one hour is needed for the temperature stabilized at 673 K. Trail ramp experiments may be needed to check the temperature profile during heating. The target temperature was 673 K. The feed hydrogen pressure was 120 kPa controlled by a back pressure regulator, and the permeate side was kept at 1 atm monitored by a pressure gauge. Permeability was calculated using Sieverts' law. (Paglieri and Way 2002)

4.3 Results and discussions

4.3.1 Structure and thermal properties

XRD was performed on all of the as cast membranes and the membranes after Pd deposition. As is shown in 4.2, there are no crystalline peaks present in XRD spectra of as-cast membranes, the broad peak centered around 2-theta of 42^{o} verified the amorphous structure. After palladium deposition and annealing at 573 K (to promote Pd adhesion), XRD was performed again. Only crystalline peaks corresponding to metallic Pd appear in

the XRD verifying that the annealing did not change the amorphous structure of the membranes. Without annealing, the Pd layer would delaminate during the hydrogen permeability test because of poor adhesion and pressure difference between feed side and permeate side. After hydrogen permeability test, XRD was performed again to evaluate any changes in the structure of the membranes. 4.2 shows the XRD of three membranes before H_2 test and after H_2 test. Only Pd crystalline peaks show in both of the XRD pattern. After the hydrogen permeation test a broad peak around 20 degree is present in all of the compositions of membranes. There seems no hydride phased formed after permeability test. According to the DSC/TG results, the weight change indicates that even there is hydride formation, the amount is very limited. XRD pattern verified that the amorphous structure did not change during the hydrogen permeability test.

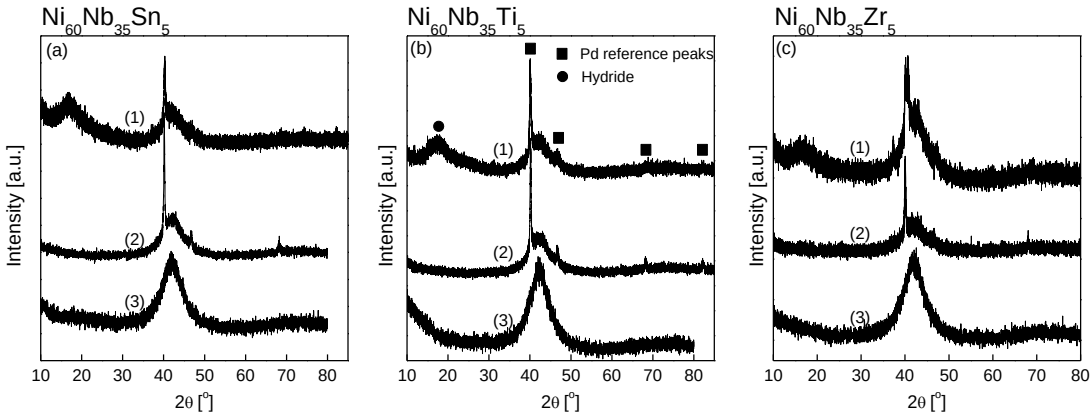

4.2. XRD pattern of a (a) $Ni_{60}Nb_{35}Sn_5$ (b) $Ni_{60}Nb_{35}Ti_5$; (c) $Ni_{60}Nb_{35}Zr_5$, from top to bottom, after hydrogen permeability test (1); after Pd deposition before H_2 test (2) and as cast (3).

Table 4.1 shows the glass transition temperature measured with DSC of the three membrane compositions. A heating rate of 20 K / min is applied because T_g measured by DSC has a slight heating rate dependence. As shown in 4.1, the $Ni_{60}Ni_{35}Zr_5$ alloy has the local maximum glass transition temperature. $Ni_{60}Nb_{35}Ti_5$ has a T_g of 809 K, which is the

minimum of the three alloys. The T_g is at least 72 K higher than of the Cu-Zr binary amorphous metals that were made and tested in previous publication.(Lai et al. 2015) The previous research shows that even with testing temperature 67 K lower than the T_g would cause crystallization after 2 hr of hydrogen permeability test.

Table 4.1 Glass transition temperature before and after hydrogen permeability test

Composition	T_g before H_2test (K)	T_g after H_2 test (K)
$Ni_{60}Nb_{35}Sn_5$	834.3 ± 8.8	824.3 ± 10.7
$Ni_{60}Nb_{35}Ti_5$	808.8 ± 2.8	806.9 ± 22.1
$Ni_{60}Nb_{35}Zr_5$	860.8 ± 18.5	849.1 ± 15.6

In the DSC scans, the ternary alloys show two endothermic peaks of crystallization (not shown for brevity). In previous work with binary Cu-Zr amorphous alloys the DSC scans show a single crystallization peak. Other researcher have observed this phenomena, of two endothermic crystallization peaks, in other multicomponent amorphous metals (Turnbull and Cohen 1961). This may be because the compositions are pseudo-eutectic, which leads to phase separation during the crystallization. All of the ternary compositions show two crystallization peaks. After the hydrogen permeability test, DSC was performed again (Table 4.1). After the hydrogen permeation test (at 673 K) the T_g of the alloys decreased. The largest difference is for $Ni_{60}Nb_{35}Sn_5$ membrane in which the after permeation testing membranes has a T_g that is 12 K lower than the as-cast membrane. The $Ni_{60}Nb_{35}Ti_5$ and $Ni_{60}Nb_{35}Zr_5$ membrane has a T_g that is 5 K lower than the as cast pieces. Not sure why there is difference of T_g change of different compositions. The decrease of T_g is due to hydrogen occupied free volume. However, the two crystallization peaks still appear in the DSC measurement after the hydrogen permeation test, indicating that the membranes maintain amorphous.

4.3.2 Mechanical properties before and after hydrogen permeation test

Representative SEM image of indentation impression is shown in Figure 4.3. Pile-ups of the material in the form of semi-circular shear bands is visible. In general, pile-up is observed around the indents in materials showing little or no strain hardening behavior. The same behavior is exhibited by bulk metallic glasses since they deform in elastic-perfectly plastic manner.（Vaidyanathan et al. 2001; Ramamurty et al. 2005）No significant change in deformation behavior was observed before and after hydrogen permeability test of all the compositions.

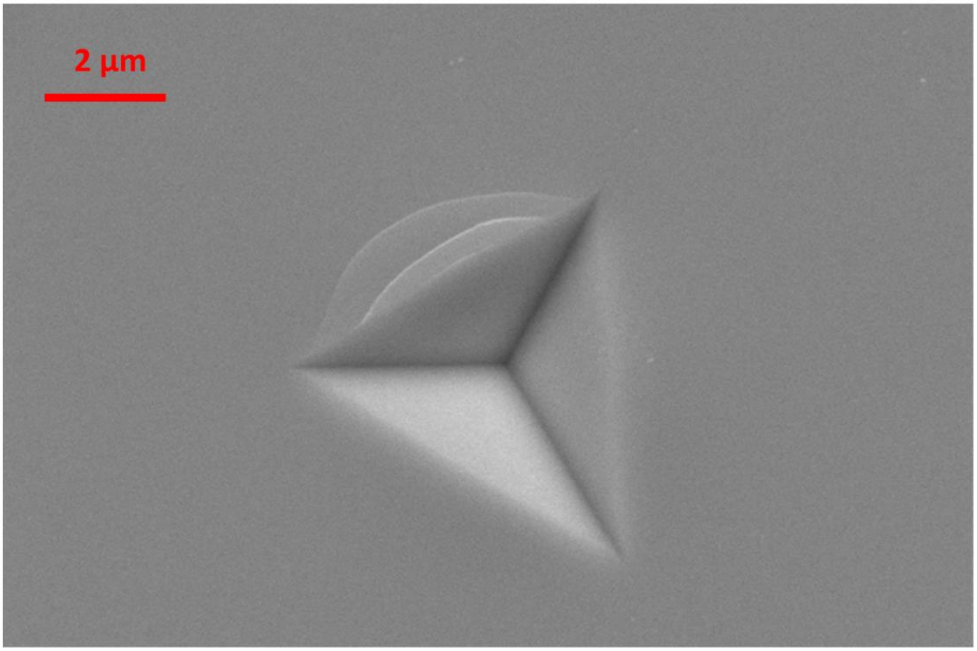

Figure 4.3 Representative SEM image of an indentation: $Ni_{60}Nb_{35}Sn_5$ before hydrogen permeability test, EDS proved that the Pd coating has been polished away

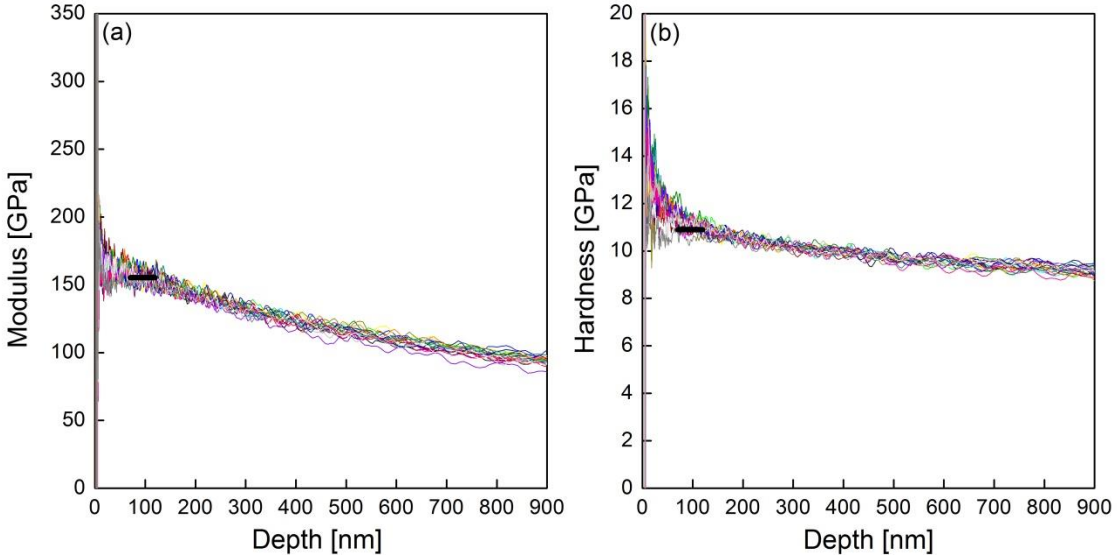

Figure 4.4 Nanoindentation data set of 20 of $Ni_{60}Nb_{35}Zr_5$ membrane before hydrogen permeability test

Figure 4.4 shows the data set of 20 nanoindentation of $Ni_{60}Nb_{35}Zr_5$ membrane before hydrogen permeability test. The black lines label the depth range where the modulus and hardness is collected. The range is determined by the software accompanied with the equipment. After the plateau, the substrate effect starts to show up in the form of decreasing, because the substrate is pure aluminum. Usually, when the indent depth is within 10% of the whole thickness, the substrate effect will not influence the results. It should be noted that CSM technique has been used in this study instead of the conventional Oliver and Pharr method (Oliver and Pharr 2004) and therefore effect of the substrate in these thin membranes can be observed, leading to the accurate measurement of modulus and hardness.

For $Ni_{60}Nb_{35}Sn_5$ and $Ni_{60}Nb_{35}Zr_5$, the Young's modulus and hardness was observed to be constant with respect to depth (plateau region) between approximately 70-120 nm. For $Ni_{60}Nb_{35}Ti_5$ membranes, the plateau was observed between 50-100 nm. The gradual decrease in values of Young's modulus and hardness at the later depths may be

attributed to the combined effect of glue and the Al7075 matrix, also known as the substrate effect in nanoindentation. The Young's modulus and hardness for membranes were averaged in the plateau region, i.e. 70-120 nm for $Ni_{60}Nb_{35}Sn_5$ and $Ni_{60}Nb_{35}Zr_5$, 50-100 nm for $Ni_{60}Nb_{35}Ti_5$. Figure 4.5 summarizes the measured Young's modulus and hardness of the membranes before and after permeability test. $Ni_{60}Nb_{35}Ti_5$ has the local minimum young's modulus with 131.3 ± 4.8 GPa and hardness of 10.19 ± 0.41 GPa before hydrogen permeability test. After hydrogen permeability test, all compositions show an increase in Young's modulus and hardness. Other researchers observed the same phenomena on BMGs.(Suh and Dauskardt 2000) Among three alloy compositions, the $Ni_{60}Nb_{35}Ti_5$ samples have the maximum increase of Young's modulus (28.9 GPa) and hardness (1.2 GPa). The $Ni_{60}Nb_{35}Sn_5$ samples have increases of 21.4 GPa (Young's modulus) and 1.06 (hardness). There is limited hardness change in the $Ni_{60}Nb_{35}Zr_5$ alloys from 11.17 GPa to 11.45 GPa.

The mechanical changes observed after the hydrogen permeability test may be

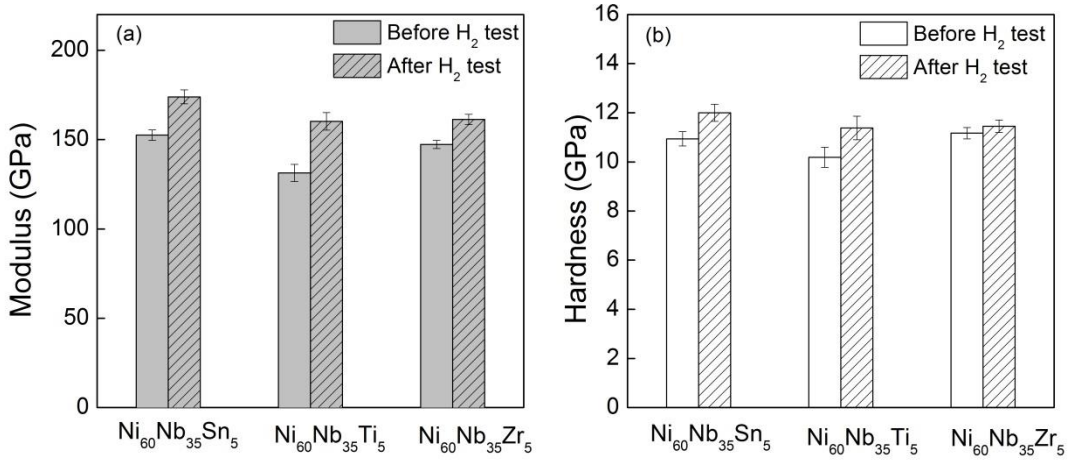

Figure 4.5 (a) Young's modulus before and after H_2 test; (b) Hardness before and after H_2 test

due to the result of free volume decrease instead of hydride formation. Usually the hydride exhibit higher hardness compared to pure element. For example, Xu et al. found that the hardness of titanium hydride is 30% higher than the pure Ti.(Xu et al. 2007) Though there is also research claiming that zirconium hydride formation in an alloy does not change the modulus and hardness when the hydrogen content up to $ZrH_{1.5}$.(Puls et al. 2005) In this study, neither XRD pattern (4.2) nor DSC (Table 4.1) validate that the hydride has formed. The enthalpy of crystallization calculated from DSC curve did not show difference before and after hydrogen permeability test for all the compositions. So the formation of hydride, if there is any, is limited. So the contribution of hydride formation to modulus' and hardness increase is negligible. The free volume decrease can be attributed to two factors: the sub-T_g annealing and the hydrogen solute into the membranes. The sub-T_g annealing of amorphous metal could influence the mechanical properties by redistributing and annihilating free volume. (Porter 2009) The free volume model has been widely applied to explain deformation mechanism in amorphous metals.（Spaepen 1977; Argon 1979; Steif et al. 1982） Flores et al. investigated the free volume change after hydrogen charged amorphous metals. They concluded that the hydride forming element, for example, Ti and Zr, performed as the deep trap for hydrogen atoms would lead free volume decrease in amorphous metals.(Flores et al. 2002) Yoo et.al studied the mechanical properties change after electrochemically charged with hydrogen at room temperature.(Yoo et al. 2010) They found the hardness increased maybe due to the same mechanism of sub-T_g annealing (free volume decrease). The hydrogen permeability test was conducted at 673 K, this can also be considered as sub-T_g annealing with the testing temperature between 0.78-0.83T_g in this case.

4.3.3 Hydrogen permeability and thermal stability

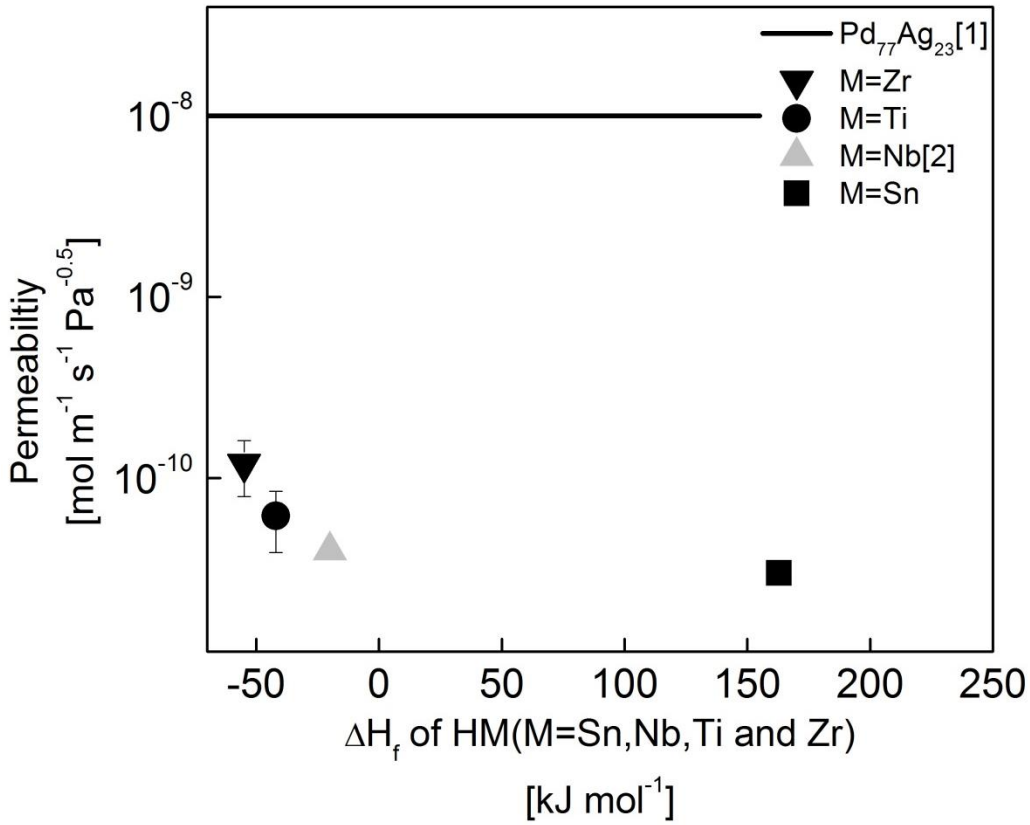

Figure 4.6 [1] $Pd_{77}Ag_{23}$ (Lai et al. 2015), [2] $Ni_{60}Nb_{40}$ (Kim et al. 2012). Hydrogen permeability of amorphous membranes as the function of enthalpy of hydride formation of the ternary substitution element. The compositions of amorphous metallic membranes can be written as $Ni_{60}Nb_{35}M_5$ (M=Sn, Nb, Ti and Zr).

Figure 4.6 shows the hydrogen permeability of tested membranes (at 673 K) as a function of enthalpy of hydride formation of the ternary element addition to the alloy (i.e., Nb, Ti, Zr, and Sn). The reference hydrogen permeability of the binary alloy $Ni_{60}Nb_{40}$ is from Kim et al.(Kim et al. 2012) The enthalpy of Nb (-20 kJ mol^{-1}), Ti (-42 kJ mol^{-1}) and Zr (-55 kJ mol^{-1}) hydride formation is from Wang and Northwood. (Yan-Bin and Northwood 1987) The only Sn hydride that exists is H_4Sn which is in gas phase, the enthalpy of formation is 162.8 kJ mol^{-1}.(Chemical Rubber) The raw data of the hydrogen

permeability can be found in appendix. The ternary allow with the Zr substitution ($Ni_{60}Nb_{35}Zr_5$) has the local maximum hydrogen permeability of $1x10^{-10}$ mol m^{-1} s^{-1} $Pa^{-0.5}$. Because the as-cast $Ni_{60}Nb_{35}Sn_5$ samples are very brittle, only one data point was collected successfully from the hydrogen permeability test. Sn did not show improvement in hydrogen permeability compared to the non-substituted $Ni_{60}Nb_{40}$. Ti and Zr substitution, even at very small substitution concentration improves the hydrogen permeability of the ternary alloy compared to the binary base of $Ni_{60}Nb_{40}$. This indicates the hydrogen permeability increase may be related to the affinity toward hydrogen. There is no clear evidence of hydride formation as mentioned in the last section. Only a broad peak shows up around 20 ° in XRD pattern after hydrogen permeability test of all the compositions (4.2) which may indicate "hydride" formation. Libowitz and Maeland investigated hydrogen interaction with binary amorphous alloy systems.(Cao et al. 2014) They found there is no new phase formation while the hydrogen forms a solid solution. They suggested a form of a novel "hydride" phase may form in the system. This is consistence with what has been observed. As is shown in Figure 4.6 the more positive the enthalpy of hydride formation, the lower the hydrogen permeability is (a positive value of the enthalpy of hydride formation means that the hydride does not form spontaneously – e.g., for Sn). Permeability in dense metallic membranes is the product of the diffusivity and solubility of the desired product within the membrane. The hydrogen attracting elements may promote the solubility of the system.

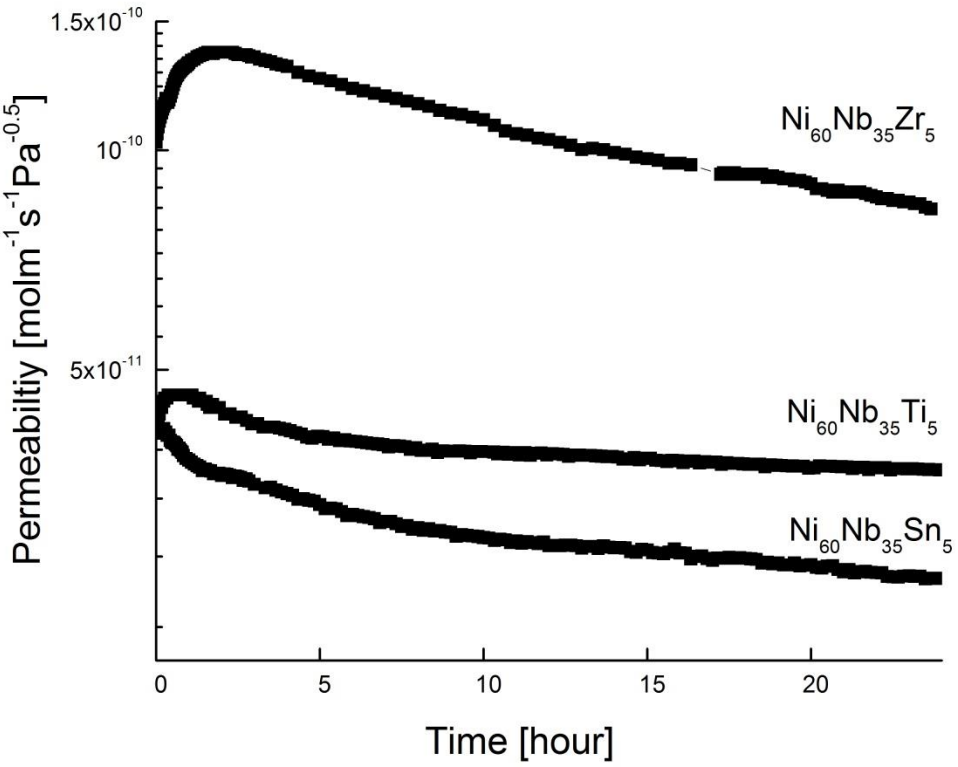

Figure 4.7 Hydrogen permeability as the function of testing time of amorphous membranes

Figure 4.7 is the representative permeability as the function of testing time (24 hours) of each composition. The testing temperature (673 K) is 135 K lower than the minimum T_g measured for $Ni_{60}Nb_{35}Ti_5$. During the test, the permeability decreased for all of the samples. Most of the samples show an initial increase in the first 2-3 hours than followed by the slow decrease over the rest of the testing time. The initial increase may relate to the activation of the catalytic coating or hydrogen activate the soluble sites during the test. The extent of permeability decrease has no relationship with the measured T_g of the alloy. Also, as discussed previously, after the hydrogen permeability test, the membranes maintain amorphous structure according to the XRD test. The DSC curves still show endothermic crystallization peaks. This indicates that the decrease of the

hydrogen permeability is not to the result of crystallization of the amorphous alloy. The observed permeability decrease may be the result of a free volume decrease (which is also the cause of the observed changes in the mechanical properties of the used membranes). Besides sub-T_g annealing, hydrogen atoms absorbed into amorphous alloys leads to the free volume decrease. However, on the whole, the NiNb series have better thermal stability and more resistance to hydrogen embrittlement compared to the family of binary Cu-Zr amorphous metallic membranes.

4.4 Conclusions

The hydrogen permeability of a series of ternary NiNb based amorphous metallic membranes system were experimentally measured. The substitution of Ti or Zr for Nb increases the hydrogen permeability of the ternary alloy compared to the binary alloy. These results show that the hydrogen permeability is related to the enthalpy of hydride formation. For mechanical properties, it is hypothesize that hydrogen occupies some free volume and leads to an increase in the Young's modulus and hardness of the membranes after permeation testing. All of the amorphous membranes exhibit good thermal stability during hydrogen permeation at 673 K as indicated by no significant changes in the hydrogen permeation during the 24 hours of the test time. The NiNb is considered to be a good system as for thermal stability concern.

CHAPTER 5 SUMMARY AND RECOMMENDATIONS

This dissertation presents new experimental results about both crystalline metals and amorphous metals as membranes for hydrogen separations. Specifically reported are relationships between metallic membrane properties and hydrogen separation performance.

Chapter 2 discusses the results of the bench-mark Pd_7Ag_{23} membranes. Crystalline membranes, Pd_7Ag_{23} membranes were investigated for the relationship between surface composition and hydrogen transport properties. Chapters 3 and 4 discuss the results of amorphous metallic membranes. Chapter 3 focuses on a series of three binary Cu-Zr amorphous metallic membranes. Chapter four focuses on, $Ni_{60}Nb_{35}X_5$ (X=Sn, Ti and Zr) ternary alloys.

Chapter 2 shows that the custom-built bench scale hydrogen permeation system can successfully collect the hydrogen permeability of free standing metallic membranes. Various heat treatments created different surface compositions in commercial $Pd_{77}Ag_{23}$ membranes – either causing Pd segregation to or away from the membrane surface. Subsequently, the hydrogen permeation of these membranes was measured. A strong correlation between the surface composition of the $Pd_{77}Ag_{23}$ membranes and the hydrogen permeation was found. This is a novel result about $Pd_{77}Ag_{23}$ metallic membranes.

Chapters 3 and 4 discuss the results of different amorphous alloys for hydrogen permeation. These amorphous systems, Cu-Zr and $Ni_{60}Nb_{35}X_5$ (X=Sn, Ti and Zr), were selected for either potential high hydrogen permeability or good thermal stability. All of

the studied compositions were successfully synthesized into amorphous metallic membranes by splat quenching.

Chapter 3 discusses Cu-Zr amorphous metallic membranes. Previous Monte Carlo simulations had predicted that the Cu-Zr system would have excellent hydrogen permeability. However, the experimentally measured Cu-Zr hydrogen permeability was not as high as predicted by the simulations. The lower experimentally observed permeation was the result of surface oxides forming on the amorphous membranes. Additionally, the thermal stability of amorphous Cu-Zr could not satisfy the operation conditions of hydrogen separation. After approximately two hours of hydrogen permeation testing at 300 °C the Cu-Zr alloys began to crystallize

Chapter 4 discusses the $Ni_{60}Nb_{35}X_5$ (X=Sn, Ti and Zr) amorphous metallic membrane system. These alloys exhibit significantly better thermal stability than the amorphous Cu-Zr membranes and also have better hydrogen permeability. However, the pure hydrogen permeability is still not comparable to $Pd_{77}Ag_{23}$ crystalline membranes. Also the mechanical properties change induced by hydrogen is also discussed for the ternary amorphous metallic membranes. It has been found that the substitution of different element, even with very low concentration, has different impact on the mechanic properties.

Based on the work that has been done, three recommendations are provided. These recommendations are summarized below.

The first recommendation is to study the surface elemental change incurred by hydrogen in alloy membranes (both crystalline and amorphous). The segregation

phenomena observed in the Pd_7Ag_{23} membranes reported in this thesis may help promote the hydrogen dissociation on the membrane surface.

The second recommendation is to investigate on the amorphous alloys which have broader super cooled liquid region (SCLR). The wider the SCLR, more the alloy will resist crystallization during a hydrogen permeation process. Examples of possible amorphous metallic forming alloys that have both high glass transition temperatures and larger SCLRs are the ZrAlNi and ZrAlCu amorphous metallic forming systems. Those compositions with large SCLR indicate better thermal stability upon operation.

The third recommendation is to relax (anneal) the amorphous structures to different energetic states. By changing the structure into different thermal state, there may be different hydrogen transport properties. This will shed light upon the relationship between the structure of amorphous alloys and the interaction with hydrogen.

REFERENCES

FACTSage Thermochemical Software and Databases [Internet]. Montreal, Quebec, Canada: Thermfact (Center for Research in computational Thermochemistry).

Abate S, Genovese C, Perathoner S, Centi G. 2009. *Performances and stability of a Pd-based supported thin film membrane prepared by EPD with a novel seeding procedure. Part 1-Behaviour in H-2:N-2 mixtures*. Catalysis Today 145(1-2):63-71.

Acha E, Requies J, Barrio VL, Cambra JF, Guemez MB, Arias PL, van Delft YC. 2012. *PdCu membrane applied to hydrogen production from methane*. Journal of Membrane Science 415:66-74.

Adibhatla A, Dolan MD, Chien W, Chandra D. 2014. *Enhancing the catalytic activity of Ni-based amorphous alloy membrane surfaces*. Journal of Membrane Science 463:190-195.

Aggarwal S, Monga AP, Perusse SR, Ramesh R, Ballarotto V, Williams ED, Chalamala BR, Wei Y, Reuss RH. 2000. *Spontaneous Ordering of Oxide Nanostructures*. Science 287(5461):2235-2237.

Al-Mufachi NA, Rees NV, Steinberger-Wilkens R. 2015. *Hydrogen selective membranes: A review of palladium-based dense metal membranes*. Renewable and Sustainable Energy Reviews 47:540-551.

Alashab STS, Harris IR. 1988. *HYDROGEN SOLUBILITY AND THE EQUILIBRIUM PRESSURE COMPOSITION ISOTHERM FOR PD-EU ALLOYS*. International Journal of Hydrogen Energy 13(3):191-194.

Alcock CB, Itkin VP, Horrigan MK. 1984. *Vapour Pressure Equations for the Metallic Elements: 298–2500K*. Canadian Metallurgical Quarterly 23(3):309-313.

Amandusson H, Ekedahl LG, Dannetun H. 2001. *Hydrogen permeation through surface modified Pd and PdAg membranes*. Journal of Membrane Science 193(1):35-47.

Antler M. 1982. *The application of palladium in electronic connectors*. Platinum metals review 26:106.

Argon AS. 1979. *Plastic deformation in metallic glasses*. Acta Metallurgica 27(1):47-58.

Argon AS, Kuo HY. 1979. *Plastic flow in a disordered bubble raft (an analog of a metallic glass)*. Materials Science and Engineering 39(1):101-109.

Assal J, Hallstedt B, Gauckler LJ. 1997. *Thermodynamic assessment of the silver-oxygen system*. Journal of the American Ceramic Society 80(12):3054-3060.

Ayturk ME, Kazantzis NK, Ma YH. 2009. *Modeling and performance assessment of Pd- and Pd/Au-based catalytic membrane reactors for hydrogen production*. Energy & Environmental Science 2(4):430-438.

Baerlocher C, Mccusker LB. Database of Zeolite Structures [Internet]. Available from: http://www.iza-structure.org/databases/

Baker RW. 2004. Membrane Technology and Applications. Menlo Park, CA, USA: John Wiley & Sons.

Barelli L, Bidini G, Gallorini F, Servili S. 2008. *Hydrogen production through sorption-enhanced steam methane reforming and membrane technology: A review*. Energy 33(4):554-570.

Basile A. 2008. *Hydrogen Production Using Pd-based Membrane Reactors for Fuel Cells*. Topics in Catalysis 51(1-4):107-122.

Bhave RR. 1991. Inorganic membranes synthesis, characteristics and applications. New York, USA: Van Nostrand Reinhold.

Bielmann M, Schwaller P, Ruffieux P, Gröning O, Schlapbach L, Gröning P. 2002. *AgO investigated by photoelectron spectroscopy:Evidence for mixed valence*. Physical Review B 65(23):235431.

Boon J, Pieterse JAZ, Dijkstra JW, Annaland MV. 2012. *Modelling and systematic experimental investigation of mass transfer in supported palladium-based membrane separators*. International Journal of Greenhouse Gas Control 11:S122-S129.

Braun F, Tarditi AM, Miller JB, Cornaglia LM. 2014. *Pd-based binary and ternary alloy membranes: Morphological and perm-selective characterization in the presence of H2S*. Journal of Membrane Science 450:299-307.

Cao QP, Ma Y, Wang C, Wang XD, Jiang JZ. 2014. *Effect of temperature and strain rate on deformation behavior in metallic glassy films*. Thin Solid Films 561:60-69.

Cha P-R, Kim J-Y, Seok H-K, Mm YC. 2008. *Ab-initio study of hydrogen permeation though palladium membrane*. Journal of the Korean Institute of Metals and Materials 46(5):296-303.

Chandrasekhar N, Sholl DS. 2014. *Quantitative computational screening of Pd-based intermetallic membranes for hydrogen separation*. Journal of Membrane Science 453:516-524.

Chemical Rubber C. CRC handbook of chemistry and physics: a ready-reference book of chemical and physical data. (Journal, Electronic).

Chen HS. 1974. *THERMODYNAMIC CONSIDERATIONS ON FORMATION AND STABILITY OF METALLIC GLASSES*. Acta Metallurgica 22(12):1505-1511.

Chi Y-H, Yen P-S, Jeng M-S, Ko S-T, Lee T-C. 2010. *Preparation of thin Pd membrane on porous stainless steel tubes modified by a two-step method*. International Journal of Hydrogen Energy 35(12):6303-6310.

Choi-Yim H, Xu D, Johnson WL. 2003. *Ni-based bulk metallic glass formation in the Ni–Nb–Sn and Ni–Nb–Sn–X(X=B,Fe,Cu) alloy systems*. Applied Physics Letters 82(7):1030-1032.

Choi-Yim H, Xu DH, Lind ML, Loffler JF, Johnson WL. 2006. *Structure and mechanical properties of bulk glass-forming Ni-Nb-Sn alloys*. Scripta Materialia 54(2):187-190.

Deng X, Koopman M, Chawla N, Chawla KK. 2004. *Young's modulus of (Cu, Ag)-Sn intermetallics measured by nanoindentation*. Materials Science and Engineering a-Structural Materials Properties Microstructure and Processing 364(1-2):240-243.

Ding HY, Zhang W, Yamaura SI, Yao KF. 2013. *Hydrogen Permeable Nb-Based Amorphous Alloys with High Thermal Stability*. Materials Transactions 54(8):1330-1334.

Dini K, Dunlap RA. 1985. *CRYSTALLIZATION AND HYDROGEN ABSORPTION IN AMORPHOUS CU60ZR40 AND CU50ZR50*. Journal of Physics F-Metal Physics 15(2):273-277.

DOE. Hydrogen Production [Internet]. Available from: http://energy.gov/eere/fuelcells/natural-gas-reforming

Dolan M, Dave N, Morpeth L, Donelson R, Liang D, Kellam M, Song S. 2009a. *Ni-based amorphous alloy membranes for hydrogen separation at 400 degrees C*. Journal of Membrane Science 326(2):549-555.

Dolan MD. 2010. *Non-Pd BCC alloy membranes for industrial hydrogen separation*. Journal of Membrane Science 362(1-2):12-28.

Dolan MD, Dave NC, Ilyushechkin AY, Morpeth LD, McLennan KG. 2006. *Composition and operation of hydrogen-selective amorphous alloy membranes*. Journal of Membrane Science 285(1-2):30-55.

Dolan MD, Hara S, Dave NC, Haraya K, Ishitsuka M, Ilyushechkin AY, Kita K, McLennan KG, Morpeth LD, Mukaida M. 2009b. *Thermal stability, glass-forming ability and hydrogen permeability of amorphous Ni64Zr36-XMX (M = Ti, Nb, Mo, Hf, Ta or W) membranes*. Separation and Purification Technology 65(3):298-304.

Dong J, Lin YS, Kanezashi M, Tang Z. 2008. *Microporous inorganic membranes for high temperature hydrogen purification*. Journal of Applied Physics 104(12):121301.

Dudek MA, Chawla N. 2010. *Nanoindentation of rare earth-Sn intermetallics in Pb-free solders*. Intermetallics 18(5):1016-1020.

Eddaoudi M, Kim J, Rosi N, Vodak D, Wachter J, O'Keeffe M, Yaghi OM. 2002. *Systematic design of pore size and functionality in isoreticular MOFs and their application in methane storage*. Science 295(5554):469-472.

Eliaz N, Eliezer D. 1999. *An Overview of Hydrogen Interaction with Amorphous Alloys*. Advanced Performance Materials 6(1):5-31.

Eliaz N, Fuks D, Eliezer D. 1999. *A new model for the diffusion behavior of hydrogen in metallic glasses*. Acta Materialia 47(10):2981-2989.

Fischer-Cripps, C. A. 2004. Nanoindentation. Springer-Verlag New York.

Flores KM, Suh D, Dauskardt RH, Asoka-Kumar P, Sterne PA, Howell RH. 2002. *Characterization of free volume in a bulk metallic glass using positron annihilation spectroscopy*. Journal of Materials Research 17(5):1153-1161.

Gabasch H, Unterberger W, Hayek K, Klotzer B, Kleimenov E, Teschner D, Zafeiratos S, Havecker M, Knop-Gericke A, Schlogl R et al. . 2006. *In situ XPS study of Pd(111) oxidation at elevated pressure, Part 2: Palladium oxidation in the 10(-1) mbar range*. Surface Science 600(15):2980-2989.

Gade SK, Coulter KE, Way JD. 2010. *Effects of fabrication technique upon material properties and permeation characteristics of palladium-gold alloy membranes for hydrogen separations*. Gold Bulletin 43(4):287-297.

Galipaud J, Martin MH, Roue L, Guay D. 2013. *Measurement of Hydrogen Solubility in PdxCu100-x Thin Films Prepared by Pulsed Laser Deposition: An Electrochemical in Situ X-Ray Diffraction Analysis*. Journal of Physical Chemistry C 117(6):2688-2698.

Ge L, Hui X, Wang ER, Chen GL, Arroyave R, Liu ZK. 2008. *Prediction of the glass forming ability in Cu-Zr binary and Cu-Zr-Ti ternary alloys*. Intermetallics 16(1):27-33.

Ge L, Hui XD, Chen GL, Liu ZK. 2007. *Prediction of the glass-forming ability of Cu-Zr binary alloys*. Acta Physico-Chimica Sinica 23(6):895-899.

Gebert A, Buchholz K, Leonhard A, Mummert K, Eckert J, Schultz L. 1999. *Investigations on the electrochemical behaviour of Zr-based bulk metallic glasses*. Materials Science and Engineering: A 267(2):294-300.

Gebert A, Gostin PF, Schultz L. 2010. *Effect of surface finishing of a Zr-based bulk metallic glass on its corrosion behaviour*. Corrosion Science 52(5):1711-1720.

Griessen R, Driessen A. 1984. *Heat of formation and band structure of binary and ternary metal hydrides*. Physical Review B 30(8):4372-4381.

Guerreiro BH, Martin MH, Roue L, Guay D. 2014. *Hydrogen solubility in PdCuAu alloy thin films prepared by electrodeposition*. International Journal of Hydrogen Energy 39(7):3487-3497.

H. Strathmann, L. Giorno, Drioli E. 2006. Introduction to Membrane Science and Technology.

Hao S, Sholl DS. 2011a. *Computational prediction of durable amorphous metal membranes for H-2 purification*. Journal of Membrane Science 381(1-2):192-196.

Hao SQ, Sholl DS. 2011b. *Computational prediction of durable amorphous metal membranes for H-2 purification*. Journal of Membrane Science 381(1-2):192-196.

Hara S, Sakaki K, Itoh N, Kimura HM, Asami K, Inoue A. 2000. *An amorphous alloy membrane without noble metals for gaseous hydrogen separation*. Journal of Membrane Science 164(1-2):289-294.

Harris IR, Norman M. 1968. *The electronic state of cerium in some palladium alloys*. Journal of the Less Common Metals 15(3):285-298.

Harris JH, Curtin WA, Tenhover MA. 1987. *UNIVERSAL FEATURES OF HYDROGEN ABSORPTION IN AMORPHOUS TRANSITION-METAL ALLOYS*. Physical Review B 36(11):5784-5797.

Hay J, Agee P, Herbert E. 2010. *CONTINUOUS STIFFNESS MEASUREMENT DURING INSTRUMENTED INDENTATION TESTING*. Experimental Techniques 34(3):86-94.

Henke BL, Gullikson EM, Davis JC. 1993. *X-Ray Interactions: Photoabsorption, Scattering, Transmission, and Reflection at E = 50-30,000 eV, Z = 1-92*. Atomic Data and Nuclear Data Tables 54(2):181-342.

Hickman JW, Gulbransen EA. 1948. *OXIDE FILMS FORMED ON TITANIUM, ZIRCONIUM, AND THEIR ALLOYS WITH NICKEL, COPPER, AND COBALT*. Analytical Chemistry 20(2):158-165.

Ho WSW, Sirkar KK. 1992. Membrane Handbook. New York, USA: Van Nostrand Reinhold.

Huang Y, Dittmeyer R. 2007. *Preparation of thin palladium membranes on a porous support with rough surface*. Journal of Membrane Science 302(1-2):160-170.

Hyman MP, Loveless BT, Medlin JW. 2007. *A density functional theory study of H2S decomposition on the (111) surfaces of model Pd-alloys*. Surface Science 601(23):5382-5393.

Ihsan Barin I. 1989. Thermochemical Data of Pure Substances. VCH, Weinheim, Germany.

Il Jeon S, Park JH, Magnone E, Lee YT, Fleury E. 2012. *Hydrogen permeation of Pd-coated V90Al10 alloy membranes at different pressures in the presence and absence of carbon dioxide*. Current Applied Physics 12(2):394-400.

Imai Y, Tsunoda T, Kobayashi K, Watanabe A. 2006. *Preparation of palladium film by coating photolysis process using KrF or ArF excimer laser*. Applied Surface Science 252(8):2858-2866.

Inoue A. 2000. *Stabilization of metallic supercooled liquid and bulk amorphous alloys*. Acta Materialia 48(1):279-306.

Ishikawa K, Tokui S, Aoki K. 2009. *Microstructure and hydrogen permeation of cold rolled and annealed Nb40Ti30Ni60 alloy*. Intermetallics 17(3):109-114.

Islam MA, Ilias S. 2010. *Characterization of Pd-Composite Membrane Fabricated by Surfactant Induced Electroless Plating (SIEP): Effect of Grain Size on Hydrogen Permeability*. Separation Science and Technology 45(12-13):1886-1893.

Jang JSC, Koch CC. 1989. *The glass transition temperature in amorphous CU1−xZrx alloys synthesized by mechanical alloying/milling*. Scripta Metallurgica 23(10):1805-1810.

Jayaraman V, Lin YS, Pakala M, Lin RY. 1995. *FABRICATION OF ULTRATHIN METALLIC MEMBRANES ON CERAMIC SUPPORTS BY SPUTTER-DEPOSITION*. Journal of Membrane Science 99(1):89-100.

Johnson WL. 2002a. *Bulk amorphous metal—An emerging engineering material*. JOM 54(3):40-43.

Johnson WL. 2002b. *Bulk amorphous metal - An emerging engineering material*. Jom-Journal of the Minerals Metals & Materials Society 54(3):40-43.

Jones CW, Koros WJ. 1994. *Carbon molecular sieve gas separation membranes-I. Preparation and characterization based on polyimide precursors*. Carbon 32(8):1419-1425.

Joshi BM, Gandhi HS, Shelef M. 1986. *Surface enrichment of rhodium in Pd-Rh alloys after high temperature air oxidation*. Surface and Coatings Technology 29(2):131-140.

Kerry F. 2007. Industrial Gas Handbook: Gas Separation and Purification. CRC Press.

Kesting RE, Fritzsche AK. 1993. Polymeric Gas Separation Membranes. Wiley.

Kim KH, Park HC, Lee J, Cho E, Lee SM. 2013. *Vanadium alloy membranes for high hydrogen permeability and suppressed hydrogen embrittlement*. Scripta Materialia 68(11):905-908.

Kim S-M, Chandra D, Pal NK, Dolan MD, Chien W-M, Talekar A, Lamb J, Paglieri SN, Flanagan TB. 2012. *Hydrogen permeability and crystallization kinetics in amorphous Ni-Nb-Zr alloys*. International Journal of Hydrogen Energy 37(4):3904-3913.

Kiyono M, Williams PJ, Koros WJ. 2010. *Effect of pyrolysis atmosphere on separation performance of carbon molecular sieve membranes*. Journal of Membrane Science 359(1–2):2-10.

Klement W, Willens RH, Duwez POL. 1960. *Non-crystalline Structure in Solidified Gold-Silicon Alloys*. Nature 187(4740):869-870.

Krisyuk VV, Shubin YV, Senocq F, Turgambaeva AE, Duguet T, Igumenov IK, Vahlas C. 2015. *Chemical vapor deposition of Pd/Cu alloy films from a new single source precursor*. Journal of Crystal Growth 414:130-134.

Lai T, Lind ML. 2015. *Heat treatment driven surface segregation in Pd77Ag23 membranes and the effect on hydrogen permeability*. International Journal of Hydrogen Energy 40(1):373-382.

Lai T, Yin H, Lind ML. 2015. *The hydrogen permeability of Cu–Zr binary amorphous metallic membranes and the importance of thermal stability*. Journal of Membrane Science 489(0):264-269.

Le Treut H, Someville R, Cubasch U, Ding Y, Mauritzen C, Mokssit A, Peterson T, Prather M. 2007. Historical Overview of Climate Change. In: Solomon S, Qin D, Manning M, Chen Z, Marquis M, Averyt KB, Tignor M, Miller HL, editors. Climate Change 2007: The Physical Science Basis. Contribution of Working Group I to the Forth Assessment Report of the Intergovernmental Panel on Climate Change. Cambridge, United Kingdom and New York, NY, USA: Cambridge University Press.

Lee B-M, Lee B-J. 2014. *A Comparative Study on Hydrogen Diffusion in Amorphous and Crystalline Metals Using a Molecular Dynamics Simulation*. Metallurgical and Materials Transactions a-Physical Metallurgy and Materials Science 45A(6):2906-2915.

Lee B-M, Shim J-H, Suh J-Y, Lee B-J. 2014. *A semi-empirical methodology to predict hydrogen permeability in amorphous alloy membranes*. Journal of Membrane Science 472:102-109.

Lee J, Farha OK, Roberts J, Scheidt KA, Nguyen ST, Hupp JT. 2009. *Metal-organic framework materials as catalysts*. Chemical Society Reviews 38(5):1450-1459.

Lewis FA. 1995. *THE PALLADIUM HYDROGEN SYSTEM - STRUCTURES NEAR PHASE-TRANSITION AND CRITICAL-POINTS*. International Journal of Hydrogen Energy 20(7):587-592.

Li J-R, Kuppler RJ, Zhou H-C. 2009. *Selective gas adsorption and separation in metal-organic frameworks*. Chemical Society Reviews 38(5):1477-1504.

Li X, Liu D, Chen R, Yan E, Liang X, Rettenmayr M, Su Y, Guo J, Fu H. 2015. *Changes in microstructure, ductility and hydrogen permeability of Nb-(Ti, Hf)Ni alloy membranes by the substitution of Ti by Hf*. Journal of Membrane Science 484:47-56.

Liaw D-J, Wang K-L, Huang Y-C, Lee K-R, Lai J-Y, Ha C-S. 2012. *Advanced polyimide materials: Syntheses, physical properties and applications*. Progress in Polymer Science 37(7):907-974.

Libowitz GG, Maeland AJ. 1984. *Interactions of hydrogen with metallic glass alloys*. Journal of the Less Common Metals 101:131-143.

Lind ML, Duan G, Johnson WL. 2006. *Isoconfigurational Elastic Constants and Liquid Fragility of a Bulk Metallic Glass Forming Alloy*. Physical Review Letters 97(1):015501.

Ling C, Semidey-Flecha L, Sholl DS. 2011. *First-principles screening of PdCuAg ternary alloys as H-2 purification membranes*. Journal of Membrane Science 371(1-2):189-196.

Ling C, Sholl DS. 2007. *Using first-principles calculations to predict surface resistances to H-2 transport through metal alloy membranes*. Journal of Membrane Science 303(1-2):162-172.

Lovallo MC, Gouzinis A, Tsapatsis M. 1998. *Synthesis and characterization of oriented MFI membranes prepared by secondary growth*. Aiche Journal 44(8):1903-1913.

Lovvik OM, Opalka SM. 2008. *Reversed surface segregation in palladium-silver alloys due to hydrogen adsorption*. Surface Science 602(17):2840-2844.

Lovvik OM, Peters TA, Bredesen R. 2014. *First-principles calculations on sulfur interacting with ternary Pd-Ag-transition metal alloy membrane alloys*. Journal of Membrane Science 453:525-531.

Lu ZP, Li Y, Ng SC. 2000. *Reduced glass transition temperature and glass forming ability of bulk glass forming alloys*. Journal of Non-Crystalline Solids 270(1–3):103-114.

Mardilovich PP, She Y, Ma YH, Rei M-H. 1998. *Defect-free palladium membranes on porous stainless-steel support*. Aiche Journal 44(2):310-322.

Masuda T, Fukumoto N, Kitamura M, Mukai SR, Hashimoto K, Tanaka T, Funabiki T. 2001. *Modification of pore size of MFI-type zeolite by catalytic cracking of silane and application to preparation of H2-separating zeolite membrane*. Microporous and Mesoporous Materials 48(1–3):239-245.

Mejdell AL, Chen D, Peters TA, Bredesen R, Venvik HJ. 2010. *The effect of heat treatment in air on CO inhibition of a similar to 3 mu m Pd-Ag (23 wt.%) membrane*. Journal of Membrane Science 350(1-2):371-377.

Mejdell AL, Klette H, Ramachandran A, Borg A, Bredesen R. 2008. *Hydrogen permeation of thin, free-standing Pd/Ag23% membranes before and after heat treatment in air*. Journal of Membrane Science 307(1):96-104.

Michalkiewicz B, Koren ZC. 2015. *Zeolite membranes for hydrogen production from natural gas: state of the art*. Journal of Porous Materials 22(3):635-646.

Morreale BD, Ciocco MV, Howard BH, Killmeyer RP, Cugini A, Enick RM. 2004. *Effect of hydrogen-sulfide on the hydrogen permeance of palladium-copper alloys at elevated temperatures*. Journal of Membrane Science 241(2):219-224.

Mueller WM, Blackledge JP, Libowitz GG. 2013. Metal hydrides. Elsevier.

Murali P, Ramamurty U. 2005. *Embrittlement of a bulk metallic glass due to sub-T-g annealing*. Acta Materialia 53(5):1467-1478.

Musket RG. 1976. *Effects of contamination on the interaction of hydrogen gas with palladium: A review*. Journal of the Less Common Metals 45(2):173-183.

Nagase T, Ueda M, Umakoshi Y. 2009. *Preparation of Ni–Nb-based metallic glass wires by arc-melt-type melt-extraction method*. Journal of Alloys and Compounds 485(1-2):304-312.

Naito S, Yamamoto M, Doi M, Kimura M. 1998. *High-temperature diffusion of hydrogen and deuterium in titanium and Ti3Al*. Journal of the Electrochemical Society 145(7):2471-2475.

Nakamura Y, Yukawa H, Suzuki A, Nambu T, Matsumoto Y, Murata Y. 2015. *Alloying effects on hydrogen permeability of V without catalytic Pd overlayer*. Journal of Alloys and Compounds 645:S275-S279.

Nambu T, Shimizu K, Matsumoto Y, Rong R, Watanabe N, Yukawa H, Morinaga M, Yasuda I. 2007. *Enhanced hydrogen embrittlement of Pd-coated niobium metal membrane detected by in situ small punch test under hydrogen permeation*. Journal of Alloys and Compounds 446:588-592.

Nenoff TM, Spontak RJ, Aberg CM. 2006. *Membranes for hydrogen purification: An important step toward a hydrogen-based economy*. Mrs Bulletin 31(10):735-741.

Nishimura C, Komaki M, Hwang S, Amano M. 2002. *V–Ni alloy membranes for hydrogen purification*. Journal of Alloys and Compounds 330–332:902-906.

Nyholm R, Mårtensson N. 1981. *Experimental core-hole ground state energies for the elements 41Nb to 52Te*. Solid State Communications 40(3):311-314.

Ockwig NW, Nenoff TM. 2007. *Membranes for hydrogen separation*. Chemical Reviews 107(10):4078-4110.

Ojovan MI. 2008. *Viscosity and Glass Transition in Amorphous Oxides*. Advances in Condensed Matter Physics 2008:23.

Oliver WC, Pharr GM. 1992. *AN IMPROVED TECHNIQUE FOR DETERMINING HARDNESS AND ELASTIC-MODULUS USING LOAD AND DISPLACEMENT SENSING INDENTATION EXPERIMENTS*. Journal of Materials Research 7(6):1564-1583.

Oliver WC, Pharr GM. 2004. *Measurement of hardness and elastic modulus by instrumented indentation: Advances in understanding and refinements to methodology*. Journal of Materials Research 19(1):3-20.

Opalka SM, Løvvik OM, Emerson SC, She Y, Vanderspurt TH. 2011. *Electronic origins for sulfur interactions with palladium alloys for hydrogen-selective membranes*. Journal of Membrane Science 375(1–2):96-103.

Ouyang C, Lee Y-S. 2011. *Hydrogen-induced interactions in vanadium from first-principles calculations*. Physical Review B 83(4).

Ozaki T, Zhang Y, Komaki M, Nishimura C. 2003. *Hydrogen permeation characteristics of V–Ni–Al alloys*. International Journal of Hydrogen Energy 28(11):1229-1235.

Paglieri SN, Pal NK, Dolan MD, Kim S-M, Chien W-M, Lamb J, Chandra D, Hubbard KM, Moore DP. 2011a. *Hydrogen permeability, thermal stability and hydrogen embrittlement of Ni–Nb–Zr and Ni–Nb–Ta–Zr amorphous alloy membranes*. Journal of Membrane Science 378(1-2):42-50.

Paglieri SN, Pal NK, Kim SM, Dolan MD, Chien WM, Lamb J, Talekar A, Chandra D. 2011b. *Ni-Nb-Zr-(Ta, Co) amorphous alloy membranes for hydrogen separation*. Abstracts of Papers of the American Chemical Society 242.

Paglieri SN, Way JD. 2002. *Innovations in palladium membrane research*. Separation and Purification Methods 31(1):1-169.

Park ES, Na JH, Kim DH. 2010. *Abnormal behavior of supercooled liquid region in bulk-forming metallic glasses*. Journal of Applied Physics 108(5):-.

Park K-W, Ahn J-P, Seok H-K, Kim Y-C. 2011. *Relationship between activation energy for hydrogen permeation and hydrogen permeation properties of amorphous Cu50Zr50 and Cu65Zr35 membranes*. Intermetallics 19(12):1887-1890.

Parsley D, Ciora Jr RJ, Flowers DL, Laukaitaus J, Chen A, Liu PKT, Yu J, Sahimi M, Bonsu A, Tsotsis TT. 2014. *Field evaluation of carbon molecular sieve membranes for the separation and purification of hydrogen from coal- and biomass-derived syngas*. Journal of Membrane Science 450:81-92.

Paul DR, Yampol'skii YP. 1994. Polymeric Gas Separation Membranes. CRC Press, Inc.

Peker A. 1994. Formation and characterization of bulk metallic glasses. California Institute of Technology.

Peker A, Johnson WL. 1993. *A HIGHLY PROCESSABLE METALLIC-GLASS - ZR41.2TI13.8CU12.5NI10.0BE22.5*. Applied Physics Letters 63(17):2342-2344.

Peters TA, Kaleta T, Stange M, Bredesen R. 2011a. *Development of thin binary and ternary Pd-based alloy membranes for use in hydrogen production*. Journal of Membrane Science 383(1-2):124-134.

Peters TA, Kaleta T, Stange M, Bredesen R. 2013. *Development of ternary Pd-Ag-TM alloy membranes with improved sulphur tolerance*. Journal of Membrane Science 429:448-458.

Peters TA, Stange M, Bredesen R. 2011b. *On the high pressure performance of thin supported Pd-23%Ag membranes-Evidence of ultrahigh hydrogen flux after air treatment*. Journal of Membrane Science 378(1-2):28-34.

Peters TA, Tucho WM, Ramachandran A, Stange M, Walmsley JC, Holmestad R, Borg A, Bredesen R. 2009. *Thin Pd-23%Ag/stainless steel composite membranes: Long-term stability, life-time estimation and post-process characterisation*. Journal of Membrane Science 326(2):572-581.

Phair JW, Donelson R. 2006. *Developments and Design of Novel (Non-Palladium-Based) Metal Membranes for Hydrogen Separation*. Industrial & Engineering Chemistry Research 45(16):5657-5674.

Porter DAEKESMY. 2009. Crystal interfaces and microstructure. Phase transformations in metals and alloys. Boca Raton, FL: CRC Press. p. 147-148.

Puls MP, Shi SQ, Rabier J. 2005. *Experimental studies of mechanical properties of solid zirconium hydrides*. Journal of Nuclear Materials 336(1):73-80.

Qiang JB, Zhang W, Inoue A. 2007. *Formation and thermal stability of Ni-based bulk metallic glasses in Ni-Zr-Nb-Al system*. Materials Transactions 48(9):2385-2389.

Qiang JB, Zhang W, Yamaura S, Inoue A. 2009. *Thermal Stability and Hydrogen Permeation of Ni42Zr30Nb28-xTax Amorphous Alloys*. Materials Transactions 50(6):1236-1239.

Ramachandran A, Tucho WM, Mejdell AL, Stange M, Venvik HJ, Walmsley JC, Holmestad R, Bredesen R, Borg A. 2010. *Surface characterization of Pd/Ag23 wt% membranes after different thermal treatments*. Applied Surface Science 256(20):6121-6132.

Ramamurty U, Jana S, Kawamura Y, Chattopadhyay K. 2005. *Hardness and plastic deformation in a bulk metallic glass*. Acta Materialia 53(3):705-717.

Rao JP, Ouyang CY, Lei MS, Jiang FY. 2012. *First principles investigation of interaction between interstitials H atom and Nb metal*. Acta Physica Sinica 61(4).

Rezac ME, Schöberl B. 1999. *Transport and thermal properties of poly(ether imide)/acetylene-terminated monomer blends*. Journal of Membrane Science 156(2):211-222.

Roa F, Way JD. 2005. *The effect of air exposure on palladium-copper composite membranes*. Applied Surface Science 240(1-4):85-104.

Robeson LM. 2008. *The upper bound revisited*. Journal of Membrane Science 320(1–2):390-400.

Roshan NR, Mishchenko AP, Polyakova VP, Parfenova NI, Savitsky EM, Voitekhova EA, Gryaznov VM, Sarylova ME. 1983. *The effect of the surface state on the hydrogen permeability and the catalytic activity of palladium alloy membranes*. Journal of the Less Common Metals 89(2):423-428.

Rosi NL, Eckert J, Eddaoudi M, Vodak DT, Kim J, O'Keeffe M, Yaghi OM. 2003. *Hydrogen storage in microporous metal-organic frameworks*. Science 300(5622):1127-1129.

Ryi SK, Xu N, Li AW, Lim CJ, Grace JR. 2010. *Electroless Pd membrane deposition on alumina modified porous Hastelloy substrate with EDTA-free bath*. International Journal of Hydrogen Energy 35(6):2328-2335.

Schroers J. 2010. *Processing of Bulk Metallic Glass*. Advanced Materials 22(14):1566-1597.

Schuh CA, Hufnagel TC, Ramamurty U. 2007. *Overview No.144 - Mechanical behavior of amorphous alloys*. Acta Materialia 55(12):4067-4109.

Schulz R, Samwer K, Johnson WL. 1984. *Kinetics of phase separation in Cu50Zr50 metallic glasses*. Journal of Non-Crystalline Solids 61–62, Part 2(0):997-1002.

Seah MP. 1990. Quantification of AES and XPS. In: Briggs D, Seah MP, editors. Practical Surface Analysis. JOHN WILEY & SONS.

Sen P, Sarma DD, Budham RC, Chopra KL, Rao CNR. 1984. *An electron spectroscopic study of the surface oxidation of glassy and crystalline Cu-Zr alloys*. Journal of Physics F: Metal Physics 14(2):565.

Shirley DA. 1972. *High-Resolution X-Ray Photoemission Spectrum of the Valence Bands of Gold*. Physical Review B 5(12):4709-4714.

Shu J, Bongondo BEW, Grandjean BPA, Adnot A, Kaliaguine S. 1993. *Surface segregation of Pd ・ Ag membranes upon hydrogen permeation*. Surface Science 291(1 – 2):129-138.

Sie SH. 2003. Rutherford Backscattering Spectrometry and Nuclear Reaction Analysis. In: O'Connor DJ, Sexton BA, Smart RSC, editors. Surface Analysis Methods in Materials Science. Verlag Berlin Heidelberg New York: Springer. p. P229-P231.

Singh SS, Schwartzstein C, Williams JJ, Xiao X, De Carlo F, Chawla N. 2014. *3D microstructural characterization and mechanical properties of constituent particles in Al 7075 alloys using X-ray synchrotron tomography and nanoindentation*. Journal of Alloys and Compounds 602:163-174.

Somorjai GA. 1994. Dynamics at surfaces. Introduction to surface chemistry and catalysis. Chichester, UK WILEY. p. 345.

Spaepen F. 1977. *A microscopic mechanism for steady state inhomogeneous flow in metallic glasses*. Acta Metallurgica 25(4):407-415.

Steif PS, Spaepen F, Hutchinson JW. 1982. *Strain localization in amorphous metals*. Acta Metallurgica 30(2):447-455.

Suh D, Dauskardt RH. 2000. *Hydrogen effects on the mechanical and fracture behavior of a Zr-Ti-Ni-Cu-Be bulk metallic glass*. Scripta Materialia 42(3):233-240.

Suwarno S, Gosselin Y, Solberg JK, Maehlen JP, Williams M, Krogh B, Borresen BT, Rytter E, Ochoa-Fernandez E, Yartys VA. 2012. *Selective hydrogen absorption from gaseous mixtures by BCC Ti-V alloys*. International Journal of Hydrogen Energy 37(5):4127-4138.

Svenum IH, Herron JA, Mavrikakis M, Venvik HJ. 2012. *Adsorbate-induced segregation in a PdAg membrane model system: Pd3Ag(111)*. Catalysis Today 193(1):111-119.

Tanaka K, Islam MN, Kido M, Kita H, Okamoto K-i. 2006. *Gas permeation and separation properties of sulfonated polyimide membranes*. Polymer 47(12):4370-4377.

Tang HX, Ishikawa K, Aoki K. 2008. *Effect of elements addition on hydrogen permeability and ductility of Nb40Ti18Zr12Ni30 alloy*. Journal of Alloys and Compounds 461(1-2):263-266.

Tarditi AM, Bosko ML, Cornaglia LM. 2012. *Alloying and surface composition of model Pd-Ag films synthesized by electroless deposition*. International Journal of Hydrogen Energy 37(7):6020-6029.

Tarditi AM, Imhoff C, Braun F, Miller JB, Gellman AJ, Cornaglia L. 2015a. *PdCuAu ternary alloy membranes: Hydrogen permeation properties in the presence of H2S*. Journal of Membrane Science 479:246-255.

Tarditi AM, Imhoff C, Miller JB, Cornaglia L. 2015b. *Surface composition of PdCuAu ternary alloys: a combined LEIS and XPS study*. Surface and Interface Analysis 47(7):745-754.

Tong JH, Suda H, Haraya K, Matsumura Y. 2005. *A novel method for the preparation of thin dense Pd membrane on macroporous stainless steel tube filter*. Journal of Membrane Science 260(1-2):10-18.

Tosques J, Martin MH, Roue L, Guay D. 2014. *Hydrogen solubility in PdCuAg ternary alloy films prepared by electrodeposition*. International Journal of Hydrogen Energy 39(28):15810-15818.

Tosti S. 2010. *Overview of Pd-based membranes for producing pure hydrogen and state of art at ENEA laboratories*. International Journal of Hydrogen Energy 35(22):12650-12659.

Tosti S, Borgognoni F, Rizzello C, Violante V. 2009. *Water gas shift reaction via Pd-based membranes*. Asia-Pacific Journal of Chemical Engineering 4(3):369-379.

Tucho WM, Venvik HJ, Stange M, Walmsley JC, Holmestad R, Bredesen R. 2009a. *Effects of thermal activation on hydrogen permeation properties of thin, self-supported Pd/Ag membranes*. Separation and Purification Technology 68(3):403-410.

Tucho WM, Venvik HJ, Walmsley JC, Stange M, Ramachandran A, Mathiesen RH, Borg A, Bredesen R, Holmestad R. 2009b. *Microstructural studies of self-supported (1.5-10 mu m) Pd/23 wt% Ag hydrogen separation membranes subjected to different heat treatments*. Journal of Materials Science 44(16):4429-4442.

Turnbull D, Cohen MH. 1961. *Free-Volume Model of the Amorphous Phase: Glass Transition*. The Journal of Chemical Physics 34(1):120.

Turner PS, Nockolds CE, Bulcock S. 2003. Electron microscope techniques for surface characterization. In: Connor DJ, Sexton BA, Smart RSC, editors. Surface analysis methods in materials science. 2nd ed.: Springer. p. 99.

Uemiya S. 1999. *State-of-the-Art of Supported Metal Membranes for Gas Separation*. Separation & Purification Reviews 28(1):51-85.

Vaidyanathan R, Dao M, Ravichandran G, Suresh S. 2001. *Study of mechanical deformation in bulk metallic glass through instrumented indentation*. Acta Materialia 49(18):3781-3789.

Vitos L, Ruban AV, Skriver HL, Kollár J. 1998. *The surface energy of metals*. Surface Science 411(1–2):186-202.

Volpe M, Inguanta R, Piazza S, Sunseri C. 2006. *Optimized bath for electroless deposition of palladium on amorphous alumina membranes*. Surface & Coatings Technology 200(20-21):5800-5806.

Wang Y-I, Suh J-Y, Lee Y-S, Shim J-H, Fleury E, Cho YW, Koh S-U. 2013. *Direct measurement of hydrogen diffusivity through Pd-coated Ni-based amorphous metallic membranes*. Journal of Membrane Science 436:195-201.

Ward TL, Dao T. 1999. *Model of hydrogen permeation behavior in palladium membranes*. Journal of Membrane Science 153(2):211-231.

Warner JS. 1967. *The Free Energy of Formation of Palladium Oxide*. Journal of the Electrochemical Society 114(1):68-71.

Watanabe N, Yukawa H, Nambu T, Matsumoto Y, Zhang G, Morinaga M. 2009a. *Mechanical Properties in Hydrogen Atmosphere and Hydrogen Permeability of Nb-W-Ta Alloys for Hydrogen Permeable Membrane*. Journal of the Japan Institute of Metals 73(9):742-746.

Watanabe N, Yukawa H, Nambu T, Matsumoto Y, Zhang GX, Morinaga M. 2009b. *Alloying effects of Ru and W on the resistance to hydrogen embrittlement and hydrogen permeability of niobium*. Journal of Alloys and Compounds 477(1-2):851-854.

Weaver JF, Hoflund GB. 1994. *Surface Characterization Study of the Thermal Decomposition of AgO*. The Journal of Physical Chemistry 98(34):8519-8524.

Wise MLH, Farr JPG, Harris IR. 1975. *X-ray studies of the α/β miscibility gaps of some palladium solid solution-hydrogen systems*. Journal of the Less Common Metals 41(1):115-127.

Wu L-Q, Xu N, Shi J. 2000. *Novel method for preparing palladium membranes by photocatalytic deposition*. Aiche Journal 46(5):1075-1083.

Xu DH, Duan G, Johnson WL. 2004a. *Unusual glass-forming ability of bulk amorphous alloys based on ordinary metal copper*. Physical Review Letters 92(24).

Xu DH, Lohwongwatana B, Duan G, Johnson WL, Garland C. 2004b. *Bulk metallic glass formation in binary Cu-rich alloy series - Cu100-xZrx (x=34, 36 38.2, 40 at.%) and mechanical properties of bulk Cu64Zr36 glass*. Acta Materialia 52(9):2621-2624.

Xu JJ, Cheung HY, Shi SQ. 2007. *Mechanical properties of titanium hydride*. Journal of Alloys and Compounds 436(1-2):82-85.

Yamaura S-i, Inoue A. 2010. *Effect of surface coating element on hydrogen permeability of melt-spun Ni40Nb20Ta5Zr30Co5 amorphous alloy*. Journal of Membrane Science 349(1-2):138-144.

Yamaura S-i, Sakurai M, Hasegawa M, Wakoh K, Shimpo Y, Nishida M, Kimura H, Matsubara E, Inoue A. 2005. *Hydrogen permeation and structural features of melt-spun Ni–Nb–Zr amorphous alloys*. Acta Materialia 53(13):3703-3711.

Yamaura SI, Nakata S, Kimura H, Inoue A. 2006. *Hydrogen permeation of Ni-Nb-Zr metallic glasses in a supercooled liquid state*. Materials Transactions 47(12):2991-2996.

Yan-Bin W, Northwood DO. 1987. *Calculation of the enthalpy of metal hydride formation*. Journal of the Less Common Metals 135(2):239-245.

Yang L, Zhang Z, Gao X, Guo Y, Wang B, Sakai O, Sakai H, Takahashi T. 2005. *Changes in hydrogen permeability and surface state of Pd–Ag/ceramic composite membranes after thermal treatment*. Journal of Membrane Science 252(1–2):145-154.

Yoo B-G, Oh J-H, Kim Y-J, Jang J-i. 2010. *Effect of hydrogen on subsurface deformation during indentation of a bulk metallic glass*. Intermetallics 18(10):1872-1875.

Yoshida H, Konishi S, Naruse Y. 1983. *Effects of impurities on hydrogen permeability through palladium alloy membranes at comparatively high pressures and temperatures*. Journal of the Less Common Metals 89(2):429-436.

Yukawa H, Zhang GX, Watanabe N, Morinaga M, Nambu T, Matsumoto Y. 2009. *Analysis of hydrogen diffusion coefficient during hydrogen permeation through niobium and its alloys*. Journal of Alloys and Compounds 476(1–2):102-106.

Zhang A, Chen D, Chen Z. 2009. *Bulk metallic glass-forming region of Cu-Zr binary and Cu-Zr based multicomponent alloy systems*. Journal of Alloys and Compounds 477(1-2):432-435.

Zhang K, Gade SK, Hatlevik O, Way JD. 2012a. *A sorption rate hypothesis for the increase in H-2 permeability of palladium-silver (Pd-Ag) membranes caused by air oxidation*. International Journal of Hydrogen Energy 37(1):583-593.

Zhang K, Gade SK, Way JD. 2012b. *Effects of heat treatment in air on hydrogen sorption over Pd-Ag and Pd-Au membrane surfaces*. Journal of Membrane Science 403:78-83.

Zhang W, Inoue A. 2002. *Effects of Ti on the thermal stability and glass-forming ability of Ni-Nb glassy alloy*. Materials Transactions 43(9):2342-2345.

Zhang W, Inoue A. 2003. *Formation and mechanical properties of Ni-based Ni-Nb-Ti-Hf bulk glassy alloys*. Scripta Materialia 48(5):641-645.

Zhao LF, Goldbach A, Bao C, Xu HY. 2014a. *Structural and Permeation Kinetic Correlations in PdCuAg Membranes*. Acs Applied Materials & Interfaces 6(24):22408-22416.

Zhao Y, Choi I-C, Seok M-Y, Kim M-H, Kim D-H, Ramamurty U, Suh J-Y, Jang J-i. 2014b. *Effect of hydrogen on the yielding behavior and shear transformation zone volume in metallic glass ribbons*. Acta Materialia 78:213-221.

Zhu ZW, Zhang HF, Sun WS, Hu ZQ. 2007. *Effect of Zr addition on the glass-forming ability and mechanical properties of Ni-Nb alloy*. Journal of Materials Research 22(2):453-459.

APPENDIX A

BASIC DEFINITIONS AND UNIT AND ERROR PROPAGATION

Experiment Parameters:

Temperature is 300 °C = 573 K

A= 153.2790124mm^2 Diameter of membrane is 1.397 cm= 13.97mm.

t= 0.025mm

a= 14.00 sccm

P_{H2}= 203.3kPa

c: hydrogen concentration various after calibration show different permeability

An example of error propagation with specific parameters is shown below

Error propagation

Formula:

$$\bar{P} = \frac{ac}{(100-c)\frac{\pi}{4}d^2}\, t\, \frac{1}{\sqrt{P_{H_2}} - \sqrt{cP_0}} \times 2.19228 \times 10^{-5}$$

$\bar{P}$: Permeability in mol/m s Pa$^{1/2}$

a: Flow rate of argon in sccm (standard cubic centimeter per minute)

c: Hydrogen composition detected by GC in %

d: Membrane permeation area diameter in mm

t: Membrane thickness in mm

P_{H2}: Hydrogen pressure on feed side in kPa

$a_{real} = 11.7$
$c_{real} = 9.94$
$d_{real} = 13.97$
$t_{real} = 0.025$
$P_{H_2 real} = 202.3$
$P_{0real} = 20$

$\sigma_a = 0.2309$
$\sigma_c = 0.334$
$\sigma_d = 0.032$
$\sigma_t = 0.0013$
$\sigma_{P_{H_2}} = 6.12$
$\sigma_{P_{H_2}} = 6.12$

$$\frac{\mathrm{d}\bar{P}}{\mathrm{da}} = \frac{c}{(100-c)\frac{\pi}{4}d^2}\,t\,\frac{1}{\sqrt{P_{H_2}}} \times 2.19228 \times 10^{-5} \qquad \frac{\mathrm{d}\bar{P}}{\mathrm{da}} = 2.774e^{-11}$$

$$\frac{\mathrm{d}\bar{P}}{\mathrm{dc}} = \frac{100a}{(100-c)^2\frac{\pi}{4}d^2}\,t\,\frac{1}{\sqrt{P_{H_2}}} \times 2.19228 \times 10^{-5} \qquad \frac{\mathrm{d}\bar{P}}{\mathrm{dc}} = 3.626e^{-11}$$

$$\frac{\mathrm{d}\bar{P}}{\mathrm{dd}} = \frac{-2ac}{(100-c)\frac{\pi}{4}d^3}\,t\,\frac{1}{\sqrt{P_{H_2}}} \times 2.19228 \times 10^{-5} \qquad \frac{\mathrm{d}\bar{P}}{\mathrm{dd}} = -4.647e^{-11}$$

$$\frac{\mathrm{d}\bar{P}}{\mathrm{dt}} = \frac{ac}{(100-c)\frac{\pi}{4}d^2}\cdot\frac{1}{\sqrt{P_{H_2}}} \times 2.19228 \times 10^{-5} \qquad \frac{\mathrm{d}\bar{P}}{\mathrm{dt}} = 1.298e^{-8}$$

$$\frac{\mathrm{d}\bar{P}}{\mathrm{d}P_{H_2}} = -\frac{ac}{2(100-c)\frac{\pi}{4}d^2}\,t\left(\frac{1}{\sqrt{P_{H_2}}}\right)^3 \times 2.19228 \times 10^{-5} \qquad \frac{\mathrm{d}\bar{P}}{\mathrm{dP}_{H_2}} = -8.023e^{-13}$$

$$\sigma_{\bar{P}} = \sqrt{\left(\frac{d\bar{P}}{da}\right)^2 \cdot \sigma_a^2 + \left(\frac{d\bar{P}}{dc}\right)^2 \cdot \sigma_c^2 + \left(\frac{d\bar{P}}{dd}\right)^2 \cdot \sigma_d^2 + \left(\frac{d\bar{P}}{dt}\right)^2 \cdot \sigma_t^2 + \left(\frac{d\bar{P}}{dP_{H_2}}\right)^2 \cdot \sigma_{P_{H_2}}^2}$$
$$= 2.23407e^{-11}$$

APPENDIX B

PARTS OF THE HYDROGEN PERMEATION SYSTEM

All the connections are either 1/8 inch or ¼ inch

Table B.1 Parts information of the bench-top system.

Part	Vender	Model	Notes
Mass flow controller (MFC)	MKS	M100B	Cable needed
MFCs power supply	MKS	247D	
Pressure sensor (feed)	MKS	722B Absolute Manometer	Cable needed
Pressure sensor readout	MKS	PDR2000 2 Channel Readout	
Back pressure regulator	Praxair	PRS40703061-TF2	
Ball valves	Swagelok	SS-41GS2	
Pressure gauge (permeate)	Ashcroft	Dual-Scale Gauge	
Muffle furnace	Fisher Scientific	NC9995039	120 V 5.8Cubic feet
Gas chromatography*	Agilent	GC7890 special	No injection; 2 TCD for gas only
Soap bubble flow meter	Restek	50 ml/1 ml	
Tubing 1	Grainger	Brass 1/8 inch tubing	From cylinder to MFC
Tubing 2 Stainless steel 316	Swagelok/Mcmaster	89785K113 (Mcmaster-Carr)	Cell
Tubing 3 Teflon PFA	Mcmaster	51805K41	

* The gas chromatography has two thermal conduct detectors which can collect hydrogen concentration as low as 1ppm

APPENDIX C

DESIGN OF STAINLESS STEEL MODULE TO SEAL THE SELF-SUPPORTED METALLIC MEMBRANES

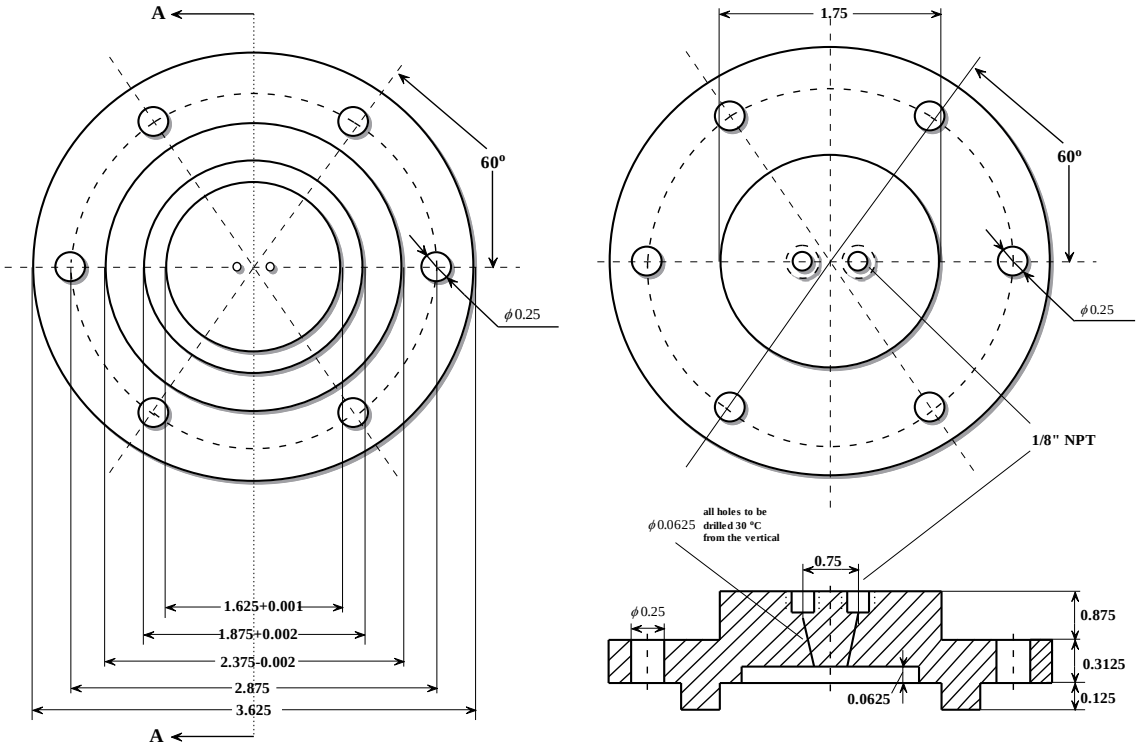

Figure C.1 Permeation cell-bulk top

Connections of 1/8” female NPT and 1/8” Swagelok connections need to be welded to the upper 1/8” NPT connections of the permeation cells. Otherwise the leaking rate would be large.

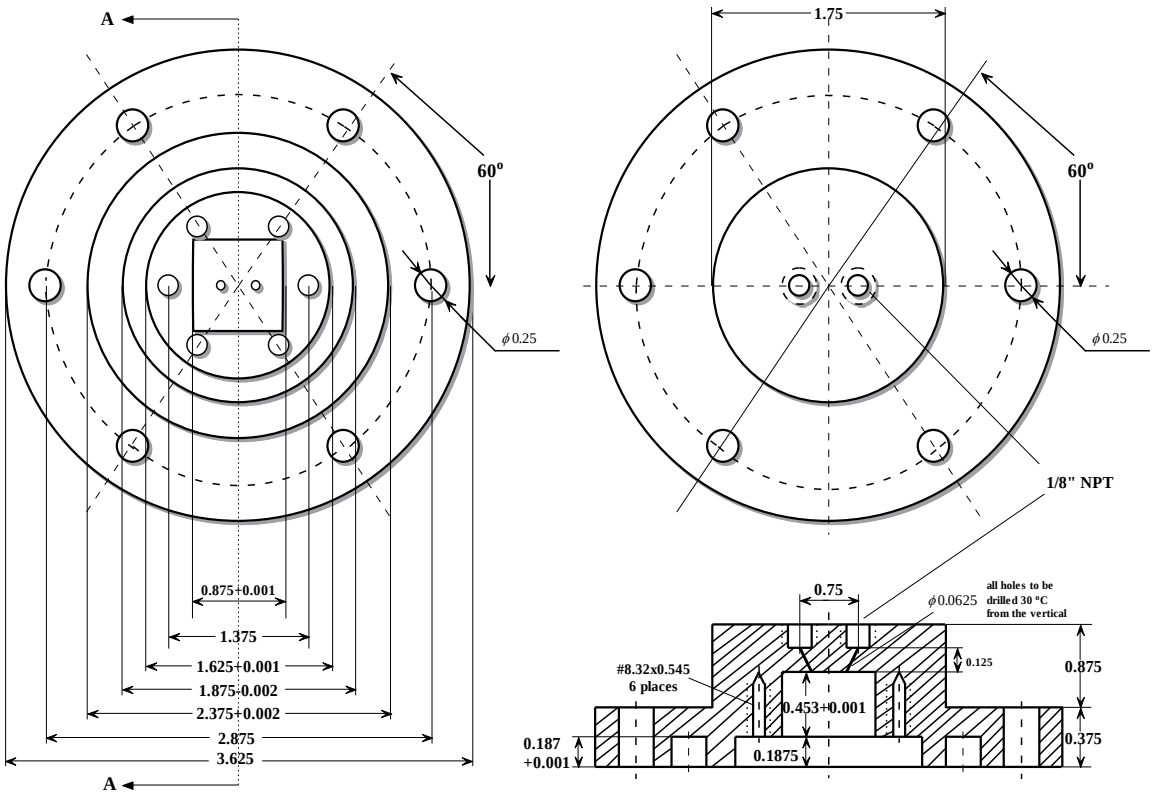

Figure C.2 Permeation cell bulk bottom

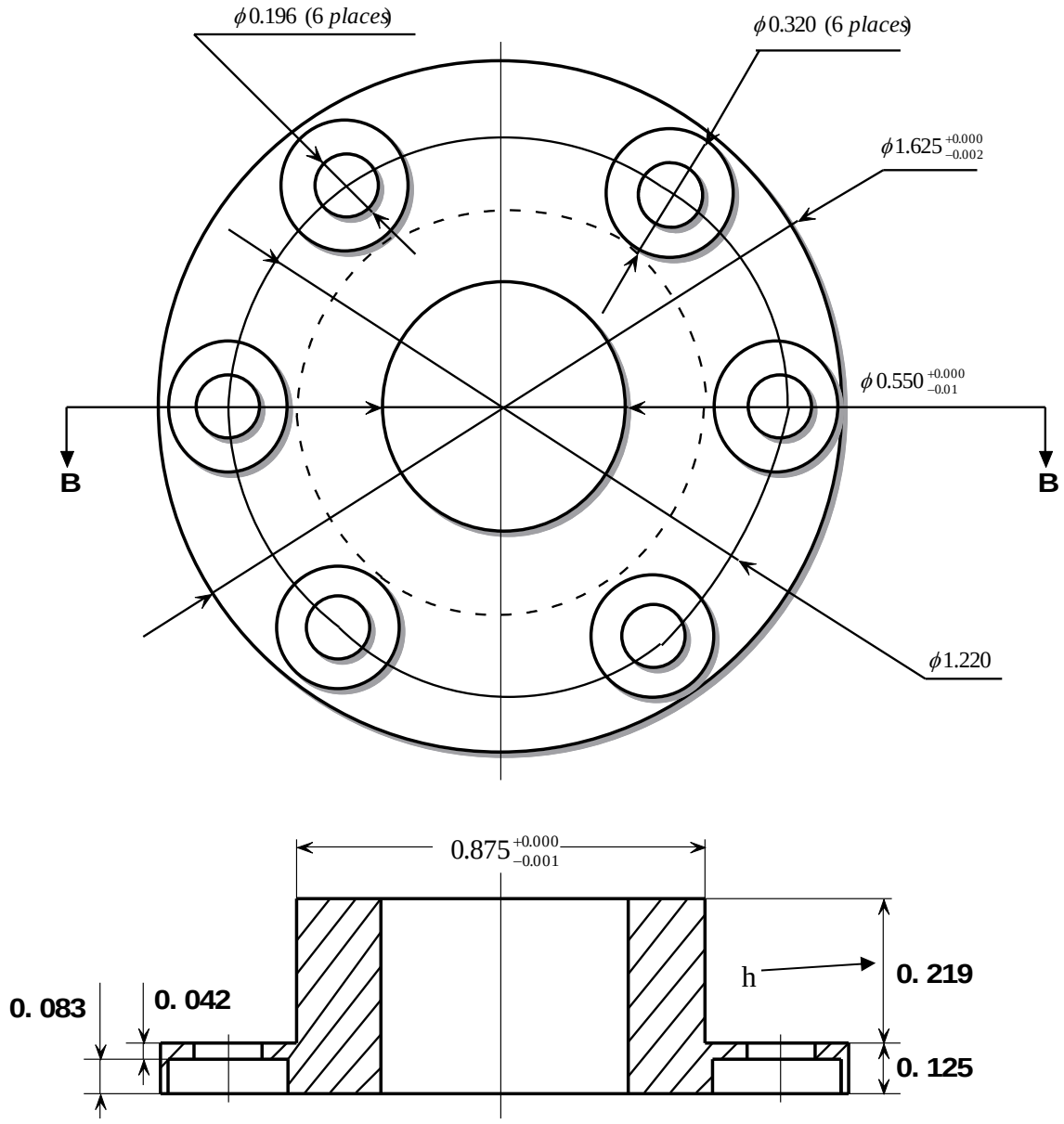

Figure C.3 Cell-fitting small part

Table C.1 Gaskets information

Gaskets	Dimension (inch)	Vendor	Notes
Graphite	ID 0.550xOD 0.875 x 0.125	Sealing devices Inc/Americansealandpacking	
Graphite	ID 0.550xOD 0.875 x 0.200	Americansealandpacking	
Graphite	ID 1.875xOD 2.375 x 0.125	Sealing devices Inc /Americansealandpacking	
Copper	OD .870 x ID.600 x .093	Coppergaskets.us	h is 0.298”

APPENDIX D

MODIFICATION OF THE HYDROGEN PERMEATION SYSTEM WITH THERMOCOUPLE INSIDE THE STAINLESS STEEL CELL

In order to monitor the temperature near the membrane during test, a thermocouple is installed from the tubing. Also, the hole for gas to go inside the cell was enlarged to get the thermocouple go through. The disk permeation cell fitting dimension has been changed to adjust the copper gaskets to maximize the sealing effect, with the figure below.

Table D.1 Gaskets and part information for modification

Parts	Dimension	Vendor	Notes
Copper Gaskets	OD .870" x ID.600" x .093"	Coppergaskets.us	
Stainless 316 Tubing	OD1/8"xID.093"x 0.016" wall	Mcmaster	
K-type Thermocouple	25"L, .063"Dia Probe	Cole-Parmer	EW-93631-21
Reducer	1/16" Swagelok x 1/8"	Swagelok	
T-connection	1/8" swagelok x3	Swagelok	

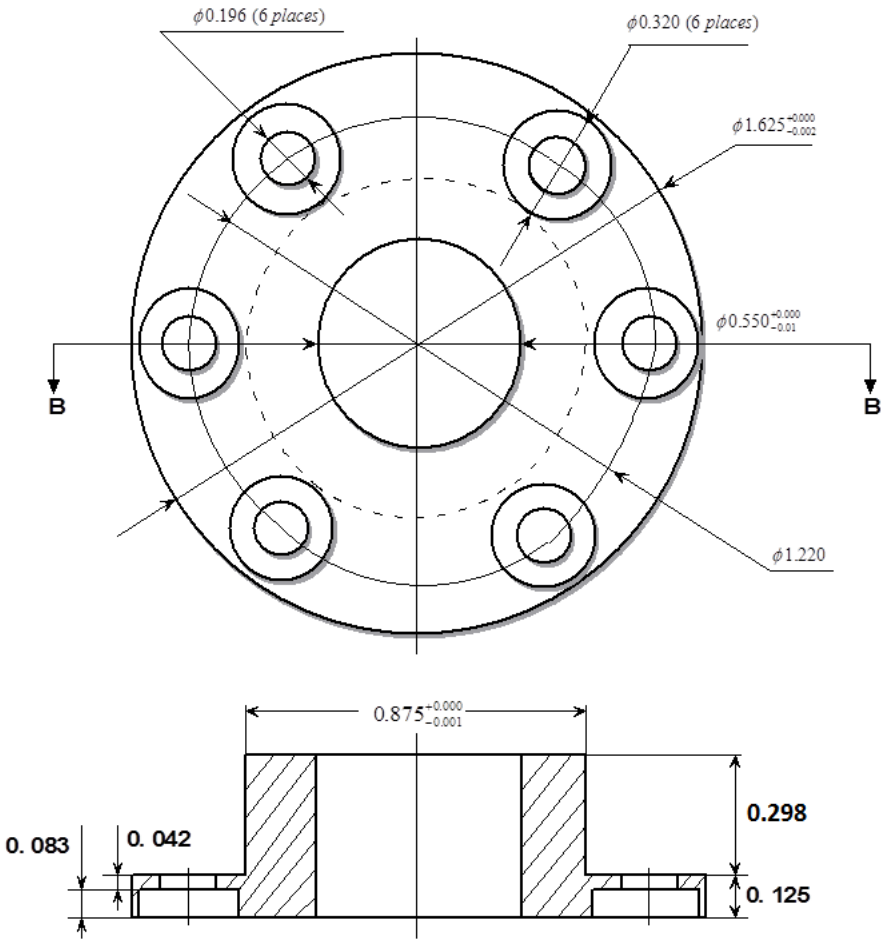

Figure D.1 Modified small part dimension

APPENDIX E

PERMEABILITY DATA OF $PD_{77}AG_{23}$ SAMPLES

Table E.1 Permeability data of Sample A (as-received samples)

Sample No.1			Sample No.2			Sample No.3		
Time	GC data	Permeability	Time	GC data	Permeability	Time	GC data	Permeability
(hr)	(ppm)	(mol m^{-1} s^{-1} $Pa^{-0.5}$)	(hr)	(ppm)	(mol m^{-1} s^{-1} $Pa^{-0.5}$)	(hr)	(ppm)	(mol m^{-1} s^{-1} $Pa^{-0.5}$)
2	8.70E+04	3.08E-09	0.5	6.35E+04	2.09E-09	0.5	6.20E+04	2.03E-09
3	1.22E+05	4.77E-09	1.5	8.87E+04	3.15E-09	1.5	8.85E+04	3.14E-09
4	1.59E+05	6.90E-09	2.5	1.29E+05	5.15E-09	2.5	1.23E+05	4.83E-09
5	1.90E+05	8.97E-09	3.5	1.53E+05	6.53E-09	3.5	1.48E+05	6.23E-09
6	1.97E+05	9.49E-09	4.5	1.62E+05	7.09E-09	4.5	1.72E+05	7.73E-09
7	2.01E+05	9.78E-09	5.5	1.68E+05	7.47E-09	5.5	1.85E+05	8.62E-09
8	2.06E+05	1.02E-08	6.5	1.73E+05	7.80E-09	6.5	1.91E+05	9.05E-09
9	2.09E+05	1.04E-08	7.5	1.78E+05	8.14E-09	7.5	1.95E+05	9.34E-09
10	2.10E+05	1.05E-08	8.5	1.80E+05	8.27E-09	8.5	1.96E+05	9.41E-09
11	2.13E+05	1.07E-08	9.5	1.84E+05	8.55E-09	9.5	1.99E+05	9.63E-09
12	2.15E+05	1.09E-08	10.5	1.86E+05	8.69E-09	10.5	2.02E+05	9.86E-09
13	2.17E+05	1.10E-08	11.5	1.88E+05	8.83E-09	11.5	2.04E+05	1.00E-08
14	2.19E+05	1.12E-08	12.5	1.92E+05	9.12E-09	12.5	2.05E+05	1.01E-08
15	2.19E+05	1.12E-08	13.5	1.93E+05	9.19E-09	13.5	2.07E+05	1.02E-08
16	2.22E+05	1.14E-08	14.5	1.96E+05	9.41E-09	14.5	2.08E+05	1.03E-08
17	2.22E+05	1.14E-08	15.5	1.97E+05	9.49E-09	15.5	2.11E+05	1.06E-08
18	2.25E+05	1.17E-08	16.5	2.00E+05	9.71E-09	16.5	2.13E+05	1.07E-08
19	2.26E+05	1.18E-08	17.5	2.01E+05	9.78E-09	17.5	2.15E+05	1.09E-08
20	2.28E+05	1.19E-08	18.5	2.03E+05	9.94E-09	18.5	2.16E+05	1.10E-08
21	2.29E+05	1.20E-08	19.5	2.04E+05	1.00E-08	19.5	2.16E+05	1.10E-08
22	2.30E+05	1.21E-08	20.5	2.06E+05	1.02E-08	20.5	2.19E+05	1.12E-08
23	2.31E+05	1.22E-08	21.5	2.07E+05	1.02E-08	21.5	2.19E+05	1.12E-08
24	2.32E+05	1.23E-08	22.5	2.10E+05	1.05E-08	22.5	2.20E+05	1.13E-08
			23.5	2.12E+05	1.06E-08	23.5	2.23E+05	1.15E-08

Table E.2 Permeability data of Sample B (24 hr air treatment)

Sample No.1			Sample No.2			Sample No.3		
Time (hr)	GC data (ppm)	Permeability (mol m^{-1} s^{-1} $Pa^{-0.5}$)	Time (hr)	GC data (ppm)	Permeability (mol m^{-1} s^{-1} $Pa^{-0.5}$)	Time (hr)	GC data (ppm)	Permeability (mol m^{-1} s^{-1} $Pa^{-0.5}$)
0	1.20E+05	4.68E-09	0	7.16E+04	2.52193E-09	0	1.16E+05	4.47E-09
1	1.44E+05	6.00E-09	1	1.39E+05	5.95449E-09	1	1.57E+05	6.79E-09
2	1.68E+05	7.49E-09	2	1.66E+05	7.66366E-09	2	1.83E+05	8.50E-09
3	1.84E+05	8.57E-09	3	1.85E+05	8.99895E-09	3	1.96E+05	9.43E-09
4	1.95E+05	9.36E-09	4	1.98E+05	9.98114E-09	4	2.06E+05	1.02E-08
5	2.01E+05	9.81E-09	5	2.08E+05	1.0777E-08	5	2.12E+05	1.07E-08
6	2.05E+05	1.01E-08	6	2.14E+05	1.1272E-08	6	2.16E+05	1.10E-08
7	2.05E+05	1.01E-08	7	2.18E+05	1.16096E-08	7	2.19E+05	1.12E-08
8	2.12E+05	1.07E-08	8	2.22E+05	1.19534E-08	9	2.26E+05	1.18E-08
9	2.14E+05	1.08E-08	9	2.25E+05	1.22153E-08	11	2.31E+05	1.22E-08
10	2.17E+05	1.11E-08	10	2.27E+05	1.23919E-08	13	2.35E+05	1.26E-08
11	2.18E+05	1.11E-08	11	2.28E+05	1.24808E-08	15	2.37E+05	1.28E-08
12	2.20E+05	1.13E-08	12	2.31E+05	1.275E-08	17	2.61E+05	1.50E-08
13	2.21E+05	1.14E-08	13	2.33E+05	1.29314E-08	19	2.62E+05	1.51E-08
14	2.23E+05	1.16E-08	14	2.37E+05	1.32994E-08	21	2.63E+05	1.52E-08
15	2.24E+05	1.16E-08	15	2.39E+05	1.34859E-08	22	2.81E+05	1.71E-08
16	2.26E+05	1.18E-08	16	2.39E+05	1.34859E-08	23	2.78E+05	1.68E-08
17	2.29E+05	1.21E-08	17	2.40E+05	1.35797E-08	24	2.70E+05	1.59E-08
18	2.30E+05	1.22E-08	18	2.41E+05	1.3674E-08			
19	2.32E+05	1.23E-08	19	2.42E+05	1.37688E-08			
20	2.33E+05	1.24E-08	20	2.42E+05	1.37688E-08			
21	2.34E+05	1.25E-08	21	2.43E+05	1.38639E-08			
22	2.34E+05	1.25E-08	22	2.45E+05	1.40556E-08			
23	2.35E+05	1.26E-08	23	2.46E+05	1.4152E-08			
			24	2.45E+05	1.40748E-08			

Table E.3 Permeability data of sample C (24 hr vacuum oven treatment)

Sample No.1			Sample No.2			Sample No.3		
Time (hr)	GC data (ppm)	Permeability (mol m^{-1} s^{-1} $Pa^{-0.5}$)	Time (hr)	GC data (ppm)	Permeability (mol m^{-1} s^{-1} $Pa^{-0.5}$)	Time (hr)	GC data (ppm)	Permeability (mol m^{-1} s^{-1} $Pa^{-0.5}$)
0.0	5.91E+04	1.84E-09	0	2.50E+04	6.96E-10	0.0	1.35E+05	5.17E-09
0.4	9.72E+04	3.3739E-09	0.5	4.70E+04	1.4113E-09	0.4	1.56E+05	6.30E-09
0.8	9.66E+04	3.34762E-09	1	5.05E+04	1.53309E-09	0.8	1.63E+05	6.70E-09
1.3	9.05E+04	3.08443E-09	1.5	5.20E+04	1.58597E-09	1.3	1.64E+05	6.76E-09
1.7	8.60E+04	2.89491E-09	2	5.35E+04	1.63925E-09	1.7	1.64E+05	6.76E-09
2.1	8.34E+04	2.78719E-09	2.5	5.48E+04	1.68575E-09	2.1	1.63E+05	6.70E-09
2.5	8.07E+04	2.67669E-09	3	5.58E+04	1.72173E-09	2.5	1.62E+05	6.64E-09
2.9	7.87E+04	2.59573E-09	3.5	5.63E+04	1.73979E-09	2.9	1.61E+05	6.58E-09
3.3	7.70E+04	2.52751E-09	4	5.70E+04	1.76514E-09	3.3	1.61E+05	6.58E-09
3.8	7.53E+04	2.45983E-09	4.5	5.73E+04	1.77604E-09	3.8	1.61E+05	6.58E-09
4.2	7.62E+04	2.49559E-09	5	5.73E+04	1.77604E-09	4.2	1.62E+05	6.64E-09
4.6	7.36E+04	2.39269E-09	5.5	5.71E+04	1.76877E-09	4.6	1.61E+05	6.58E-09
5.0	7.45E+04	2.42817E-09	6	5.73E+04	1.77604E-09	5.0	1.61E+05	6.58E-09
5.4	7.35E+04	2.38876E-09	6.5	5.69E+04	1.76152E-09	5.4	1.61E+05	6.58E-09
5.8	7.29E+04	2.3652E-09	7	5.67E+04	1.75427E-09	5.8	1.61E+05	6.58E-09
6.3	7.23E+04	2.34171E-09	7.5	5.63E+04	1.73979E-09	6.3	1.62E+05	6.64E-09
6.7	7.19E+04	2.32609E-09	8	5.60E+04	1.72895E-09	6.7	1.62E+05	6.64E-09
7.1	7.16E+04	2.31439E-09	8.5	5.57E+04	1.71812E-09	7.1	1.62E+05	6.64E-09
7.5	7.12E+04	2.29882E-09	9	5.56E+04	1.71452E-09	7.5	1.62E+05	6.64E-09
7.9	7.12E+04	2.29882E-09	9.5	5.52E+04	1.70012E-09	7.9	1.63E+05	6.70E-09
8.3	7.08E+04	2.28328E-09	10	5.50E+04	1.69293E-09	8.3	1.63E+05	6.70E-09
8.8	7.07E+04	2.2794E-09	10.5	5.47E+04	1.68216E-09	8.8	1.63E+05	6.70E-09
9.2	7.05E+04	2.27165E-09	11	5.44E+04	1.67141E-09	9.2	1.64E+05	6.76E-09
9.6	7.03E+04	2.2639E-09	11.5	5.41E+04	1.66067E-09	9.6	1.64E+05	6.76E-09
10.0	7.03E+04	2.2639E-09	12	5.38E+04	1.64995E-09	10.0	1.68E+05	6.99E-09
10.4	7.03E+04	2.2639E-09	12.5	5.34E+04	1.63568E-09	10.4	1.68E+05	6.99E-09
10.8	7.01E+04	2.25616E-09	13	5.30E+04	1.62144E-09	10.8	1.69E+05	7.05E-09
11.3	7.01E+04	2.25616E-09	13.5	5.20E+04	1.58597E-09	11.3	1.68E+05	6.99E-09
11.7	7.01E+04	2.25616E-09	14	5.24E+04	1.60013E-09	11.7	1.69E+05	7.05E-09
12.1	7.03E+04	2.2639E-09	14.5	5.22E+04	1.59305E-09	12.1	1.69E+05	7.05E-09
12.5	7.01E+04	2.25616E-09	15	5.22E+04	1.59305E-09	12.5	1.71E+05	7.17E-09
12.9	7.02E+04	2.26003E-09	16	5.21E+04	1.58951E-09	13.5	1.71E+05	7.17E-09
13.3	7.01E+04	2.25616E-09	17	5.20E+04	1.58597E-09	14.5	1.72E+05	7.23E-09
14.2	6.98E+04	2.24456E-09	18	5.21E+04	1.58951E-09	15.5	1.73E+05	7.29E-09
15.2	6.98E+04	2.24456E-09	19	5.22E+04	1.59305E-09	16.5	1.73E+05	7.29E-09
16.2	6.97E+04	2.2407E-09	20	5.30E+04	1.62144E-09	17.5	1.74E+05	7.35E-09
17.2	6.98E+04	2.24456E-09	21	5.40E+04	1.6571E-09	18.5	1.74E+05	7.35E-09
18.2	6.97E+04	2.2407E-09	22	5.53E+04	1.70372E-09	19.5	1.75E+05	7.41E-09
19.2	6.99E+04	2.24843E-09	23	5.62E+04	1.73617E-09	20.5	1.76E+05	7.47E-09
20.2	7.02E+04	2.26003E-09				21.5	1.76E+05	7.47E-09
21.2	7.08E+04	2.28328E-09				22.5	1.76E+05	7.47E-09
22.2	7.10E+04	2.29105E-09	24	5.79E+04	1.79788E-09	23.5	1.76E+05	7.47E-09
23.2	7.16E+04	2.31439E-09				24.5	1.78E+05	7.60E-09
23.9	7.19E+04	2.32609E-09						

Table E.4 Permeability data of Sample D (24 hr high vacuum treatment)

Sample No.1			Sample No.2		
Time (hr)	GC data (ppm)	Permeability (mol m^{-1} s^{-1} $Pa^{-0.5}$)	Time (hr)	GC data (ppm)	Permeability (mol m^{-1} s^{-1} $Pa^{-0.5}$)
0	5.80E+04	1.87E-09	0	7.40E+04	2.40E-09
1	7.30E+04	2.46E-09	1	1.01E+05	3.52E-09
2	1.16E+05	4.40E-09	2	1.44E+05	5.60E-09
3	1.43E+05	5.82E-09	3	1.78E+05	7.54E-09
4	1.66E+05	7.17E-09	4	1.95E+05	8.62E-09
5	1.85E+05	8.39E-09	6	2.09E+05	9.57E-09
6	1.90E+05	8.73E-09	8	2.16E+05	1.01E-08
8	1.90E+05	8.73E-09	10	2.22E+05	1.05E-08
10	1.90E+05	8.73E-09	12	2.26E+05	1.08E-08
12	1.99E+05	9.35E-09	14	2.30E+05	1.11E-08
14	2.01E+05	9.49E-09	16	2.33E+05	1.13E-08
16	2.06E+05	9.86E-09	18	2.35E+05	1.15E-08
18	2.10E+05	1.02E-08	20	2.36E+05	1.16E-08
20	2.14E+05	1.04E-08	22	2.38E+05	1.17E-08
22	2.15E+05	1.05E-08	23.5	2.38E+05	1.17E-08
23.3	2.17E+05	1.07E-08			

Table E.5 Permeability data of sample E (second hydrogen permeability test of Sample B)

Sample No.1			Sample No.2			Sample No.3		
Time (hr)	GC data (ppm)	Permeability (mol m^{-1} s^{-1} $Pa^{-0.5}$)	Time (hr)	GC data (ppm)	Permeability (mol m^{-1} s^{-1} $Pa^{-0.5}$)	Time (hr)	GC data (ppm)	Permeability (mol m^{-1} s^{-1} $Pa^{-0.5}$)
0.4	8.30E+04	2.89E-09	1.4	1.55E+05	6.56E-09	0.4	8.64E+04	3.04E-09
1.4	1.20E+05	4.63E-09	2.6	1.71E+05	7.55E-09	1.4	1.08E+05	4.03E-09
2.4	1.40E+05	5.70E-09	3.6	1.80E+05	8.14E-09	2.4	1.36E+05	5.48E-09
3.4	1.60E+05	6.87E-09	4.6	1.90E+05	8.82E-09	3.4	1.65E+05	7.17E-09
4.4	1.75E+05	7.81E-09	5.6	1.97E+05	9.31E-09	4.4	1.84E+05	8.41E-09
5.4	1.86E+05	8.54E-09	6.6	2.01E+05	9.60E-09	5.4	1.95E+05	9.17E-09
6.4	1.93E+05	9.03E-09	8.6	2.08E+05	1.01E-08	6.4	2.01E+05	9.60E-09
7.4	1.98E+05	9.38E-09	10.6	2.11E+05	1.03E-08	8.4	2.11E+05	1.03E-08
9.4	2.04E+05	9.82E-09	12.6	2.14E+05	1.06E-08	10.4	2.17E+05	1.08E-08
11.4	2.09E+05	1.02E-08	14.6	2.17E+05	1.08E-08	12.4	2.22E+05	1.12E-08
13.4	2.12E+05	1.04E-08	16.6	2.19E+05	1.10E-08	14.4	2.25E+05	1.14E-08
15.4	2.14E+05	1.06E-08	18.6	2.20E+05	1.10E-08	16.4	2.29E+05	1.18E-08
17.4	2.18E+05	1.09E-08	20.6	2.21E+05	1.11E-08	18.4	2.31E+05	1.19E-08
19.4	2.22E+05	1.12E-08	21.3	2.22E+05	1.12E-08	20.4	2.33E+05	1.21E-08
21.4	2.23E+05	1.13E-08	21.8	2.22E+05	1.12E-08	22.4	2.33E+05	1.21E-08
21.9	2.23E+05	1.13E-08				24.0	2.36E+05	1.23E-08
22.9	2.24E+05	1.14E-08						

APPENDIX F

PERMEABILITY DATA OF AMORPHOUS CU-ZR SAMPLES

Table F.1 Raw data of hydrogen permeability of Pd-coated $Cu_{63}Zr_{37}$

Sample No.1			Sample No.2			Sample No.3		
Time	GC data	Permeability	Time	GC data	Permeability	Time	GC data	Permeability
(hr)	(ppm)	(mol $m^{-1} s^{-1} Pa^{-0.5}$)	(hr)	(ppm)	(mol $m^{-1} s^{-1} Pa^{-0.5}$)	(hr)	(ppm)	(mol $m^{-1} s^{-1} Pa^{-0.5}$)
0.00	2495.45	1.41E-11	0.00	2241.63	1.34E-11	0.00	13200.00	8.27E-11
0.33	2001.83	1.13E-11	0.33	8228.09	5.13E-11	0.33	12700.00	7.93E-11
0.67	6739.10	3.94E-11	0.67	8497.49	5.30E-11	0.67	9137.91	5.60E-11
1.00	6967.40	4.08E-11	1.00	7803.24	4.85E-11	1.00	6826.43	4.12E-11
1.33	7448.28	4.38E-11	1.33	7100.92	4.39E-11	1.33	5634.11	3.38E-11
1.67	7831.94	4.62E-11	1.67	6567.45	4.05E-11	1.67	4837.37	2.88E-11
2.00	7849.38	4.63E-11	2.00	6120.77	3.76E-11	2.00	4188.20	2.48E-11
2.33	7435.53	4.37E-11	2.33	5677.68	3.48E-11	2.33	3582.34	2.11E-11
2.67	6288.57	3.67E-11	2.67	5285.93	3.23E-11	2.67	3079.81	1.81E-11
3.00	5019.83	2.90E-11	3.00	4938.24	3.01E-11	3.00	2660.31	1.56E-11
3.33	4065.63	2.33E-11	3.33	4648.20	2.83E-11	3.33	2336.58	1.36E-11
3.67	3398.00	1.94E-11	3.67	4391.34	2.67E-11	3.67	2066.05	1.20E-11
4.00	2946.55	1.68E-11	4.00	4131.59	2.50E-11	4.00	1855.24	1.08E-11
4.33	2637.95	1.50E-11	4.33	3899.76	2.36E-11	4.33	1686.95	9.77E-12
4.67	2423.08	1.37E-11	4.67	3608.04	2.18E-11	4.67	1550.75	8.97E-12
5.00	2249.51	1.27E-11	5.00	3309.63	1.99E-11	5.00	1442.87	8.33E-12
5.33	2113.79	1.19E-11	5.33	3019.78	1.81E-11	5.33	1355.24	7.82E-12
5.67	1989.58	1.12E-11	5.67	2579.41	1.54E-11	5.67	1281.05	7.38E-12
6.00	1890.02	1.06E-11	6.00	1858.91	1.10E-11	6.00	1216.53	7.00E-12

Table F.2 Raw data of hydrogen permeability of non-Pd-coated $Cu_{63}Zr_{37}$

Sample No.1			Sample No.2			Sample No.3		
Time	GC data	Permeability	Time	GC data	Permeability	Time	GC data	Permeability
(hr)	(ppm)	(mol $m^{-1} s^{-1} Pa^{-0.5}$)	(hr)	(ppm)	(mol $m^{-1} s^{-1} Pa^{-0.5}$)	(hr)	(ppm)	(mol $m^{-1} s^{-1} Pa^{-0.5}$)
0.00	2345.82	1.36E-11	0.00	912.96	5.00E-12	0.00	516.59	2.98E-12
0.42	9444.08	5.75E-11	0.33	5969.23	3.42E-11	0.67	6329.63	3.87E-11
0.83	6958.89	4.17E-11	0.67	5374.14	3.07E-11	1.00	5787.16	3.52E-11
1.25	4315.04	2.54E-11	1.00	5591.57	3.20E-11	1.75	6782.35	4.16E-11
1.67	4181.00	2.46E-11	1.33	5755.49	3.30E-11	1.92	7237.69	4.45E-11
2.08	3422.37	2.00E-11	1.67	5429.69	3.10E-11	2.00	7374.51	4.54E-11
2.50	2352.72	1.36E-11	2.00	4822.75	2.74E-11	2.50	6194.39	3.78E-11
2.92	1874.05	1.08E-11	2.33	4111.15	2.33E-11	2.67	5397.45	3.28E-11
3.33	1633.95	9.38E-12	2.67	3403.24	1.91E-11	3.00	4093.92	2.46E-11
3.75	1464.86	8.39E-12	3.00	2797.64	1.57E-11	3.50	3152.66	1.88E-11
4.17	1340.92	7.67E-12	3.33	2334.29	1.30E-11	3.58	3056.87	1.82E-11
4.58	1241.92	7.09E-12	3.67	1999.65	1.11E-11	4.00	2700.61	1.60E-11
5.00	1157.61	6.60E-12	4.00	1764.53	9.77E-12	4.50	2421.33	1.43E-11
5.42	1079.46	6.15E-12	4.33	1583.78	8.75E-12	5.00	2222.19	1.31E-11
5.83	1015.31	5.78E-12	4.67	1446.46	7.98E-12	5.08	2177.47	1.29E-11
6.25	958.10	5.45E-12	5.00	1341.85	7.39E-12	5.50	2066.42	1.22E-11
			5.33	1249.76	6.88E-12	5.75	1998.94	1.18E-11
			5.67	1173.55	6.45E-12	6.00	1934.88	1.14E-11
			6.00	1112.32	6.11E-12			

Table F.3 Raw permeability data of Pd-coated $Cu_{46}Zr_{54}$

Sample No.1			Sample No.2			Sample No.3		
Time	GC data	Permeability	Time	GC data	Permeability	Time	GC data	Permeability
(hr)	(ppm)	(mol m^{-1} s^{-1} $Pa^{-0.5}$)	(hr)	(ppm)	(mol m^{-1} s^{-1} $Pa^{-0.5}$)	(hr)	(ppm)	(mol m^{-1} s^{-1} $Pa^{-0.5}$)
0.00	132.68	7.53E-13	0.00	159.90	9.55E-13	0.00	200.70	1.14E-12
0.03	134.43	7.63E-13	0.03	163.30	9.76E-13	0.03	184.10	1.05E-12
0.07	131.47	7.46E-13	0.07	156.80	9.37E-13	0.07	188.70	1.07E-12
0.18	224.70	1.28E-12	0.10	154.60	9.23E-13	0.10	186.40	1.06E-12
0.22	224.71	1.28E-12	0.13	152.60	9.11E-13	0.13	178.30	1.01E-12
0.25	212.66	1.21E-12	0.17	159.20	9.51E-13	0.17	183.30	1.04E-12
0.28	197.24	1.12E-12	0.20	161.30	9.64E-13	0.20	176.20	1.00E-12
0.32	176.44	1.00E-12	0.23	159.10	9.50E-13	0.23	165.50	9.41E-13
0.35	175.06	9.95E-13	0.27	159.10	9.50E-13	0.27	172.40	9.80E-13
0.38	146.04	8.30E-13	0.30	160.20	9.57E-13	0.30	164.50	9.35E-13
0.42	164.13	9.33E-13	0.33	177.70	1.06E-12	0.33	163.10	9.27E-13
0.45	129.76	7.37E-13	0.37	152.10	9.08E-13	0.37	164.70	9.36E-13
0.48	143.11	8.13E-13	0.40	173.30	1.04E-12	0.40	172.50	9.81E-13
0.52	152.14	8.64E-13	0.43	155.60	9.29E-13	0.43	143.20	8.13E-13
0.55	134.78	7.65E-13	0.47	165.10	9.86E-13	0.47	153.40	8.72E-13
0.58	128.43	7.29E-13	0.50	177.30	1.06E-12	0.50	162.30	9.23E-13
0.62	136.45	7.75E-13	0.53	175.30	1.05E-12	0.53	158.80	9.03E-13
0.65	128.97	7.32E-13	0.57	175.50	1.05E-12	0.57	146.50	8.32E-13
0.68	126.51	7.18E-13	0.60	166.90	9.97E-13	0.63	156.20	8.88E-13
0.72	129.78	7.37E-13	0.63	169.20	1.01E-12	0.67	152.30	8.65E-13
0.75	127.79	7.25E-13	0.67	184.00	1.10E-12	0.70	148.50	8.44E-13
0.78	131.52	7.47E-13	0.70	180.80	1.08E-12	0.73	118.50	6.72E-13
0.82	134.11	7.62E-13	0.73	183.70	1.10E-12	0.77	138.00	7.84E-13
0.85	150.48	8.55E-13	0.77	187.80	1.12E-12	0.80	118.60	6.73E-13
0.88	170.17	9.68E-13	0.80	175.40	1.05E-12	0.83	138.00	7.84E-13
0.92	182.37	1.04E-12	0.83	186.80	1.12E-12	0.87	137.00	7.78E-13
0.95	209.97	1.20E-12	0.87	187.60	1.12E-12	0.90	136.00	7.72E-13
0.98	232.52	1.32E-12	0.90	185.90	1.11E-12	0.93	135.60	7.70E-13
1.02	255.50	1.46E-12	0.93	187.00	1.12E-12	0.97	131.00	7.44E-13
1.05	271.30	1.55E-12	0.97	193.30	1.16E-12	1.00	120.70	6.85E-13
1.08	281.34	1.60E-12	1.00	182.60	1.09E-12	1.03	137.80	7.83E-13
1.12	299.37	1.71E-12	1.03	174.50	1.04E-12	1.07	132.50	7.52E-13
1.15	307.36	1.75E-12	1.07	183.10	1.09E-12	1.10	119.50	6.78E-13
1.18	293.54	1.67E-12	1.10	189.80	1.13E-12	1.13	135.20	7.68E-13
1.22	278.75	1.59E-12	1.13	173.50	1.04E-12	1.17	129.00	7.32E-13
1.25	262.29	1.50E-12	1.17	173.30	1.04E-12	1.20	98.20	5.57E-13
1.28	244.18	1.39E-12	1.20	181.20	1.08E-12	1.23	117.70	6.68E-13
1.32	228.62	1.30E-12	1.23	171.50	1.02E-12	1.27	162.10	9.21E-13
1.35	203.32	1.16E-12	1.27	174.00	1.04E-12	1.30	125.70	7.14E-13
1.38	180.39	1.03E-12	1.30	193.30	1.16E-12	1.33	126.50	7.18E-13
1.42	164.80	9.37E-13	1.33	183.30	1.10E-12	1.37	120.80	6.86E-13
1.45	151.82	8.63E-13	1.50	169.80	1.01E-12	1.40	119.40	6.78E-13
1.48	143.27	8.14E-13	1.53	171.10	1.02E-12	1.43	112.30	6.37E-13
1.52	135.55	7.70E-13	1.57	185.90	1.11E-12	1.47	117.10	6.64E-13
1.55	115.26	6.54E-13	1.60	165.50	9.89E-13	1.50	120.00	6.81E-13
1.58	117.04	6.64E-13	1.63	174.60	1.04E-12	1.53	121.40	6.89E-13
1.62	130.87	7.43E-13	1.67	182.70	1.09E-12	1.57	127.50	7.24E-13
1.65	119.69	6.79E-13	1.70	185.10	1.11E-12	1.60	129.40	7.35E-13
1.68	121.69	6.91E-13	1.73	187.80	1.12E-12	1.63	133.00	7.55E-13
1.72	106.46	6.04E-13	1.77	185.00	1.11E-12	1.67	108.30	6.14E-13
1.75	113.30	6.43E-13	1.80	179.90	1.08E-12	1.70	110.50	6.27E-13
1.78	105.50	5.98E-13	1.83	196.50	1.18E-12	1.73	120.70	6.85E-13
1.82	108.94	6.18E-13	1.87	176.80	1.06E-12	1.77	128.00	7.27E-13
1.85	116.53	6.61E-13	1.90	183.60	1.10E-12	1.80	116.30	6.60E-13
1.88	100.76	5.71E-13	1.93	182.50	1.09E-12			
1.92	93.45	5.30E-13	1.97	168.30	1.01E-12	1.83	123.80	7.03E-13
1.95	124.42	7.06E-13	2.00	175.70	1.05E-12			
1.98	103.02	5.84E-13	2.03	178.80	1.07E-12			

Table F.4 Raw permeability data of $Cu_{46}Zr_{54}$ uncoated

Sample No.1			Sample No.2			Sample No.3		
Time	GC data	Permeability	Time	GC data	Permeability	Time	GC data	Permeability
(hr)	(ppm)	(mol $m^{-1} s^{-1} Pa^{-0.5}$)	(hr)	(ppm)	(mol $m^{-1} s^{-1} Pa^{-0.5}$)	(hr)	(ppm)	(mol $m^{-1} s^{-1} Pa^{-0.5}$)
0.00	2625.39	1.50E-11	0.00	1075.72	6.09E-12	0.00	295.04	1.62E-12
0.33	1168.58	6.57E-12	0.42	658.15	3.70E-12	0.40	244.51	1.34E-12
0.75	716.65	4.00E-12	0.83	3287.08	1.91E-11	0.50	231.61	1.27E-12
1.17	504.88	2.81E-12	1.25	4902.77	2.88E-11	1.05	202.30	1.11E-12
1.58	386.52	2.15E-12	1.67	2869.33	1.66E-11	1.38	273.47	1.50E-12
2.00	364.24	2.02E-12	2.08	2869.75	1.66E-11	1.72	295.03	1.62E-12
2.42	1177.05	6.62E-12	2.50	188.22	1.05E-12	2.05	264.45	1.45E-12
2.83	914.57	5.13E-12	2.92	119.28	6.62E-13	2.38	238.61	1.31E-12
3.25	531.56	2.96E-12	3.33	92.77	5.14E-13	2.72	220.76	1.21E-12
3.67	418.01	2.32E-12	3.75	82.80	4.59E-13	3.05	203.95	1.12E-12
4.08	387.10	2.15E-12	4.17	77.99	4.32E-13	3.38	206.06	1.13E-12
4.50	366.60	2.03E-12	4.58	74.74	4.14E-13	3.72	212.99	1.17E-12
4.92	359.44	1.99E-12				4.05	226.44	1.24E-12
5.33	353.37	1.96E-12				4.72	235.28	1.29E-12
5.75	357.09	1.98E-12	5.00	75.10	4.16E-13	5.05	242.70	1.33E-12
6.17	369.31	2.05E-12				5.55	265.26	1.46E-12
						6.05	275.27	1.51E-12

Table F.5 Raw permeability data of Pd-coated $Cu_{40}Zr_{60}$

Sample No.1			Sample No.2		
Time (hr)	GC data (ppm)	Permeability (mol m^{-1} s^{-1} $Pa^{-0.5}$)	Time (hr)	GC data (ppm)	Permeability (mol m^{-1} s^{-1} $Pa^{-0.5}$)
0.00	318.00	1.67E-12	0.00	1195.00	7.03E-12
0.42	3597.32	1.96E-11	0.10	6002.50	3.69E-11
0.83	1874.56	1.01E-11	0.13	7131.40	4.41E-11
1.25	121.58	6.33E-13	0.17	7768.20	4.83E-11
1.67	78.54	4.08E-13	0.20	7852.40	4.88E-11
2.08	71.42	3.71E-13	0.23	7702.50	4.78E-11
2.50	71.29	3.71E-13	0.27	7369.70	4.57E-11
2.92	67.31	3.50E-13	0.30	6882.40	4.25E-11
3.33	65.88	3.42E-13	0.33	6355.80	3.91E-11
3.75	65.21	3.39E-13	0.37	5815.20	3.57E-11
4.17	64.08	3.33E-13	0.40	5300.00	3.24E-11
4.58	63.49	3.30E-13	0.43	4838.10	2.95E-11
5.00	63.79	3.31E-13	0.47	4362.90	2.65E-11
5.42	66.19	3.44E-13	0.50	3906.00	2.36E-11
5.83	64.55	3.35E-13	0.53	3477.90	2.10E-11
6.25	64.71	3.36E-13	0.57	3030.70	1.82E-11
			0.60	2638.60	1.58E-11
			0.63	2294.00	1.37E-11
			0.67	1945.90	1.16E-11
			0.70	1641.40	9.71E-12
			0.73	1368.60	8.07E-12
			0.77	1151.80	6.77E-12
			0.80	929.80	5.45E-12
			0.83	741.80	4.34E-12
			0.87	571.90	3.33E-12
			0.90	424.00	2.46E-12
			0.93	308.60	1.79E-12
			0.97	218.00	1.26E-12
			1.00	166.80	9.62E-13
			1.03	156.60	9.03E-13
			1.07	139.70	8.05E-13
			1.27	128.90	7.43E-13
			1.30	120.50	6.94E-13
			1.33	125.30	7.22E-13
			1.37	129.60	7.47E-13
			1.40	80.60	4.63E-13
			1.43	108.20	6.23E-13

Table F.6 Raw permeability data of uncoated $Cu_{40}Zr_{60}$

Sample No.1			Sample No.2			Sample No.3		
Time	GC data	Permeability	Time	GC data	Permeability	Time	GC data	Permeability
(hr)	(ppm)	(mol $m^{-1} s^{-1} Pa^{-0.5}$)	(hr)	(ppm)	(mol $m^{-1} s^{-1} Pa^{-0.5}$)	(hr)	(ppm)	(mol $m^{-1} s^{-1} Pa^{-0.5}$)
0.00	857.50	4.84E-12	0.00	1109.17	6.52E-12	0.00	215.50	1.15E-12
0.03	888.83	5.02E-12	0.03	1126.04	6.62E-12	0.03	191.40	1.02E-12
0.07	914.27	5.16E-12	0.07	1032.66	6.06E-12	0.07	200.30	1.06E-12
0.10	929.86	5.25E-12	0.10	999.76	5.87E-12	0.10	190.80	1.01E-12
0.13	943.85	5.33E-12	0.13	970.40	5.69E-12	0.13	195.10	1.04E-12
0.17	964.71	5.45E-12	0.17	934.04	5.48E-12	0.17	193.50	1.03E-12
0.20	1009.76	5.71E-12	0.20	913.00	5.35E-12	0.20	175.40	9.31E-13
0.23	1045.23	5.91E-12	0.23	898.15	5.26E-12	0.23	181.50	9.63E-13
0.27	1112.92	6.30E-12	0.27	870.41	5.10E-12	0.30	164.40	8.72E-13
0.30	1170.94	6.64E-12	0.30	847.80	4.96E-12	0.33	167.50	8.89E-13
0.33	1231.24	6.98E-12	0.33	825.21	4.83E-12	0.37	160.40	8.51E-13
0.37	1291.97	7.33E-12	0.37	796.28	4.66E-12	0.40	145.00	7.69E-13
0.40	1356.02	7.70E-12	0.40	774.96	4.53E-12	0.43	160.00	8.49E-13
0.43	1420.67	8.08E-12	0.43	757.96	4.43E-12	0.47	156.50	8.30E-13
0.47	1480.80	8.43E-12	0.47	725.49	4.24E-12	0.50	164.60	8.73E-13
0.50	1540.02	8.77E-12	0.57	665.76	3.89E-12	0.53	145.00	7.69E-13
0.53	1601.75	9.13E-12	0.70	602.46	3.51E-12	0.57	148.80	7.89E-13
0.57	1692.58	9.66E-12	0.87	551.82	3.21E-12	0.60	137.00	7.26E-13
0.60	1743.19	9.95E-12	1.03	514.54	2.99E-12	0.63	141.00	7.47E-13
0.63	1804.79	1.03E-11	1.20	493.59	2.87E-12	0.67	120.70	6.39E-13
0.67	1883.56	1.08E-11	1.37	466.90	2.71E-12	0.70	142.60	7.56E-13
0.70	1952.38	1.12E-11	1.53	449.55	2.61E-12	0.73	140.00	7.42E-13
0.73	2009.39	1.15E-11	1.70	424.30	2.46E-12	0.77	148.00	7.85E-13
0.77	2073.68	1.19E-11	1.87	409.45	2.38E-12	0.83	129.80	6.88E-13
0.80	2106.65	1.21E-11	2.03	396.26	2.30E-12	0.87	131.40	6.96E-13
0.83	2158.70	1.24E-11	2.20	382.02	2.22E-12	0.90	141.70	7.51E-13
0.87	2184.65	1.25E-11	2.37	369.99	2.15E-12	0.93	125.80	6.66E-13
0.90	2235.85	1.28E-11	2.53	343.48	1.99E-12	0.97	155.00	8.22E-13
0.93	2241.32	1.29E-11	2.70	345.73	2.00E-12	1.00	130.40	6.91E-13
0.97	2286.07	1.31E-11	2.87	327.79	1.90E-12	1.03	141.90	7.52E-13
1.00	2312.64	1.33E-11	3.03	315.87	1.83E-12	1.07	97.80	5.18E-13
1.17	2403.73	1.38E-11	3.20	307.61	1.78E-12	1.10	126.20	6.69E-13
1.33	2433.39	1.40E-11	3.37	286.63	1.66E-12	1.13	126.10	6.68E-13
1.50	2470.48	1.42E-11	3.53	283.17	1.64E-12	1.17	111.80	5.92E-13
1.67	2520.28	1.45E-11	3.87	261.31	1.51E-12	1.20	119.10	6.31E-13
1.83	2529.48	1.46E-11	4.37	258.12	1.49E-12	1.23	127.00	6.73E-13
2.00	2553.28	1.47E-11	4.70	241.94	1.40E-12	1.27	122.70	6.50E-13
2.25	2573.68	1.48E-11	4.87	235.39	1.36E-12	1.30	89.50	4.73E-13
2.50	2590.31	1.49E-11	5.03	229.97	1.33E-12	1.33	88.40	4.68E-13
2.75	2605.03	1.50E-11	5.20	217.06	1.25E-12	1.37	89.50	4.73E-13
3.00	2647.74	1.53E-11	5.37	220.85	1.28E-12	1.40	122.80	6.51E-13
3.33	2651.52	1.53E-11	5.53	219.01	1.27E-12	1.43	131.20	6.95E-13
3.67	2684.85	1.55E-11	5.70	219.04	1.27E-12	1.47	118.30	6.27E-13
4.00	2690.87	1.55E-11	5.87	207.86	1.20E-12	1.50	116.60	6.18E-13
4.33	2717.72	1.57E-11	6.20	209.78	1.21E-12	1.53	122.00	6.46E-13
4.67	2748.48	1.59E-11	6.37	196.68	1.14E-12	1.57	111.30	5.89E-13
4.69	2744.70	1.58E-11	6.53	196.89	1.14E-12	1.60	109.70	5.81E-13
4.73	2743.98	1.58E-11	6.57	199.63	1.15E-12	1.63	112.40	5.95E-13
4.76	2750.37	1.59E-11	6.60	186.36	1.08E-12	1.67	83.10	4.39E-13
4.79	2756.61	1.59E-11	6.63	195.08	1.13E-12	1.70	123.70	6.55E-13
4.83	2732.14	1.58E-11	6.67	197.01	1.14E-12	1.73	119.00	6.30E-13
4.86	2727.68	1.57E-11	6.70	197.64	1.14E-12	1.77	123.40	6.54E-13
4.89	2743.74	1.58E-11				1.80	82.00	4.34E-13
4.93	2755.49	1.59E-11				1.83	118.80	6.29E-13
4.96	2733.84	1.58E-11				1.87	117.90	6.24E-13
4.99	2745.43	1.58E-11				1.90	117.00	6.20E-13
5.03	2745.60	1.58E-11				1.93	116.40	6.16E-13
5.06	2768.52	1.60E-11				1.97	78.70	4.16E-13
5.09	2762.29	1.59E-11				2.00	123.80	6.56E-13

APPENDIX G

PERMEABILITY DATA OF AMORPHOUS NINB-BASED MEMBRANES

Table G.1 Raw data of hydrogen permeability of $Ni_{60}Nb_{35}Sn_5$ Pd-coated amorphous membrane

Sample No.1		
Time (hr)	GC data (ppm)	Permeability (mol m^{-1} s^{-1} $Pa^{-0.5}$)
0.03	10200	4.11E-11
0.07	10200	4.11E-11
0.10	10200	4.11E-11
0.13	10200	4.11E-11
0.17	10200	4.11E-11
0.20	10200	4.15E-11
0.23	10300	4.15E-11
0.27	10300	4.11E-11
0.30	10200	4.11E-11
0.33	10200	4.07E-11
0.37	10100	4.07E-11
0.40	10100	4.07E-11
0.43	10100	4.00E-11
0.47	9948.3	3.99E-11
0.50	9904.5	3.97E-11
0.53	9874.4	3.98E-11
0.57	9896.5	3.97E-11
0.60	9857.4	3.95E-11
0.63	9822.8	3.94E-11
0.67	9787.7	3.89E-11
0.70	9688.1	3.91E-11
0.73	9721.7	3.89E-11
0.77	9672.8	3.87E-11
0.80	9631.7	3.86E-11
0.83	9598.8	3.82E-11
0.92	9507.6	3.78E-11
1.00	9422.6	3.76E-11
1.08	9377.6	3.74E-11
1.17	9320.4	3.72E-11
1.25	9269.7	3.70E-11
1.33	9226.5	3.68E-11
1.42	9188.8	3.64E-11
1.50	9090.8	3.65E-11
1.58	9127	3.64E-11
1.67	9095.9	3.64E-11
1.75	9082.3	3.60E-11
1.83	9007.6	3.61E-11
1.92	9022.6	3.61E-11

Table G.1 Continued

Sample No.1		
Time (hr)	GC data (ppm)	Permeability (mol m^{-1} s^{-1} $Pa^{-0.5}$)
2.00	9014.1	3.58E-11
2.08	8958.7	3.60E-11
2.17	9002.3	3.60E-11
2.25	8994	3.59E-11
2.33	8964.1	3.56E-11
2.42	8904.4	3.58E-11
2.50	8944	3.57E-11
2.58	8928.6	3.56E-11
2.67	8909.9	3.53E-11
2.75	8829.9	3.55E-11
2.83	8872.3	3.52E-11
3.00	8810.1	3.48E-11
3.33	8722.7	3.45E-11
3.50	8633.6	3.45E-11
3.67	8649.4	3.42E-11
3.83	8574.8	3.40E-11
4.00	8526.5	3.38E-11
4.17	8486.7	3.37E-11
4.33	8442.1	3.33E-11
4.50	8344.9	3.33E-11
4.67	8356.5	3.32E-11
4.83	8322.2	3.31E-11
5.00	8299.6	3.27E-11
5.17	8211.8	3.23E-11
5.33	8111.9	3.23E-11
5.50	8125.2	3.23E-11
5.67	8108.1	3.20E-11
5.83	8041.4	3.16E-11
6.00	7948.1	3.17E-11
6.17	7977.3	3.16E-11
6.33	7947	3.15E-11
6.50	7922.3	3.14E-11
6.67	7902.3	3.13E-11
6.83	7870.1	3.09E-11
7.00	7782.1	3.10E-11
7.17	7811.5	3.10E-11
7.33	7807.6	3.08E-11
7.50	7752	3.05E-11
8.00	7627.7	3.04E-11

Table G.1 Continued

Sample No.1		
Time (hr)	GC data (ppm)	Permeability (mol m^{-1} s^{-1} $Pa^{-0.5}$)
8.17	7660.8	3.01E-11
8.33	7600.4	3.03E-11
8.50	7639.4	3.01E-11
8.67	7589.9	3.01E-11
8.83	7595.1	3.00E-11
9.00	7566.2	3.00E-11
9.17	7555.8	2.96E-11
9.33	7471.7	2.97E-11
9.50	7502.6	2.97E-11
9.67	7484.5	2.96E-11
9.83	7472.9	2.96E-11
10.00	7462.9	2.95E-11
10.17	7439.7	2.94E-11
10.33	7428.5	2.92E-11
10.50	7374.3	2.93E-11
10.67	7399.3	2.92E-11
10.83	7387.2	2.90E-11
11.00	7329.1	2.91E-11
11.17	7360.8	2.89E-11
11.33	7312.2	2.91E-11
11.50	7349.7	2.90E-11
11.67	7328	2.89E-11
11.83	7307.9	2.90E-11
12.00	7337.3	2.87E-11
12.17	7262.5	2.87E-11
12.33	7264.3	2.87E-11
12.50	7262.9	2.88E-11
12.67	7271.1	2.88E-11
12.83	7268.3	2.87E-11
13.00	7256.9	2.85E-11
13.17	7205.5	2.87E-11
13.33	7243.3	2.86E-11
13.50	7241.6	2.85E-11
13.67	7198.2	2.87E-11
13.83	7254.2	2.86E-11
14.00	7229.1	2.85E-11
14.17	7215.2	2.85E-11
14.33	7215.8	2.85E-11
14.83	7118.1	2.84E-11

Table G.1 Continued

Sample No.1		
Time (hr)	GC data (ppm)	Permeability (mol m^{-1} s^{-1} $Pa^{-0.5}$)
15.00	7177.9	2.83E-11
15.17	7167.4	2.81E-11
15.33	7113	2.81E-11
15.50	7101.1	2.80E-11
15.67	7089.4	2.82E-11
15.83	7123.8	2.84E-11
16.00	7188.2	2.81E-11
16.17	7104.1	2.81E-11
16.33	7101.6	2.76E-11
16.50	6977.7	2.78E-11
16.67	7031.4	2.78E-11
16.83	7037.1	2.76E-11
17.00	6986.3	2.74E-11
17.17	6947.3	2.76E-11
17.33	6996.9	2.76E-11
17.50	6994.3	2.77E-11
17.67	7012.2	2.76E-11
17.83	6991.3	2.76E-11
18.00	7001.6	2.76E-11
18.17	6988.4	2.75E-11
18.33	6977.4	2.75E-11
18.50	6969	2.72E-11
18.67	6889.4	2.73E-11
18.83	6907.7	2.71E-11
19.00	6871.6	2.72E-11
19.17	6893.2	2.70E-11
19.33	6850.5	2.70E-11
19.50	6851.2	2.72E-11
19.67	6895	2.70E-11
19.83	6832.6	2.70E-11
20.00	6844	2.70E-11
20.17	6854.4	2.68E-11
20.33	6804.9	2.68E-11
20.50	6789.5	2.69E-11
20.67	6826.6	2.69E-11
20.83	6832.3	2.66E-11
21.00	6757.4	2.64E-11
21.17	6708.5	2.66E-11
21.67	6713.4	2.65E-11

Table G.1 Continued

Sample No.1		
Time (hr)	GC data (ppm)	Permeability (mol m^{-1} s^{-1} $Pa^{-0.5}$)
21.83	6723.1	2.64E-11
22.00	6702	2.64E-11
22.17	6695.1	2.64E-11
22.33	6691.5	2.61E-11
22.50	6619.3	2.60E-11
22.67	6612	2.60E-11
22.83	6602.2	2.61E-11
23.00	6625.6	2.61E-11
23.17	6626.6	2.61E-11
23.33	6617.8	2.61E-11
23.50	6625.9	2.59E-11
23.67	6574.4	2.59E-11
23.83	6582.5	2.59E-11
24.00	6579.4	9.10E-12

Table G.2 Raw permeability data of $Ni_{60}Nb_{40}Ti_5$ Pd-coated amorphous membranes-1

Sample No.1			Sample No.2		
Time (hr)	GC data (ppm)	Permeability (mol m^{-1} s^{-1} $Pa^{-0.5}$)	Time (hr)	GC data (ppm)	Permeability (mol m^{-1} s^{-1} $Pa^{-0.5}$)
0.00	24900.00	1.05E-10	0.00	9821.00	4.09E-11
0.03	31800.00	1.38E-10	0.03	10100.00	4.22E-11
0.07	35500.00	1.56E-10	0.07	10300.00	4.31E-11
0.10	36700.00	1.63E-10	0.10	10400.00	4.35E-11
0.13	37600.00	1.67E-10	0.13	10600.00	4.44E-11
0.17	38500.00	1.72E-10	0.17	10600.00	4.44E-11
0.20	39400.00	1.76E-10	0.20	10800.00	4.53E-11
0.23	40000.00	1.79E-10	0.23	10800.00	4.53E-11
0.27	40400.00	1.82E-10	0.27	10900.00	4.57E-11
0.30	40900.00	1.84E-10	0.30	10900.00	4.57E-11
0.33	41700.00	1.88E-10	0.33	10900.00	4.57E-11
0.37	42100.00	1.90E-10	0.37	11000.00	4.62E-11
0.40	42300.00	1.91E-10	0.40	11000.00	4.62E-11
0.43	42400.00	1.92E-10	0.43	11000.00	4.62E-11
0.47	42500.00	1.92E-10	0.47	11000.00	4.62E-11
0.50	42600.00	1.93E-10	0.50	11000.00	4.62E-11
0.53	42800.00	1.94E-10	0.53	11000.00	4.62E-11
0.57	42900.00	1.95E-10	0.57	11000.00	4.62E-11
0.60	42900.00	1.95E-10	0.60	11000.00	4.62E-11
0.63	42900.00	1.95E-10	0.63	11000.00	4.62E-11

Table G.2 Continued

Sample No.1			Sample No.2		
Time (hr)	GC data (ppm)	Permeability (mol m^{-1} s^{-1} $Pa^{-0.5}$)	Time (hr)	GC data (ppm)	Permeability (mol m^{-1} s^{-1} $Pa^{-0.5}$)
0.67	43000.00	1.95E-10	0.67	11000.00	4.62E-11
0.70	43000.00	1.95E-10	0.70	11000.00	4.62E-11
0.73	42900.00	1.95E-10	0.73	11000.00	4.62E-11
0.77	42800.00	1.94E-10	0.77	11000.00	4.62E-11
0.80	42700.00	1.94E-10	0.80	11000.00	4.62E-11
0.83	42600.00	1.93E-10	0.83	11000.00	4.62E-11
0.87	42600.00	1.93E-10	0.87	11000.00	4.62E-11
0.90	42500.00	1.92E-10	0.90	11000.00	4.62E-11
0.93	42400.00	1.92E-10	0.93	11000.00	4.62E-11
0.97	42300.00	1.91E-10	0.97	11000.00	4.62E-11
1.00	42200.00	1.91E-10	1.00	11000.00	4.62E-11
1.03	42100.00	1.90E-10	1.03	11000.00	4.62E-11
1.07	42000.00	1.90E-10	1.07	11000.00	4.62E-11
1.10	41900.00	1.89E-10	1.10	11000.00	4.62E-11
1.13	41800.00	1.89E-10	1.13	10900.00	4.57E-11
1.17	41700.00	1.88E-10	1.17	10900.00	4.57E-11
1.20	41600.00	1.88E-10	1.20	10900.00	4.57E-11
1.23	41500.00	1.87E-10	1.23	10900.00	4.57E-11
1.27	41400.00	1.87E-10	1.27	10900.00	4.57E-11
1.30	41300.00	1.86E-10	1.30	10800.00	4.53E-11
1.33	41200.00	1.86E-10	1.33	10900.00	4.57E-11
1.37	41100.00	1.85E-10	1.37	10800.00	4.53E-11
1.40	41000.00	1.85E-10	1.40	10800.00	4.53E-11
1.43	40800.00	1.84E-10	1.43	10800.00	4.53E-11
1.47	40700.00	1.83E-10	1.47	10800.00	4.53E-11
1.50	40500.00	1.82E-10	1.50	10800.00	4.53E-11
1.53	40500.00	1.82E-10	1.53	10800.00	4.53E-11
1.57	40300.00	1.81E-10	1.57	10700.00	4.48E-11
1.60	40200.00	1.80E-10	1.60	10700.00	4.48E-11
1.63	40100.00	1.80E-10	1.63	10600.00	4.44E-11
1.67	40000.00	1.79E-10	1.67	10700.00	4.48E-11
1.70	39900.00	1.79E-10	1.70	10700.00	4.48E-11
1.73	39800.00	1.78E-10	1.73	10700.00	4.48E-11
1.77	39600.00	1.77E-10	1.77	10600.00	4.44E-11
1.80	39500.00	1.77E-10	1.80	10600.00	4.44E-11
1.83	39500.00	1.77E-10	1.83	10600.00	4.44E-11
1.87	39400.00	1.76E-10	1.87	10600.00	4.44E-11
1.90	39400.00	1.76E-10	1.90	10600.00	4.44E-11
1.93	39500.00	1.77E-10	1.93	10600.00	4.44E-11

Table G.2 Continued

Sample No.1			Sample No.2		
Time (hr)	GC data (ppm)	Permeability (mol m^{-1} s^{-1} $Pa^{-0.5}$)	Time (hr)	GC data (ppm)	Permeability (mol m^{-1} s^{-1} $Pa^{-0.5}$)
1.97	39600.00	1.77E-10	2.10	10400.00	4.35E-11
2.00	39600.00	1.77E-10	2.27	10400.00	4.35E-11
2.03	39500.00	1.77E-10	2.43	10300.00	4.31E-11
2.07	39200.00	1.75E-10	2.60	10300.00	4.31E-11
2.10	38900.00	1.74E-10	2.77	10200.00	4.26E-11
2.13	38700.00	1.73E-10	2.93	10100.00	4.22E-11
2.17	38500.00	1.72E-10	3.10	10100.00	4.22E-11
2.20	38400.00	1.71E-10	3.27	10000.00	4.17E-11
2.23	38300.00	1.71E-10	3.43	10000.00	4.17E-11
2.27	38200.00	1.70E-10	3.60	10000.00	4.17E-11
2.30	38300.00	1.71E-10	3.77	9971.00	4.16E-11
2.33	38100.00	1.70E-10	3.93	9934.20	4.14E-11
2.37	38000.00	1.69E-10	4.10	9890.70	4.13E-11
2.40	37900.00	1.69E-10	4.27	9834.40	4.10E-11
2.43	37700.00	1.68E-10	4.43	9797.20	4.08E-11
2.47	37500.00	1.67E-10	4.60	9707.50	4.04E-11
2.50	37300.00	1.66E-10	4.77	9673.00	4.03E-11
2.53	37100.00	1.65E-10	4.93	9728.80	4.05E-11
2.57	36900.00	1.64E-10	5.10	9718.90	4.05E-11
2.60	36700.00	1.63E-10	5.27	9643.00	4.02E-11
2.77	36100.00	1.60E-10	5.43	9677.20	4.03E-11
2.93	36500.00	1.62E-10	5.60	9605.20	4.00E-11
3.10	37800.00	1.68E-10	5.77	9628.30	4.01E-11
3.27	39100.00	1.75E-10	5.93	9595.40	4.00E-11
3.43	40100.00	1.80E-10	6.10	9582.00	3.99E-11
3.60	40700.00	1.83E-10	6.27	9564.20	3.98E-11
3.77	41200.00	1.86E-10	6.43	9546.40	3.97E-11
3.93	41500.00	1.87E-10	6.60	9523.40	3.96E-11
4.10	41700.00	1.88E-10	6.77	9508.20	3.96E-11
4.27	41800.00	1.89E-10	6.93	9490.80	3.95E-11
4.43	41900.00	1.89E-10	7.10	9433.00	3.92E-11
4.60	42000.00	1.90E-10	7.27	9464.10	3.94E-11
4.77	41900.00	1.89E-10	7.43	9450.50	3.93E-11
4.93	41900.00	1.89E-10	7.60	9435.10	3.92E-11
5.10	41900.00	1.89E-10	7.77	9364.50	3.89E-11
5.27	41900.00	1.89E-10	7.93	9405.40	3.91E-11
5.43	41900.00	1.89E-10	8.10	9331.60	3.88E-11
5.60	41900.00	1.89E-10	8.27	9334.60	3.88E-11
5.77	41900.00	1.89E-10	8.43	9360.20	3.89E-11

Table G.2 Continued

Sample No.1			Sample No.2		
Time (hr)	GC data (ppm)	Permeability (mol m^{-1} s^{-1} $Pa^{-0.5}$)	Time (hr)	GC data (ppm)	Permeability (mol m^{-1} s^{-1} $Pa^{-0.5}$)
5.93	41900.00	1.89E-10	8.60	9277.30	3.86E-11
6.10	41800.00	1.89E-10	8.77	9315.00	3.87E-11
6.27	41800.00	1.89E-10	8.93	9308.10	3.87E-11
6.43	41700.00	1.88E-10	9.10	9309.90	3.87E-11
6.60	41600.00	1.88E-10	9.27	9316.10	3.87E-11
6.77	41600.00	1.88E-10	9.43	9310.70	3.87E-11
6.93	41600.00	1.88E-10	9.60	9259.40	3.85E-11
7.10	41500.00	1.87E-10	9.77	9297.30	3.86E-11
7.27	41600.00	1.88E-10	9.93	9300.40	3.87E-11
7.43	41600.00	1.88E-10	10.32	9286.90	3.86E-11
7.60	41600.00	1.88E-10	10.43	9235.30	3.84E-11
7.77	41500.00	1.87E-10	10.60	9280.50	3.86E-11
7.93	41400.00	1.87E-10	10.77	9226.30	3.83E-11
8.10	41400.00	1.87E-10	10.93	9271.70	3.85E-11
8.27	41400.00	1.87E-10	11.10	9208.20	3.82E-11
8.43	41400.00	1.87E-10	11.27	9265.30	3.85E-11
8.60	41400.00	1.87E-10	11.43	9198.30	3.82E-11
8.77	41400.00	1.87E-10	11.60	9251.90	3.84E-11
8.93	41300.00	1.86E-10	11.77	9254.20	3.84E-11
9.10	41300.00	1.86E-10	11.93	9207.60	3.82E-11
9.27	41200.00	1.86E-10	12.10	9242.40	3.84E-11
9.43	41200.00	1.86E-10	12.27	9232.80	3.84E-11
9.60	41100.00	1.85E-10	12.43	9216.90	3.83E-11
9.77	41100.00	1.85E-10	12.60	9163.20	3.80E-11
9.93	41000.00	1.85E-10	12.77	9203.80	3.82E-11
10.10	41000.00	1.85E-10	12.93	9197.10	3.82E-11
10.27	41000.00	1.85E-10	13.10	9194.50	3.82E-11
10.43	40900.00	1.84E-10	13.27	9191.80	3.82E-11
10.60	40900.00	1.84E-10	13.43	9180.80	3.81E-11
10.77	40900.00	1.84E-10	13.60	9171.20	3.81E-11
10.93	40800.00	1.84E-10	13.77	9160.60	3.80E-11
11.10	40700.00	1.83E-10	13.93	9166.80	3.81E-11
11.27	40600.00	1.83E-10	14.10	9144.20	3.80E-11
11.43	40500.00	1.82E-10	14.27	9093.90	3.77E-11
11.60	39800.00	1.78E-10	14.43	9095.30	3.78E-11
11.77	37400.00	1.66E-10	14.60	9136.50	3.79E-11
11.93	34300.00	1.50E-10	14.77	9076.40	3.77E-11
12.10	30800.00	1.33E-10	14.93	9116.80	3.78E-11
12.27	27500.00	1.17E-10	15.10	9110.90	3.78E-11

Table G.2 Continued

Sample No.1			Sample No.2		
Time (hr)	GC data (ppm)	Permeability (mol m^{-1} s^{-1} $Pa^{-0.5}$)	Time (hr)	GC data (ppm)	Permeability (mol m^{-1} s^{-1} $Pa^{-0.5}$)
12.43	24300.00	1.02E-10	15.27	9058.40	3.76E-11
12.60	21300.00	8.84E-11	15.43	9052.90	3.76E-11
12.77	18700.00	7.67E-11	15.60	9026.90	3.75E-11
12.93	16300.00	6.60E-11	15.77	9056.80	3.76E-11
13.10	14200.00	5.69E-11	15.93	9048.70	3.75E-11
13.27	12300.00	4.88E-11	16.10	9000.70	3.73E-11
13.43	10700.00	4.20E-11	16.27	9043.70	3.75E-11
13.60	9185.43	3.58E-11	16.43	9037.40	3.75E-11
13.77	7792.37	3.01E-11	16.60	8989.20	3.73E-11
13.93	6605.05	2.53E-11	16.77	9024.00	3.74E-11
			16.93	9008.70	3.74E-11
			17.10	9008.30	3.74E-11
			17.27	8954.40	3.71E-11
			17.43	8988.80	3.73E-11
			17.60	8978.30	3.72E-11
			17.77	8977.60	3.72E-11
			17.93	8959.70	3.72E-11
			18.10	8954.90	3.71E-11
			18.27	8954.00	3.71E-11
			18.43	8955.00	3.71E-11
			18.60	8885.10	3.68E-11
			18.77	8938.30	3.71E-11
			18.93	8923.50	3.70E-11
			19.10	8922.00	3.70E-11
			19.27	8912.60	3.70E-11
			19.43	8907.00	3.69E-11
			19.60	8901.10	3.69E-11
			19.77	8901.60	3.69E-11
			19.93	8849.70	3.67E-11
			20.10	8860.00	3.67E-11
			20.27	8906.20	3.69E-11
			20.43	8903.80	3.69E-11
			20.60	8900.30	3.69E-11
			20.77	8893.60	3.69E-11
			21.10	8883.50	3.68E-11
			21.27	8835.70	3.66E-11
			21.43	8874.60	3.68E-11
			21.60	8869.80	3.68E-11
			21.77	8811.80	3.65E-11

Table G.2 Continued

Sample No.2		
Time (hr)	GC data (ppm)	Permeability (mol m^{-1} s^{-1} $Pa^{-0.5}$)
21.93	8863.10	3.67E-11
22.10	8856.00	3.67E-11
22.27	8860.70	3.67E-11
22.43	8803.40	3.65E-11
22.60	8838.80	3.66E-11
22.77	8835.60	3.66E-11
22.93	8833.00	3.66E-11
23.10	8832.10	3.66E-11
23.27	8825.50	3.66E-11
23.43	8819.80	3.65E-11
23.60	8814.20	3.65E-11
23.77	8810.20	3.65E-11
23.93	8804.30	3.65E-11
24.10	8803.60	3.65E-11
24.27	8801.00	3.65E-11

Table G.3 Raw permeability data of $Ni_{60}Nb_{40}Ti_5$ Pd-coated amorphous membranes-2

Sample No.3		
Time (hr)	GC data (ppm)	Permeability (mol m^{-1} s^{-1} $Pa^{-0.5}$)
0.00	13500.00	5.47E-11
0.03	13900.00	5.65E-11
0.07	14200.00	5.78E-11
0.10	14300.00	5.82E-11
0.13	14500.00	5.91E-11
0.17	14600.00	5.95E-11
0.20	14600.00	5.95E-11
0.23	14500.00	5.91E-11
0.27	14500.00	5.91E-11
0.30	14400.00	5.87E-11
0.33	14200.00	5.78E-11
0.37	13900.00	5.65E-11
0.40	13700.00	5.56E-11
0.43	13500.00	5.47E-11
0.47	13400.00	5.43E-11
0.50	13200.00	5.34E-11
0.53	13200.00	5.34E-11
0.57	13100.00	5.30E-11

Table G.3 Continued

Sample No.3		
Time (hr)	GC data (ppm)	Permeability (mol m^{-1} s^{-1} $Pa^{-0.5}$)
0.60	13000.00	5.26E-11
0.63	13000.00	5.26E-11
0.67	12900.00	5.21E-11
0.70	12900.00	5.21E-11
0.73	12900.00	5.21E-11
0.77	12800.00	5.17E-11
0.80	12900.00	5.21E-11
0.83	12900.00	5.21E-11
0.87	12800.00	5.17E-11
0.90	12900.00	5.21E-11
0.93	12900.00	5.21E-11
0.97	13000.00	5.26E-11
1.00	12900.00	5.21E-11
1.03	13000.00	5.26E-11
1.07	13000.00	5.26E-11
1.10	13100.00	5.30E-11
1.13	13000.00	5.26E-11
1.17	13100.00	5.30E-11
1.20	13000.00	5.26E-11
1.23	13000.00	5.26E-11
1.27	13000.00	5.26E-11
1.30	13000.00	5.26E-11
1.33	13000.00	5.26E-11
1.37	13000.00	5.26E-11
1.40	13000.00	5.26E-11
1.43	13000.00	5.26E-11
1.47	13000.00	5.26E-11
1.50	12900.00	5.21E-11
1.53	13000.00	5.26E-11
1.57	13000.00	5.26E-11
1.60	13000.00	5.26E-11
1.67	12900.00	5.21E-11
1.70	12900.00	5.21E-11
1.73	12900.00	5.21E-11
1.77	13000.00	5.26E-11
1.80	12900.00	5.21E-11
1.83	12900.00	5.21E-11
1.87	12900.00	5.21E-11
1.90	12900.00	5.21E-11

Table G.3 Continued

Sample No.3		
Time (hr)	GC data (ppm)	Permeability (mol m^{-1} s^{-1} $Pa^{-0.5}$)
1.93	12800.00	5.17E-11
1.97	12800.00	5.17E-11
2.00	12800.00	5.17E-11
2.03	12800.00	5.17E-11
2.07	12800.00	5.17E-11
2.10	12700.00	5.13E-11
2.13	12700.00	5.13E-11
2.17	12700.00	5.13E-11
2.20	12700.00	5.13E-11
2.23	12600.00	5.08E-11
2.27	12600.00	5.08E-11
2.30	12600.00	5.08E-11
2.33	12500.00	5.04E-11
2.37	12500.00	5.04E-11
2.40	12500.00	5.04E-11
2.43	12400.00	5.00E-11
2.60	12300.00	4.95E-11
2.77	12200.00	4.91E-11
2.93	12000.00	4.82E-11
3.10	11900.00	4.78E-11
3.27	11700.00	4.70E-11
3.43	11600.00	4.65E-11
3.60	11400.00	4.57E-11
3.77	11300.00	4.52E-11
3.93	11100.00	4.44E-11
4.10	11000.00	4.40E-11
4.27	10900.00	4.35E-11
4.43	10800.00	4.31E-11
4.60	10600.00	4.23E-11
4.77	10500.00	4.18E-11
4.93	10400.00	4.14E-11
5.10	10300.00	4.10E-11
5.27	10200.00	4.06E-11
5.43	9999.30	3.97E-11
5.60	9946.09	3.95E-11
5.77	9845.80	3.91E-11
5.93	9739.50	3.86E-11
6.10	9644.00	3.82E-11
6.27	9551.70	3.79E-11

Table G.3 Continued

Sample No.3		
Time (hr)	GC data (ppm)	Permeability (mol m^{-1} s^{-1} $Pa^{-0.5}$)
6.43	9460.10	3.75E-11
6.60	9370.40	3.71E-11
6.77	9218.40	3.65E-11
6.93	9195.10	3.64E-11
7.10	9116.70	3.60E-11
7.27	9039.00	3.57E-11
7.43	8958.40	3.54E-11
7.60	8844.30	3.49E-11
7.77	8816.40	3.48E-11
7.93	8750.50	3.45E-11
8.10	8624.80	3.40E-11
8.27	8585.80	3.38E-11
8.43	8567.50	3.37E-11
8.60	8511.70	3.35E-11
8.77	8446.20	3.32E-11
8.93	8337.60	3.28E-11
9.10	8341.00	3.28E-11
9.27	8289.30	3.26E-11
9.43	8243.70	3.24E-11
9.60	8144.10	3.20E-11
9.77	8146.00	3.20E-11
9.93	8046.20	3.16E-11
10.10	7995.90	3.14E-11
10.27	7958.30	3.12E-11
10.43	7971.30	3.13E-11
10.60	7939.80	3.11E-11
10.77	7908.70	3.10E-11
10.93	7877.60	3.09E-11
11.10	7848.50	3.08E-11
11.27	7765.30	3.04E-11
11.43	7745.00	3.03E-11
11.60	7714.10	3.02E-11
11.77	7690.10	3.01E-11
11.93	7673.90	3.00E-11
12.10	7657.50	3.00E-11
12.27	7648.90	2.99E-11
12.43	7578.90	2.97E-11
12.60	7562.30	2.96E-11
12.77	7557.70	2.96E-11

Table G.3 Continued

Sample No.3		
Time (hr)	GC data (ppm)	Permeability (mol m^{-1} s^{-1} $Pa^{-0.5}$)
12.93	7536.10	2.95E-11
13.10	7493.00	2.93E-11
13.27	7447.50	2.91E-11
13.43	7591.70	2.97E-11
13.60	7403.40	2.89E-11
13.77	7442.00	2.91E-11
13.93	7389.80	2.89E-11
14.10	7370.70	2.88E-11
14.27	7390.50	2.89E-11
14.43	7272.40	2.84E-11
14.60	7297.50	2.85E-11
14.77	7275.80	2.84E-11
14.93	7245.70	2.83E-11
15.10	7212.00	2.82E-11
15.27	7246.10	2.83E-11
15.43	7190.00	2.81E-11
15.60	7201.30	2.81E-11
15.77	7243.70	2.83E-11
15.93	7213.20	2.82E-11
16.10	7200.20	2.81E-11
16.27	7174.50	2.80E-11
16.43	7169.60	2.80E-11
16.60	7175.50	2.80E-11
16.77	7180.20	2.80E-11
16.93	7165.20	2.80E-11
17.10	7083.80	2.76E-11
17.27	7109.40	2.77E-11
17.43	7105.20	2.77E-11
17.60	7059.70	2.75E-11
17.77	7073.60	2.76E-11
17.93	7005.40	2.73E-11
18.10	7043.90	2.75E-11
18.27	7053.00	2.75E-11
18.43	7018.10	2.74E-11
18.60	7044.60	2.75E-11
18.77	7051.90	2.75E-11
18.93	7054.50	2.75E-11
19.10	6928.90	2.70E-11
19.27	6965.80	2.71E-11

Table G.3 Continued

Sample No.3		
Time (hr)	GC data (ppm)	Permeability (mol m^{-1} s^{-1} $Pa^{-0.5}$)
19.43	6971.80	2.72E-11
19.60	6937.70	2.70E-11
19.77	7009.90	2.73E-11
19.93	7018.40	2.74E-11
20.10	6956.20	2.71E-11
20.27	6985.80	2.72E-11
20.43	6971.20	2.72E-11
20.60	6960.40	2.71E-11
20.77	6904.60	2.69E-11
20.93	6908.20	2.69E-11
21.10	6909.80	2.69E-11
21.27	6871.00	2.68E-11
21.43	6901.40	2.69E-11
21.60	6868.90	2.67E-11
21.77	6903.20	2.69E-11
21.93	6882.10	2.68E-11
22.10	6876.10	2.68E-11
22.27	6821.30	2.66E-11
22.43	6855.20	2.67E-11
22.60	6801.90	2.65E-11
23.60	6774.80	2.64E-11
23.77	6823.30	2.66E-11
23.93	6771.70	2.64E-11
24.10	6800.50	2.65E-11

Table G.4 Raw permeability data of $Ni_{60}Nb_{35}Zr_5$ Pd-coated amorphous membranes

Sample No.1			Sample No.2		
Time (hr)	GC data (ppm)	Permeability (mol m^{-1} s^{-1} $Pa^{-0.5}$)	Time (hr)	GC data (ppm)	Permeability (mol m^{-1} s^{-1} $Pa^{-0.5}$)
0.00	14800.00	5.62E-11	0.00	24200.00	1.02E-10
0.05	16100.00	6.15E-11	0.03	24800.00	1.05E-10
0.10	17300.00	6.65E-11	0.07	25300.00	1.08E-10
0.13	18000.00	6.94E-11	0.10	25700.00	1.10E-10
0.18	18900.00	7.32E-11	0.13	26000.00	1.11E-10
0.23	19600.00	7.61E-11	0.17	26300.00	1.12E-10
0.28	20600.00	8.03E-11	0.20	26600.00	1.14E-10
0.33	20600.00	8.03E-11	0.23	26800.00	1.15E-10
0.38	21000.00	8.20E-11	0.27	27000.00	1.16E-10
0.43	21300.00	8.33E-11	0.30	27400.00	1.18E-10

Table G.4 Continued

Sample No.1			Sample No.2		
Time (hr)	GC data (ppm)	Permeability (mol m^{-1} s^{-1} $Pa^{-0.5}$)	Time (hr)	GC data (ppm)	Permeability (mol m^{-1} s^{-1} $Pa^{-0.5}$)
0.48	21500.00	8.42E-11	0.33	27200.00	1.17E-10
0.53	21700.00	8.50E-11	0.37	27100.00	1.16E-10
0.58	21900.00	8.59E-11	0.40	27300.00	1.17E-10
0.63	22000.00	8.63E-11	0.43	27600.00	1.19E-10
0.68	22100.00	8.68E-11	0.47	27900.00	1.20E-10
0.73	22200.00	8.72E-11	0.50	28200.00	1.21E-10
0.78	22300.00	8.76E-11	0.53	28500.00	1.23E-10
0.83	22400.00	8.80E-11	0.57	28800.00	1.24E-10
0.88	22400.00	8.80E-11	0.60	29000.00	1.25E-10
0.93	22500.00	8.85E-11	0.63	29200.00	1.26E-10
0.98	22500.00	8.85E-11	0.67	29300.00	1.27E-10
1.03	22600.00	8.89E-11	0.70	29500.00	1.28E-10
1.08	22500.00	8.85E-11	0.73	29600.00	1.28E-10
1.13	22600.00	8.89E-11	0.77	29700.00	1.29E-10
1.18	22600.00	8.89E-11	0.80	29800.00	1.29E-10
1.23	22600.00	8.89E-11	0.83	29900.00	1.30E-10
1.28	22600.00	8.89E-11	0.87	30000.00	1.30E-10
1.33	22600.00	8.89E-11	0.90	30000.00	1.30E-10
1.38	22500.00	8.85E-11	0.93	30100.00	1.31E-10
1.43	22600.00	8.89E-11	0.97	30200.00	1.31E-10
1.48	22500.00	8.85E-11	1.00	30300.00	1.32E-10
1.53	22500.00	8.85E-11	1.08	30500.00	1.33E-10
1.58	22400.00	8.80E-11	1.17	30600.00	1.33E-10
1.63	22300.00	8.76E-11	1.25	30800.00	1.34E-10
1.68	22400.00	8.80E-11	1.33	30900.00	1.35E-10
1.73	22300.00	8.76E-11	1.42	31000.00	1.35E-10
1.83	22300.00	8.76E-11	1.50	31100.00	1.36E-10
1.92	22300.00	8.76E-11	1.58	31200.00	1.36E-10
2.00	22200.00	8.72E-11	1.67	31100.00	1.36E-10
2.08	22100.00	8.68E-11	1.75	31100.00	1.36E-10
2.17	22000.00	8.63E-11	1.83	31200.00	1.36E-10
2.25	22000.00	8.63E-11	1.92	31200.00	1.36E-10
2.33	22000.00	8.63E-11	2.00	31200.00	1.36E-10
2.42	21900.00	8.59E-11	2.08	31200.00	1.36E-10
2.50	21800.00	8.55E-11	2.17	31200.00	1.36E-10
2.58	21800.00	8.55E-11	2.25	31200.00	1.36E-10
2.67	21700.00	8.50E-11	2.33	31200.00	1.36E-10
2.75	21600.00	8.46E-11	2.42	31100.00	1.36E-10
2.83	21600.00	8.46E-11	2.50	31000.00	1.35E-10

Table G.4 Continued

Sample No.1			Sample No.2		
Time (hr)	GC data (ppm)	Permeability (mol m^{-1} s^{-1} $Pa^{-0.5}$)	Time (hr)	GC data (ppm)	Permeability (mol m^{-1} s^{-1} $Pa^{-0.5}$)
2.92	21500.00	8.42E-11	2.58	31000.00	1.35E-10
3.00	21400.00	8.38E-11	2.67	31000.00	1.35E-10
3.08	21400.00	8.38E-11	2.75	31000.00	1.35E-10
3.17	21400.00	8.38E-11	2.83	30900.00	1.35E-10
3.25	21300.00	8.33E-11	2.92	30800.00	1.34E-10
3.33	21100.00	8.25E-11	3.00	30800.00	1.34E-10
3.42	20900.00	8.16E-11	3.17	30600.00	1.33E-10
3.50	20800.00	8.12E-11	3.33	30500.00	1.33E-10
3.67	20700.00	8.08E-11	3.50	30400.00	1.32E-10
3.83	20600.00	8.03E-11	3.67	30200.00	1.31E-10
4.00	20400.00	7.95E-11	3.83	30100.00	1.31E-10
4.17	20300.00	7.91E-11	4.00	30000.00	1.30E-10
4.33	20100.00	7.82E-11	4.33	29500.00	1.28E-10
4.50	20000.00	7.78E-11	4.67	29200.00	1.26E-10
4.67	19800.00	7.69E-11	5.00	29000.00	1.25E-10
4.83	19800.00	7.69E-11	5.33	28800.00	1.24E-10
5.00	19800.00	7.69E-11	5.67	28500.00	1.23E-10
5.17	19800.00	7.69E-11	6.00	28200.00	1.21E-10
5.33	19700.00	7.65E-11	6.33	28000.00	1.20E-10
5.50	19700.00	7.65E-11	6.67	27800.00	1.20E-10
5.67	19800.00	7.69E-11	7.00	27600.00	1.19E-10
5.83	19800.00	7.69E-11	7.33	27400.00	1.18E-10
6.00	19800.00	7.69E-11	7.67	27200.00	1.17E-10
6.17	19700.00	7.65E-11	8.00	27000.00	1.16E-10
6.33	19800.00	7.69E-11	8.33	26800.00	1.15E-10
6.50	19800.00	7.69E-11	8.67	26500.00	1.13E-10
6.67	19800.00	7.69E-11	9.00	26300.00	1.12E-10
6.83	19800.00	7.69E-11	9.33	26200.00	1.12E-10
7.00	19800.00	7.69E-11	9.67	26000.00	1.11E-10
7.17	19800.00	7.69E-11	10.00	25800.00	1.10E-10
7.33	19800.00	7.69E-11	10.33	25400.00	1.08E-10
7.50	19800.00	7.69E-11	10.67	25000.00	1.06E-10
7.67	19800.00	7.69E-11	11.00	24800.00	1.05E-10
7.83	19800.00	7.69E-11	11.33	24700.00	1.05E-10
8.00	19800.00	7.69E-11	11.67	24500.00	1.04E-10
8.17	19800.00	7.69E-11	12.00	24400.00	1.03E-10
8.33	19800.00	7.69E-11	12.33	24200.00	1.02E-10
8.50	19800.00	7.69E-11	12.67	24000.00	1.01E-10
8.67	19800.00	7.69E-11	13.00	23700.00	1.00E-10

Table G.4 Continued

Sample No.1			Sample No.2		
Time (hr)	GC data (ppm)	Permeability (mol m^{-1} s^{-1} $Pa^{-0.5}$)	Time (hr)	GC data (ppm)	Permeability (mol m^{-1} s^{-1} $Pa^{-0.5}$)
8.83	19800.00	7.69E-11	13.33	23800.00	1.01E-10
9.00	19800.00	7.69E-11	13.67	23700.00	1.00E-10
9.17	19800.00	7.69E-11	14.00	23500.00	9.92E-11
9.33	19800.00	7.69E-11	14.33	23400.00	9.87E-11
9.50	19800.00	7.69E-11	14.67	23200.00	9.78E-11
9.67	19800.00	7.69E-11	15.00	23100.00	9.73E-11
9.83	19800.00	7.69E-11	15.33	23000.00	9.68E-11
10.00	19700.00	7.65E-11	15.67	22800.00	9.59E-11
10.17	19700.00	7.65E-11	16.00	22800.00	9.59E-11
10.33	19700.00	7.65E-11	16.33	22700.00	9.54E-11
10.50	19700.00	7.65E-11	17.25	22100.00	9.27E-11
10.67	19700.00	7.65E-11	17.33	22200.00	9.31E-11
10.83	19600.00	7.61E-11	17.50	22100.00	9.27E-11
11.00	19600.00	7.61E-11	17.67	22200.00	9.31E-11
11.17	19600.00	7.61E-11	17.83	22100.00	9.27E-11
11.33	19600.00	7.61E-11	18.00	22100.00	9.27E-11
11.50	19600.00	7.61E-11	18.17	22100.00	9.27E-11
11.67	19500.00	7.57E-11	18.33	22100.00	9.27E-11
11.83	19500.00	7.57E-11	18.50	22100.00	9.27E-11
12.00	19500.00	7.57E-11	18.67	21900.00	9.17E-11
12.17	19500.00	7.57E-11	18.83	22000.00	9.22E-11
12.33	19500.00	7.57E-11	19.00	21900.00	9.17E-11
12.50	19400.00	7.53E-11	19.17	21800.00	9.13E-11
12.67	19400.00	7.53E-11	19.33	21800.00	9.13E-11
12.83	19400.00	7.53E-11	19.50	21700.00	9.08E-11
13.00	19300.00	7.48E-11	19.67	21700.00	9.08E-11
13.17	19200.00	7.44E-11	19.83	21600.00	9.04E-11
13.33	19300.00	7.48E-11	20.00	21500.00	8.99E-11
13.50	19300.00	7.48E-11	20.17	21200.00	8.85E-11
13.67	19200.00	7.44E-11	20.33	21200.00	8.85E-11
13.83	19200.00	7.44E-11	20.50	21100.00	8.81E-11
14.00	19200.00	7.44E-11	20.67	21000.00	8.76E-11
14.17	19100.00	7.40E-11	20.83	21100.00	8.81E-11
14.33	19100.00	7.40E-11	21.00	21000.00	8.76E-11
14.50	19100.00	7.40E-11	21.17	21000.00	8.76E-11
14.67	19000.00	7.36E-11	21.33	21000.00	8.76E-11
14.83	19000.00	7.36E-11	21.50	21000.00	8.76E-11
15.00	19000.00	7.36E-11	21.67	20900.00	8.71E-11
15.17	18900.00	7.32E-11	21.83	20800.00	8.67E-11

Table G.4 Continued

Sample No.1			Sample No.2		
Time (hr)	GC data (ppm)	Permeability (mol m^{-1} s^{-1} $Pa^{-0.5}$)	Time (hr)	GC data (ppm)	Permeability (mol m^{-1} s^{-1} $Pa^{-0.5}$)
15.33	18900.00	7.32E-11	22.00	20700.00	8.62E-11
15.50	18900.00	7.32E-11	22.17	20600.00	8.58E-11
15.67	18800.00	7.27E-11	22.33	20600.00	8.58E-11
15.83	18800.00	7.27E-11	22.50	20500.00	8.53E-11
16.00	18800.00	7.27E-11	22.67	20500.00	8.53E-11
16.17	18700.00	7.23E-11	22.83	20400.00	8.49E-11
16.33	18600.00	7.19E-11	23.00	20400.00	8.49E-11
16.50	18700.00	7.23E-11	23.17	20300.00	8.44E-11
16.67	18600.00	7.19E-11	23.33	20300.00	8.44E-11
16.83	18600.00	7.19E-11	23.50	20100.00	8.35E-11
17.00	18600.00	7.19E-11	23.67	20000.00	8.30E-11
17.17	18500.00	7.15E-11			
17.33	18500.00	7.15E-11			
17.50	18500.00	7.15E-11			
17.67	18400.00	7.11E-11			
17.83	18400.00	7.11E-11			
18.00	18400.00	7.11E-11			
18.17	18300.00	7.06E-11			
18.33	18300.00	7.06E-11			
18.50	18300.00	7.06E-11			
18.67	18200.00	7.02E-11			
18.83	18200.00	7.02E-11			
19.00	18200.00	7.02E-11			
19.17	18100.00	6.98E-11			
19.33	18000.00	6.94E-11			
19.50	18000.00	6.94E-11			
19.67	18000.00	6.94E-11			
19.83	17500.00	6.73E-11			
20.00	16900.00	6.48E-11			
20.17	16900.00	6.48E-11			
20.33	17200.00	6.61E-11			
20.50	17400.00	6.69E-11			
20.67	17900.00	6.90E-11			
20.83	18100.00	6.98E-11			
21.00	18100.00	6.98E-11			
21.17	18000.00	6.94E-11			
21.33	18000.00	6.94E-11			
21.50	18000.00	6.94E-11			
21.67	17900.00	6.90E-11			

Table G.4 Continued

Sample No.1		
Time (hr)	GC data (ppm)	Permeability (mol m^{-1} s^{-1} $Pa^{-0.5}$)
21.83	17900.00	6.90E-11
22.00	17900.00	6.90E-11
22.17	17800.00	6.86E-11
22.33	17800.00	6.86E-11
22.50	17700.00	6.81E-11
22.67	17600.00	6.77E-11
22.83	17700.00	6.81E-11
23.00	17600.00	6.77E-11
23.17	17600.00	6.77E-11
23.33	17400.00	6.69E-11
23.50	17100.00	6.56E-11
23.67	16800.00	6.44E-11
23.83	16700.00	6.40E-11
24.00	16800.00	6.44E-11